

OPTIMUM YEARLY TILTED ANGLE OF PHOTOVOLTAIC CELL TO RECEIVE MAXIMUM SOLAR RADIATION IN SOUTHERN IRAQ CITIES

Ali Khalid Shaker Al-Sayyab and Maher Kadhim Taher

Refrigeration and Air Conditioning Department, Basra Technical College,
Foundation of Technical Education

Abstract:

The performance of photovoltaic cell is affected by the value of its tilt angle with respect to horizontal plane, where the variation of tilt angle changes the amount of solar radiation permit to the photovoltaic cell surface. So that, the using of solar tracking system for photovoltaic cell will get the maximum solar radiation that permit to the surface of the cell at any time and day of the year, but the solar tracking systems have high operation and maintenance costs and are not always applicable. It is often convenient to set the solar collector at an optimum fixed tilt angle over a time of the year with less reduction in solar radiation received in the cell surface.

This work is to find an optimum tilt angle of photovoltaic cell located in southern Iraqi cities Basrah city (latitude 30.30°), Amarah city (31.55°) and Nasiriyah (31°). A mathematical models was used and programed by engineering equation solver EES to find an optimum tilt angle depending on the maximum solar radiation, the tilted angle varied with range from 0° to 90° . The results showed that the optimum tilt angle for Basrah is 28° , where for Amarah is 30° and for Nasiriyah is 29° .

الخلاصة:

يتأثر اداء الخلية الشمسية بزاوية الميل عن المستوى الافقي، حيث ان تغيير زاوية الميل تغير كمية الاشعاع الشمسي الواصل لسطح الخلية الشمسية. لذلك فان استخدام منظومة التتبع الشمسية سيمكن من الحصول على اقصى كمية من الاشعاع الساقط والواصل لسطح الخلية في أي وقت من اليوم وفي أي يوم من ايام السنة . هذه المنظومة تمتاز بكلفة عمل وصيانة عالية ولا يمكن تطبيقها دائما. في الغالب يكون من المناسب ضبط المجمع الشمسي على زاوية ميل مثلى ثابتة على مدار السنة بأقل نقص في كمية الاشعاع الواصل والساقط على سطح الخلية.

تم في هذا البحث ايجاد زاوية الميل المثلى للخلية الشمسية عن المستوى الافقي في المنطقة الجنوبية من العراق والتي هي مدينة البصرة (على خط عرض 30.30°) وفي مدينة العمارة (على خط عرض 31.55°) وفي مدينة الناصرية (على خط عرض 31°). تم استخدام موديل رياضي لإيجاد زاوية الميلان المثلى من خلال برمجته وتحليله باستخدام برنامج EES بالاعتماد على اقصى كمية للإشعاع الشمسي الساقط، حيث ان زاوية الميلان تتغير من 0° لغاية 90° . اظهرت النتائج بان زاوية الميلان المثلى لمدينة البصرة هي (28°) و لمدينة العمارة (30°) و لمدينة الناصرية (29°) .

1- Introduction:

The ozone layer, which considered the “protective shield against ultraviolet radiation” ,regulates the amount of radiation that reaches Earth’s surface. The ultraviolet radiation can cause non-melanoma and malignant melanoma skin cancer. It can also have negative effects on plant growth, marine animals, and normal ecological cycles in nature. Yet in the 1977s it was discovered that Because of the actions of humans, the ozone layer is deteriorating by emissions into the atmosphere from industrial [1]

The Greenhouse Effect produces rapid and alarming warming of the lower level atmosphere. It is caused by the presence of greenhouse gases (GHG) which trap heat that would otherwise escape into space. The most significant cause of the increased greenhouse effect and global warming is the 30% increase in atmospheric carbon dioxide (a well-known GHG) since 1950. Present carbon dioxide concentrations have not been seen in 20 million years. It is estimated that $\frac{3}{4}$ of the GHG emissions in the last 20 years. According to the World Health Organization (WHO), global warming killed 150,000 people in the year 2000 and this number could double in the next decade [1].

At 1997, in Kyoto a protocol was written, which an effort to work toward sustainable development. The Kyoto Protocol was signed by more than 55% of the countries worldwide. The goal of the Kyoto Protocol is to reduce the emissions levels of 6 major greenhouse gases in 1990 by 5.2% between the years 2008 and 2012[2]. Only developed countries have been able to quantify their commitment to emissions reduction. There for the use of energy source with no emission of Co_2 is a good choice for reducing the effect of global warming

Renewable energy technologies are those that provide energy from a source considered inexhaustible (i.e. the sun, wind, biomass, river water, etc.). Within renewable, the potential of

solar technologies has recently caused a large increase in its development, the use of renewable energy technologies is an effective way to reduce emissions.

Solar energy technology is one of the best solutions for future energy production. It is clean which produces no fossil fuel emissions. Combustion does not occur within a solar energy system, storable and will eventually be less expensive than fossil fuel.

The characteristics of solar energy make it well suited to supply peak electricity demands. In the southern Iraq cities which receive high solar radiation, in these cities the summer peak demands have become overwhelming give strong pressure to the installation of solar plants is ideal in this cities as the “solar belt”

Photovoltaic cells are the one of common type of the form of solar energy collector it convert solar radiation into electricity. The performance of the Photovoltaic cells is highly dependent on its orientation, cell tilted angle, optical and geometric properties, macro and microclimatic conditions, geographical position, and the period of use (Ashok Kumar,2011). The tilt angle, defined as the angle of PV arrays with respect to horizontal.It is a dominant parameter affecting the collectible radiation of a fixed PV array.

Many studies show that the optimum tilt angle depends on latitude angle (λ), solar declination angle or days of the year [6]. Soulayman et al showed the optimum tilt angle is almost equal to the latitude [3].Where other show the daily solar energy collected was reported to be 19 to 24% higher by a solar PV panel with one axis east-west tracking system than by a fixed system [4] .Hamdy K.Elminir et al showed the yearly optimum tilted angle for Helwan Egypt is about ($\text{latitude} \pm 15^\circ$) where (+)refer to summer and(–)refer to winter [5].Koray reported that the optimum orientation of the PV array should be directly towards the equator, facing south in the northern hemisphere and the optimum tilt angle depends only on the latitude [6]. Kamal Skeiker (2009)show that the changing of the tilt angle of PV cell located in Syria by 12 times in a year achieves a solar radiation of approximately 30% more than the case of a solar collector fixed on a horizontal surface[9]. Ashok Kumar et al. found the optimum tilted angle for PV cell array in Punjab India changes between 60.5° (January) and 62.5° (December) throughout the year [11].

2- Mathematical Method for Finding the Optimum Tilted Angle:-

The total daily irradiation on a horizontal plane is the combination of two components, the direct irradiation and the diffuse irradiation from the sky [11]

In this study the Bernard-Menguy-Schwartz model is used to find the optimum tilt angle (β) of photovoltaic cell solar collector in southern Iraq cities because it's more simple correlation than other authors and predicted to northern hemisphere [10].

In Bernard-Menguy-Schwartz model the direct radiation under three conditions of sky, they are :

a- Clear Sky:

$$I_D = 1230e^{\left(\frac{-1}{3.8 \sin(h_s+1.6)}\right)} \quad (1)$$

b- Very Clear Sky:

$$I_D = 1210e^{\left(\frac{-1}{6 \sin(h_s+1)}\right)} \quad (2)$$

c- Polluted Sky:

$$I_D = 1260e^{\left(\frac{-1}{2.3 \sin(h_s+3)}\right)} \quad (3)$$

The diffused radiation (D_H) for any sky conditions:-

$$D_H = 125(\sin(h_s))^{0.4} \quad (4)$$

The total radiation received(G_H) by the horizontal plane is:-

$$G_H = D_H + I_D \sin(h_s) \quad (5)$$

The Diffuse (D_i) and the total radiations (G_i) receipts by the inclined collector plane are :

$$D_i = \frac{1+\cos(\beta)}{2} D_H + \frac{1-\cos(\beta)}{2} G_H \alpha \quad (6)$$

$$G_i = I_D \cdot \cos(\theta) + D_i \quad (7)$$

Where the factor α is the coefficient of reflection of the ground located in front of the collector (usually taken equal to 0.2)[10]. The angle θ formed between the normal of the collector and the solar rays at solar midday that shown fig(1) is define by:

$$\theta = 90 - (\beta + h_s) \quad (8)$$

$$\square h_s = 90 - \varphi + \delta \quad (9)$$

The duration of the day (ΔD) is given by:-

$$\Delta D = \frac{2}{15} \arccosh(-\tan(\varphi) \cdot \tan(\delta)) \quad (10)$$

$$\text{where } \delta = 23.45 \sin\left(360^\circ \frac{(284 + N)}{365}\right) \quad (11)$$

The received energy is given by:

$$E = \frac{2}{\pi} \times G_i \times \Delta E \quad (12)$$

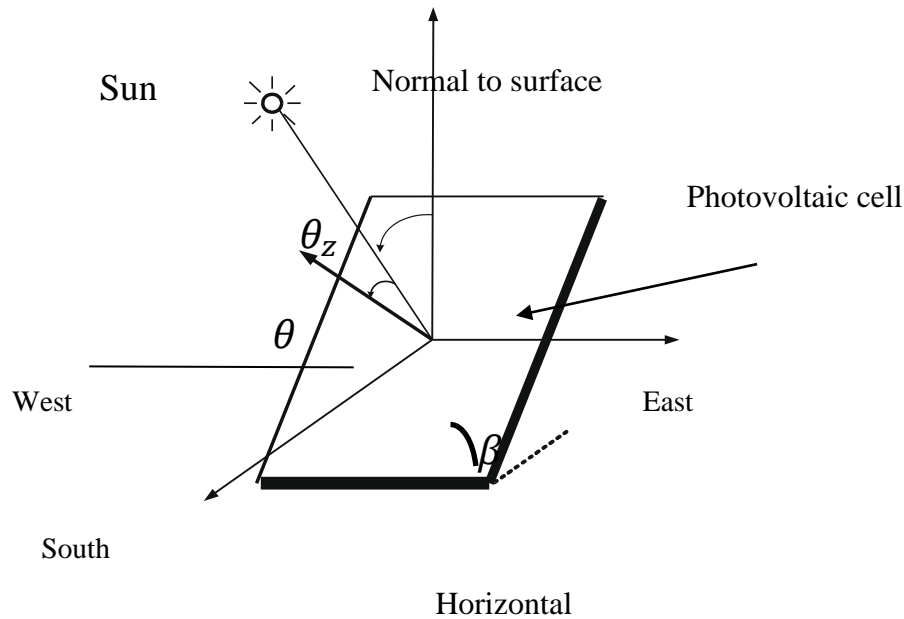
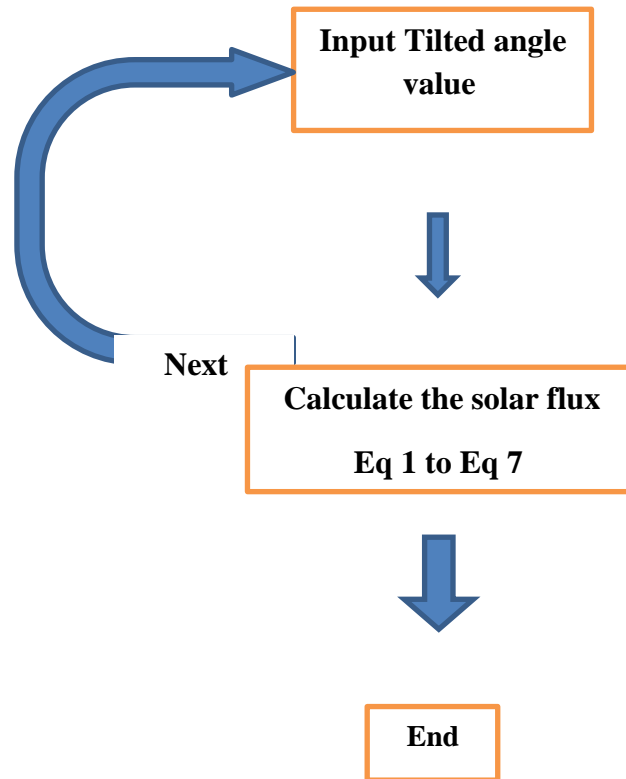


Fig (1) Common Angles in solar application [6]

3-System modeling:

The tilted angle model is programmed using Engineering Equation Solver (EES); all governing equations are performed on EES. EES incorporates the programming structures of C and FORTRAN with a built-in iterates, thermodynamic and transport property relations, graphical capabilities, numerical integration, and many other useful mathematical functions. By grouping equations that are to be solved simultaneously, EES is able to rapidly solve large numbers of transcendental equations. In this study an exact solution is used as a way to solving the module, The Flow chart of the present program is shown below.



Fig(2) System modeling Flow chart

4- Results and Discussion:

4-1 Monthly Optimum Tilted Angle:-

Fig (3) shows the effect of tilted angle variation of photovoltaic (PV) cell on the collected solar energy located in Basrah city for all months of the year. From this figure, as the tilted angle increases the collected solar energy flux will increase until reach to maximum value due to the increasing in the amount of the solar radiation normal component that incident to the cell surface .After this value of tilted angle the collected solar energy flux will decrease, therefore the optimum monthly tilted angles can be indicated. Each month has its optimum tilted angle due to the difference in solar characteristics of these months (solar day number that affect the declination angle).

From Fig(3) , the maximum solar flux occurs at Jun ,that is due to high angle of declination .the higher angle of declination leads to reduce the path of the sun ray, so it reduces

the solar beam absorbing and scattering and increased the flux of solar energy that reaches to earth surface see Fig(4) and Fig(5)

Fig (6) show the effect of tilted angle of PV cell variation on the collected energy located in Amarah city, where Fig(7) show the effect of tilted angle of PV cell variation on the collected energy located in Nasiriyah city for all months of the year . From these figures, these cities (Basra ,Amarah and Nasiriyah) have different in

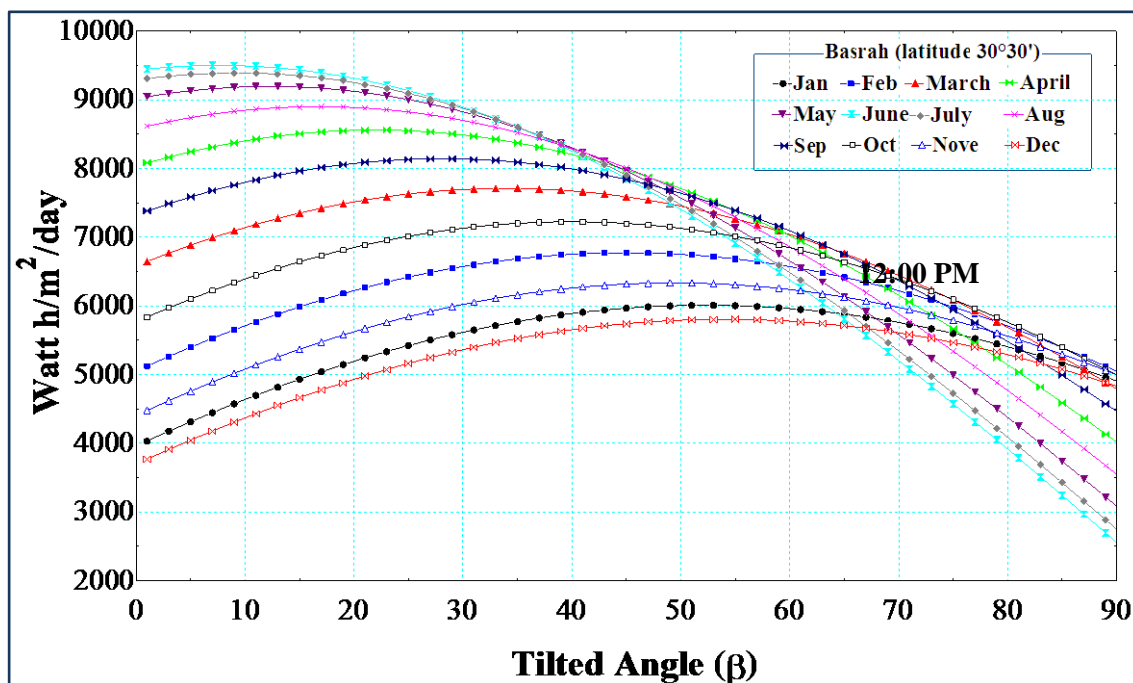


Fig (3) Effect of PV Cell Tilted Angle Variation on Collected Solar Flux located at Basrah city around months of the year

longitude and latitude therefore for this reason the optimum monthly tilted angle of these cities will different from one to other. And The total solar radiation was the highest in Basrah city because it has the nearest latitude angle from equator as compared with other cities (Amarah and Nasiriyah) .

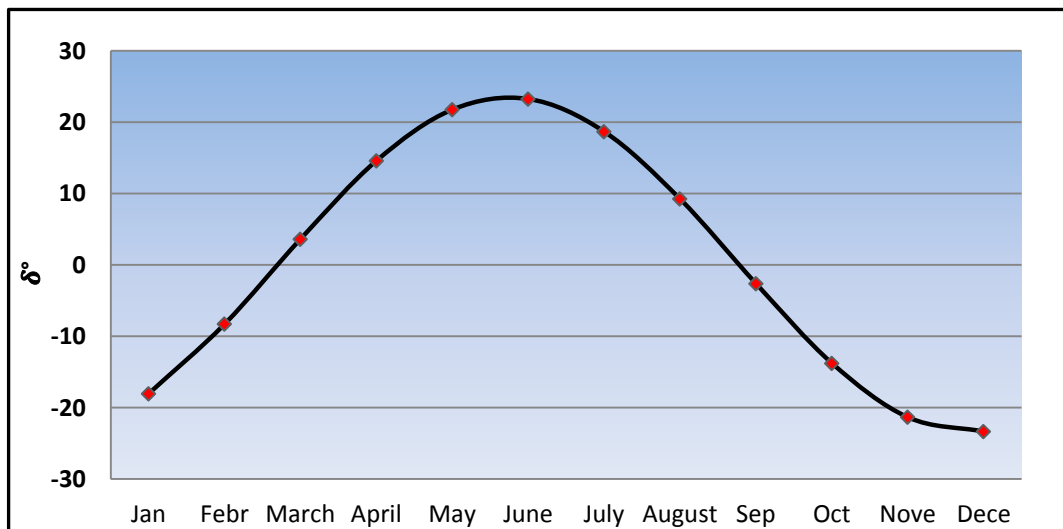
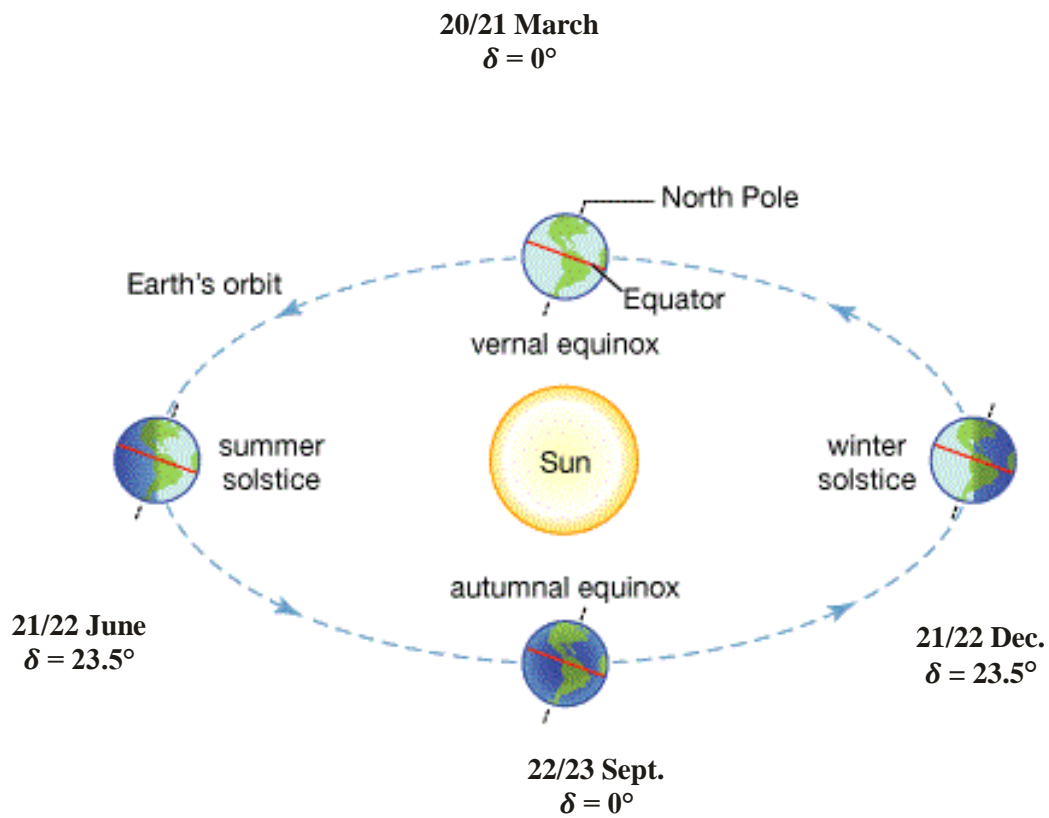


Fig (4) Ecliptic plane and position of the earth at the winter and summer solstices, and also at the spring and autumn equinoxes[12]

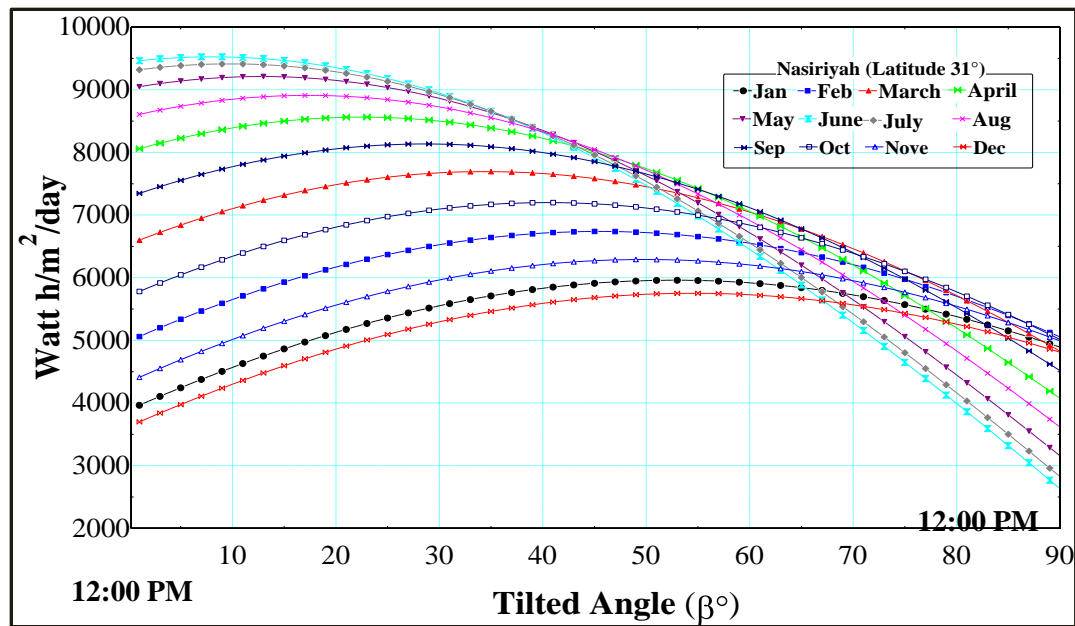


Fig (6) Effect of PV Cell Tilted Angle Variation on Collected Solar Flux located at Nasiriyah city around months of the year

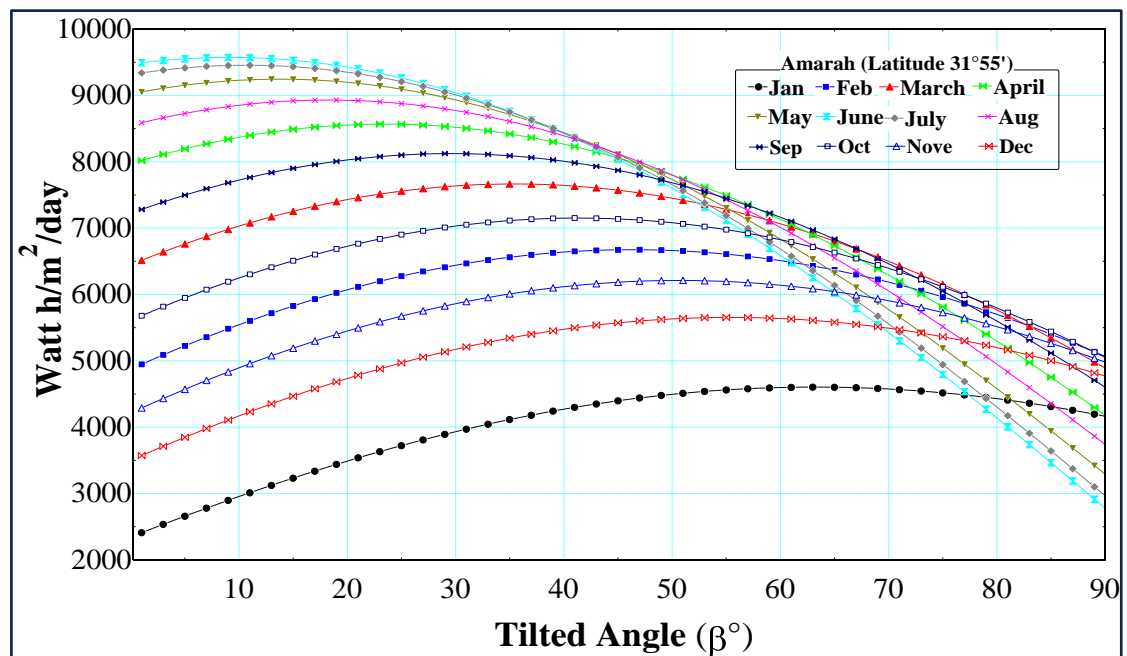


Fig (7) Effect of PV Cell Tilted Angle Variation on Collected Solar Flux located at Amarah city around months of the year

4-2 Yearly Optimum Tilted Angle:-

The using of stationary system with optimum yearly tilted angle is more efficient from using tracking system with daily or monthly tilt angle, because of tracking system maintenance cost and energy requirement to operate the system.

The tilted angle varies over range from 0° to 90° . The variation of tilted angle was adopted over the days of the year, and an average value of collected solar energy was taken as a method to find the collected energy by any tilted angle.

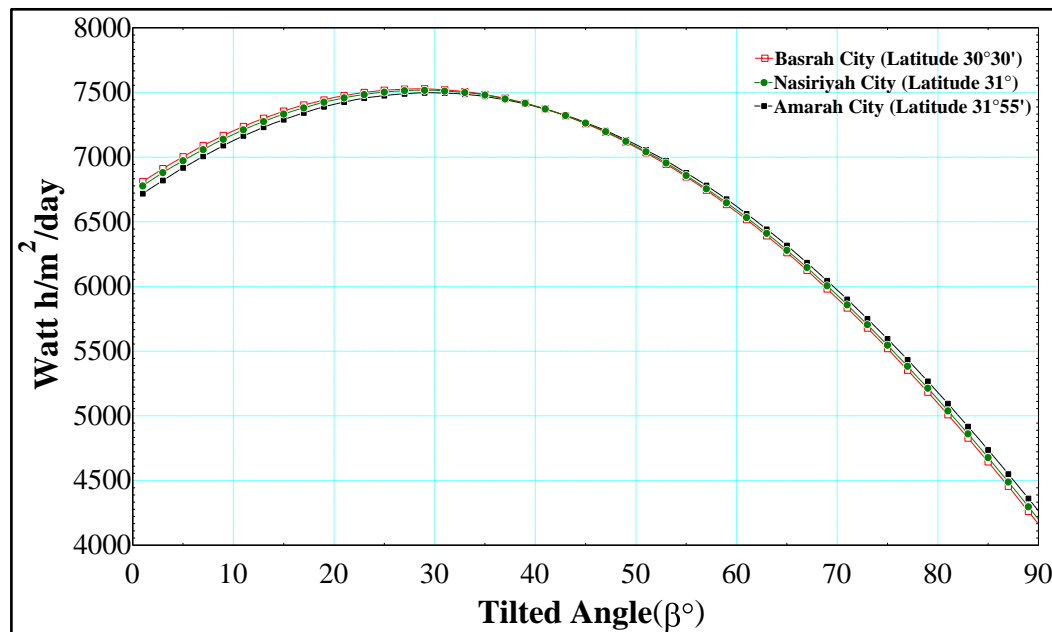


Fig (8) Effect of PV Cell Tilted Angle Variation on Collected Solar Flux located at Amarah city around months of the year

Fig (8) gives solar energy flux around the year for three cities Basrah, Nasiriyah, and Amarah, From this figure there is one angle that give overall maximum value of collected solar energy flux . This value of angle can be taken as optimum yearly tilted angle, so that this angle will deferent from monthly optimum tilted angle with less decrease in collected energy as compared with monthly optimum tilted angle that give the highest solar energy at the same day of the year (12% less from solar energy collected with optimum monthly tilted angle at April for Basrah city) .

CONCLUSION

Many recent studies shows that the optimum tilted angle of photovoltaic cell is approximately equal to the latitude at the given location, this study showed that the optimum tilted angle(monthly or yearly) is not equal to the latitude of the city.

From results the optimum monthly tilt angle of the given location is differs from month to other due to deferent in the declination angle , and the maximum solar flux occurs at Jun which have high declination angle.

Also showed that the optimum yearly tilt angle for Basrah city (latitude $30^{\circ} 30''$) is 28° , where for Amarah city (latitude $31^{\circ} 55''$) is 30° , and for Nasiriyah city(latitude 31°) is 29° . From all these values the optimum tilted angle is not equal to latitude of the given location.

REFERENCES

1. Tom Markvart and Luis Castafier “Practical Handbook of Photovoltaics: Fundamentals and Applications”, 2003.
2. Kyoto Protocol To The United Nations Frame work Convention On Climate Change .1998, UNITED NATIONS, FCCC/INFORMAL/84.
3. Soulayman, S. S. H., On “the optimum tilt of solar absorber plates”. Renewable Energy, 1991. 1, 551-554.
4. Vilela, O.C.; Fraidenraich, N.; Tiba, C. , “Photovoltaic pumping systems driven by tracking collectors: experiments and simulation”. Solar Energy jornal, 2003, vol.74 no.1, 45-52.
5. Hamdy K. Elminir , Ahmed E. Ghitas, F. El-Hussainy, R. Hamid a, M.M. Beheary, Khaled M. Abdel-Moneim, “Optimum solar flat-plate collector slope: Case study for Helwan, Egypt”. Energy Conversion and Management 47, 2006, 624–637.
6. KORAY ULGEN, “Optimum Tilt Angle for Solar Collectors”, Energy Sources, Part A, 28:1171–1180, 2006.
7. Tian Pau Chang . “Study on the Optimal Tilt Angle of Solar Collector According to Different Radiation Types”, International Journal of Applied Science and Engineering, 2008. 6, 2: 151-161.
8. Can Ertekin , Fatih Evrendilek and Recep Kulcu , “Modeling Spatio-Temporal Dynamics of Optimum Tilt Angles for Solar Collectors in Turkey”. Sensors 2008, 8, 2913-2931.

9. Kamal Skeiker ,2009. “Optimum tilt angle and orientation for solar collectors in Syria”. Energy Conversion and Management , 2009.50.2439–2448.
10. Romdhane Ben Slama , “Incidental Solar Radiation According to the Solar Collector Slope -Horizontal Measurements Conversion on an Inclined Panel Laws”. The Open Renewable Energy Journal, 2009, 2, 52-58.
11. Ashok Kumar ,2011 “optimization Of Tilt Angle For Photovoltaic Array” International Journal of Engineering Science and Technology (IJEST), Vol. 3 No. 4 Apr 2011.
12. Ursula Eicker . “Solar Technologies for Buildings”,1st edition 2001, University of Applied Sciences, Stuttgart, Germany

Nomenclature

<u>Symbols</u>	<u>Description</u>	<u>Unit</u>
D_H	Diffused solar radiation received by the horizontal plane	W/m^2
D_i	Diffused solar radiation received by the titled photovoltaic cell	W/m^2
E	Energy theoretically received per m^2 and per day	$kWh/m^2/day$
G_i	Global solar radiation received by the collector	W/m^2
G_H	Global solar radiation received by the horizontal plane	W/m^2
h_s	Height of the sun at true solar midday	$(^\circ)$
N	Number of solar day	
I_D	Direct solar flux	W/m^2
θ	Angle formed by the normal to the collector and the solar rays incident to the collector	$(^\circ)$
θ_z	Azimuth angle	$(^\circ)$
α	Albedo	

β	Photovoltaic cell tilted angle	(°)
φ	Latitude of the city	(°)
δ	Declination angle of the sun	(°)
ΔD	Duration of the day	

Environmental impact assessment of domestic effluents on water quality of Tigris River discharged from Wasit Thermal Power Plant

Ali N. Hello, PhD

**Department of Civil Engineering, Wasit University,
Wasit, Iraq**

Email address: alinasser3@yahoo.com

Ali J. Jaeel, PhD

**Department of Civil Engineering, Wasit University,
Wasit, Iraq**

Email address: alijwied_2004@yahoo.com; alijwied@gmail.com

ABSTRACT

Present study was conducted at Tigris river, near Wasit Thermal Power Plant (WTPP) in Al Zubiadiyah city to evaluate the impact of discharging domestic sewage during construction period (2010-2016) on water quality of the river; to assess the level at which effluents discharged from WTPP affect the quality of Tigris river water; and to compare the quantity of pollutants in the water with the acceptable limits of Iraqi Standards. Observation recorded during the three months study depicted that the river is polluted in certain areas downstream the river as comparatively higher values of biological oxygen demand (BOD) and chemical oxygen demand (COD) were recorded. The level of total dissolved solids (TDS), dissolved oxygen (DO), chemical oxygen demand (COD), biological oxygen demand (BOD), total hardness, sodium ion, and sulfates (SO_4) in the water sample were quite high. With the exception of pH, all other physical-chemical parameters measured are between 100% and 180% higher and have exceeded the maximum permissible limit given by the permissible Iraqi standards. The domestic wastewater is discharged directly to river without any treatment during this period (construction period), there is tendency of these pollutants to persist in the water and its uptake may cause long term health problems when the water is used as drinking water, especially in areas near the point

of discharge, since there is an intake of a water compact unit 1 km downstream from the point of discharge (Al-Bokhauder village), as well as the adverse effects on plants when the contaminated water used for plant irrigation .

Key words: domestic effluent, river water quality, pollution.

تقييم الأثر البيئي لمياه الصرف الصحي لمحطة كهرباء واسط الحرارية على جودة مياه نهر دجلة

الخلاصة

أجريت الدراسة الحالية على نهر دجلة قرب مدينة الزبيدية في محافظة واسط وبالتحديد عند مشروع محطة واسط الحرارية لتوليد الطاقة الكهربائية في مدينة الزبيدية وذلك لتقييم الأثر البيئي الناتج عن تصريف مياه الصرف الصحي وخلال فترة إنشاء المحطة (٢٠١٠ – ٢٠١٦) على نوعية مياه نهر دجلة مع مقارنة قيم الملوثات المطروحة مع الحدود المسموح بها ضمن المواصفات العراقية . ومن خلال النتائج التي تم التوصل إليها طيلة فترة الدراسة (ثلاثة أشهر) لوحظ إن منطقة أسفل النهر ملوثة بنسبة عالية جدا من الملوثات (الأملاح المذابة الكلية ، الأوكسجين المذاب ، الأوكسجين البايولوجي المطلوب ، الأوكسجين الكيماوي المطلوب، العسرة الكلية ، ايون الصوديوم ، الكبريتات) في نماذج المياه المأخوذة حيث كانت تراكيزها عالية جدا. وفي ما عدا قيم الأس الهيدروجيني فأن كل الملوثات الكيميائية والفيزيائية كانت تزيد عن الحدود المسموح بها حسب المواصفات العراقية بأكثر من (١٠٠% – ١٨٠%) . إن مياه الصرف الصحي كانت تصرف مباشرة إلى نهر دجلة دون أي معالجة تذكر وخلال الفترة الحالية (فترة إنشاء المشروع) وهناك ميل قوي لهذه الملوثات إن تبقى في الماء ويمكن إن تسبب العديد من المشاكل الصحية على المدى الطويل عند استخدامها كمياه شرب وخصوصا على المناطق القريبة على نقطة التصريف حيث إن هناك مأخذ لوحدة ماء مجمعة تابعة لقرية البوخضر يبعد حوالي ١ كم عن نقطة التصريف ، إضافة إلى ذلك التأثير السلبي على النباتات عند استخدام تلك المياه الملوثة في ري المزروعات.

1. Introduction

Water is the basic and primary need of all vital life processes and it is now well established that the life first arose in aquatic environment. Ever since the pre-historic times man has been intimately associated with water and the evidences of past civilization that all historic human settlements were developed around inland freshwater resources have conclusively proved it. Even today it is the major consideration for all socio-economic cultural, industrial and technological developments. Besides drinking, water is also used for fish and aquaculture, irrigation hydropower generation etc. but these days water the elixir of life is becoming more and more unfit and dearer to mankind due to unwise use, neglect and mismanagement.

According to the World Commission on water for the 21st century, more than half of the world's major rivers are so depleted and polluted that they endanger human health and poison surrounding ecosystems. When waste water finds its way into any water body it pollutes the water, water pollution is primarily associated with domestic and industrial waste. Both types of waste-water pose threats to water quality which may be classified into health hazards and sanitary nuisances. Many fresh water resources are contaminated through human activities. Each day some 25,000 people (in the developing countries) are said to die from their everyday use of wastewater. Many millions more suffer from frequent and devastating water borne illnesses,[1]. About half of the people that live in developing countries do not have access to safe drinking water and 73% have no sanitation, some of their wastes eventually contaminate their drinking water supply leading to a high level of suffering [2]. Every human use of water, whether for drinking, irrigation, and industrial processes or for recreation has some quality requirements in order to make it acceptable. This quality criterion can be described in terms of physical, chemical and biological properties of such water[1]. In many places both surface and ground water is fouled with industrial, agricultural, and municipal wastes.

Today water resources have been the most exploited natural systems. Pollution of water bodies is increasing steadily due to rapid population growth, industrial proliferation, urbanization, increasing living standard and wide sphere human activities. Most of our cities developed without proper development plan.

Consequently sewage systems of these cities are not well planned. Therefore wastes of homes and industries mixed with the catchment areas of water by the fault sewage system.

Water quality studies have focused on cases where sever pollution problems are arises, especially in heavily populated urban areas. For example Baghdad city is over populated and produced a huge amount of wastewater from different sources which are disposed into Tigris river directly or after treatment. In the last few years, an increase of wastewater directly disposed in the river using pump stations of storm sewer network have caused high pollution levels in the river's water [3].

Most potential negative environmental impacts from the application of recycled water to the environment come from recycled water's origin as wastewater. These impacts include other water resources, potential contamination of surface and groundwater sources. Public health hazards, and other environmental impacts that may directly or indirectly affect the public. Fortunately, very few significant negative impacts have ever occurred. It is important that all public water systems serve water of the best possible quality to their customers[4].

In Wasit province (middle of Iraq), Tigris river facing the effect of conservative pollution due to the continuous discharge of domestic wastewater in it during the current construction phase (2010-2016) of Wasit Thermal Power Plant (WTPP) project. The present research is to study the effect of wastewater pollutants discharged from the residential complex directly into the river on the water quality during the construction period.

2-MATERIALS AND METHODS

2-1 Water sampling

Collection of water samples was done in the morning between 9am and 10am. These samples were collected using Grab method which according to World Bank, 1988 [5]; Samples were collected into clean 2liter plastic bottles and were stored in an ice box of 4°C and were taken to the laboratory within twenty-four hours for analysis. Water samples were collected by lowering pre-cleaned plastic bottles into the bottom of the water body, 30 cm deep, and allowed to over flow before withdrawing. Ten sampling

points were used and the sampling points are approximately 1km away from each other. A total of 40 samples were analyzed. Four samples were collected from each of the ten sampling points. The first location was 1km up stream; the second location was at (Chinese residential camp) waste water discharge point. The third to the eighth locations were at the 1km, 2kms, 3kms, 4kms, 5kms, and 6kms, downstream. The study was carried out through three months.

2-2 General description of the Project environment

Wasit Thermal Power Plant (WTPP) is located in the land of Wasit governorate. The station is located about 120 km southeast of Baghdad Fig. (1). Water source which the project depends on is the Tigris river, which the right bank of the river about 100 meters from the project.



Figure (1) Location of Wasit thermal power plant project in Wasit Province.

2-3 Domestic Wastewater discharge during WTPP construction phase

We have been calculating how much drainage discharged by Chinese camp which contains more than 1,500 workers and the adoption of the international standard for quantitative feedback per person per day and 300 liters of water is the amount of 450,000 liters per day or the equivalent of 450 cubic meters of wastewater per day and several samples of water posed to the river directly have been taking regularly (Fig. 2). For the purpose of checking a range of environmental tests have shown that wastewater is very far from Iraq and global environmental determinants. Table 1 shows the results of the examination rate for several domestic wastewater samples. Waste water as sewage discharged to the irregular and underground septic tanks is a collection of scattered drilling and deployed dozens of meters away from the right bank of the Tigris river, the dimensions of the each underground septic tank are 40

meters length by 15 meters width by 6 meters depth, and roofed with sheets of aluminum. The wastewater is discharged from these underground tanks directly into the Tigris river through the trenches with dimensions 1.25m width and depth of 1.5 meters or through pipes diameter 8 inches. While the other section of the underground tank (reservoirs) water is drained through the nomination process in the soil where the water level is higher than the level of the Tigris river, the nomination process of this waste water from these septic tanks to the river are easy and fast. . However the quality of river water deteriorates at several places due to inflow of sewage. The present study deals with the assessment of the impact of pollution on the Tigris river water quality along the stretch of Wasit Thermal Power Plant (WTPP) borders with the river.



Figure (2) Chinese camp -underground septic tanks with directly wastewater discharge to the river.

2-4 Physicochemical Analyses

The following parameters were analyzed during the course of study

1. pH

The hydrogen ion concentration is the indicator of acidity and alkalinity of any aqueous system. During present investigation pH was measured with the help of a pH meter.

2. Dissolved Oxygen

Dissolved oxygen level of the samples was measured with the D.O meter. The electrode was dipped into each sample, after it had been rinsed, then readings were taken and the description was given in APHA[6].

3. Total Dissolved Solids

TDS test by filtration followed by oven drying 200 ml (V) of sample was filtered by filter paper to separate the suspended solid, then the beaker was weighted (A) and filled by the filtered sample. The sample was dried in the oven at 105°C for 5 hours, the beaker with the dissolved solid was weighted again (B) [7]. Then TDS was calculated by:

$$\text{TDS} = \frac{B - A}{V} \quad (1)$$

Where:

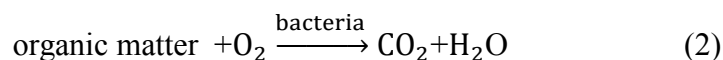
V= volume of sample, (L).

A=weight of beaker filled by filtered sample, (mg).

B= weight of beaker with the dissolved solid, (mg).

4. Biochemical Oxygen Demand (BOD)

Biological oxygen demand is an indirect measure quantifying the amount of oxidizable organic matter in wastewater. It is defined as the mass of oxygen that would be required for the complete decomposition of the organic matter in a given volume of water (usually in mg/l), given sufficient time (Clesceri et al. 1998). The standard five day BOD test (BOD₅) quantifies the extent of oxygen depletion in a sample over 5 days. Excessive BOD in effluent discharged to natural bodies of water can quickly cause anoxic conditions for fish and other aquatic life as decomposers deplete available DO through respiration. Kadlec and Knight (1996) simplify the multitude of processes breaking down BOD through the following equation, analogous to cellular respiration [8]:



They admit that equation (2) overlooks two significant issues: (i) that other pathways exist for breaking down organic matter (e.g. anaerobic methanogenesis), and (ii) that other biological wetland processes demand oxygen (e.g. nitrification).

The first reading of D.O1 was taken with oxygen meter and after 5 days of incubation of water samples in 20°C without light, the second reading of D.O2 was taken. The BOD was determined by the below equation and expressed in mg/L. [9]

$$\text{BOD5} = \frac{\text{D.O1}-\text{D.O2}}{\text{P}} \quad (3)$$

Where:

D.O1= dissolved oxygen of diluted sample immediately after reparation, mg/l.

D.O2= dissolved oxygen of diluted sample after 5 days incubation at 20°C, mg/l.

P = decimal volumetric fraction of sample used (dilution factor).

5. Chemical Oxygen Demand (COD)

Chemical oxygen demand (COD) test was conducted in accordance to the procedures outlined in the *Standard methods* (APHA, 1998) using COD reactor (Model: WTW CR 2200, Germany) and Photometer (Model: WTW S6, Germany).

6.Total hardness (T.H)

Total hardness (T.H) test as CaCO_3 is done by titration method. A solution was prepared from 10 ml of water sample (V1) and 10 drops of buffer solution (pH=10) in order to give the alkalinity characteristics, the none drop (10 mg) of Erio chrome black T reagent was added, so the solution became pink. This solution was titrated with (1 normality)(N) of H_2SO_4 acid until the solution became blue, the volume of acid was records(V) [10].

The total hardness was calculated by:

$$\text{Total Hardness} = \frac{\text{V} \times \text{N} \times \text{M}_w}{\text{V1}} \times 1000 \quad (4)$$

Where:

V= volume of H_2SO_4 .

N= normality of H_2SO_4 .

M_w = the molecular weight of CaCO_3

V1= volume of water sample, ml.

7. Na^+ Test by Photometer (S6) Method

This method was done by using Atomic Absorption Spectrometry using Photometer (Model: WTW S6, Germany). This photometer allows measurement of convenient rapid tests by inserting the coded cuvette (Na^+) and read the result directly.

8. SO_4^- Test by Photometer (S6) Method

This method was done by using Atomic Absorption Spectrometry using Photometer (Model: WTW S6, Germany). This photometer allows measurement of convenient rapid tests by inserting the coded cuvette (SO_4^-) and read the result directly.

3-RESULTS

1- From the laboratory tests, the mean concentration of biological oxygen demand (BOD) at the point of entry (main discharging point 0km) was 280 mg/l (Fig.3) which is higher than the permissible value according to the Iraqi standards, this discharging adversely affects the quality of water and gradually ended up to the 8km where the BOD concentration becomes 30 mg/l which is lower than the permissible value (40 mg/l).

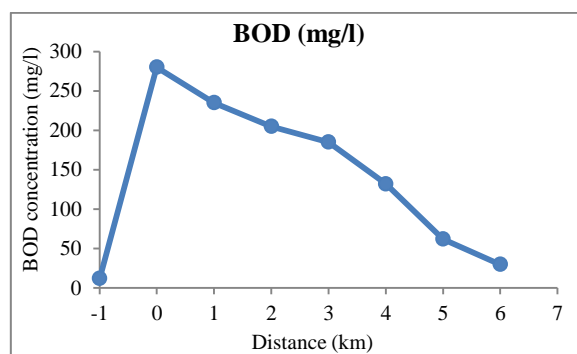


Figure (3) Variation of BOD concentration with distance

2-The COD concentration level increases at the main discharging of river at a point 0km by 265% of the permissible value (Fig.4). After 5km from the point of entry the COD concentration decreases to 95 mg/l which is an acceptable value.

Table 1 Mean value of physical-chemical parameters

Parameter	Upstream -1km	Point of Entry 0km	1km	2km	3km	4km	5km	6km	Max permissible Iraqi Standard (mg/l)
COD (mg/l)	25	365	330	256	245	170	95	42	< 100
BOD (mg/l)	12	280	235	205	185	132	62	30	< 40
Dissolved Oxygen (mg/l)	9	1.2	1.8	3.5	4.1	5	6.5	7.2	-
Total Dissolved Solids (mg/l)	450	1200	1119	998	975	945	610	480	< 1000
SO ₄	45	425	389	370	365	360	239	187	< 250
Total Hardness	398	877	832	765	720	578	454	400	< 500
Na ⁺	32	78	65	51	35	34	33	30	< 150
PH	8.4	7.1	7.3	7.5	7.8	8.1	8.2	8.2	6-9.5

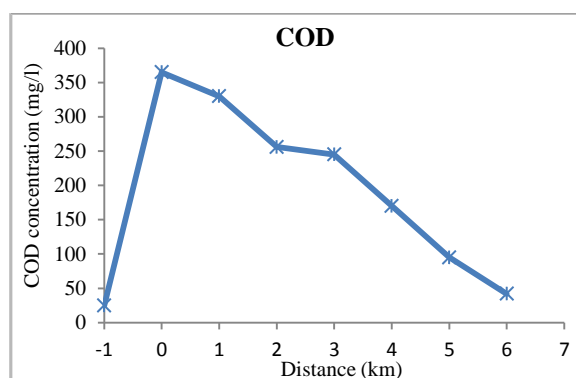


Figure (4) Variation of COD concentration with distance

3- The concerning the dissolved oxygen concentration, Fig (5) shows that the river was fully saturated with dissolved oxygen (1km upstream) which was 9 mg/l. Low dissolved oxygen and under saturation observed at the sewage outfall (0km) is due to increasing biochemical oxygen demand requiring oxygen to break down organic matter brought in by the sewage. After the first km beyond the point of entry the dissolved oxygen concentration increases gradually until it becomes 7.2mg/l at the station 6km downstream.

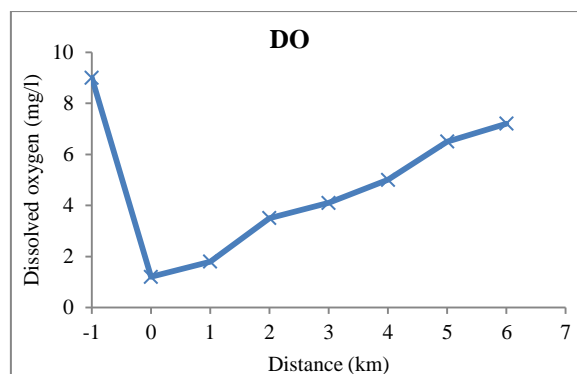


Figure (5) Variation of DO concentration with distance

4-The pH values decrease at the discharge point, Fig (6) and increase at the other stations downstream. All the values of pH at the ten stations were at an acceptable range of Iraqi standards.

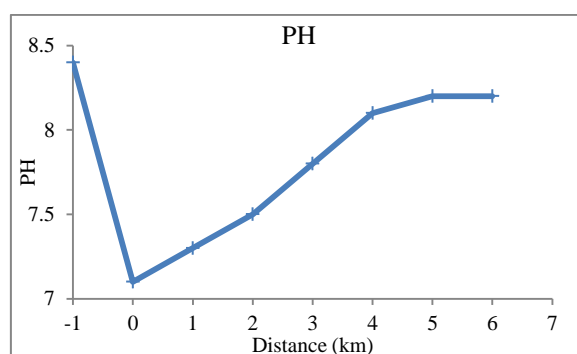


Figure (6) Variation of pH concentration with distance

5-The phosphates concentrations were higher in the vicinity of sewage outfalls (425 mg/l) which is about 170% higher than the permissible value according to the Iraqi standards. There was a slow dissipation of phosphates from a higher concentration at the pollution source to near the station at 4km. The lowest concentration was recorded at the station 6km about 187 mg/l.

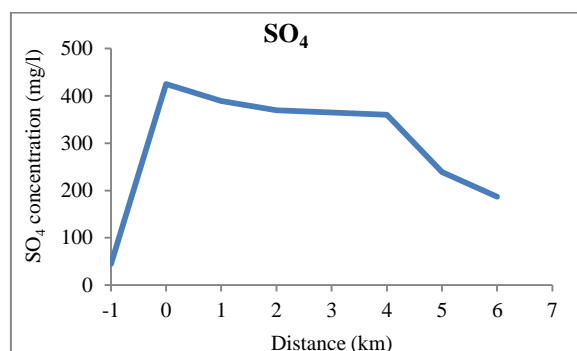


Figure (7) Variation of SO₄ concentration with distance

- 6- The total dissolved solid (TDS) concentrations varied between 480 - 1200 mg/L (Fig. 8) in all the study sites beyond the point of entry, and ranged from a minimum of 480 mg/L at the station 6km to a maximum of 1200 mg/L at the station 0km as an average. The high dissolved solids recorded in could be because of domestic effluent discharges and surface run-off from the cultivated fields which might have increased the concentration of ions. The observed high concentration of dissolved solids in the surface water is a pointer to the fact that there are intense anthropogenic activities along the course of the river and run-off with high suspended matter content.

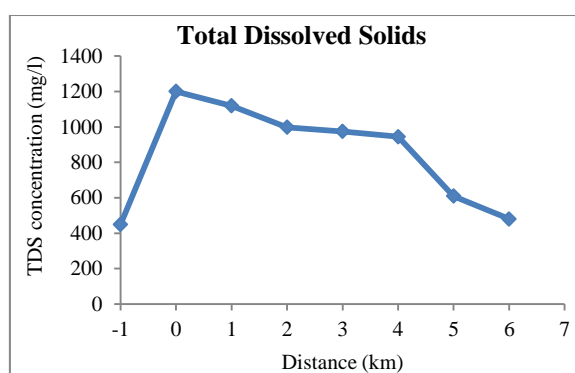


Figure (8) Variation of TDS concentration with distance

- 7- In spite of the maximum value of sodium ions concentration at the point of entry (Fig. 9), the concentrations conserve within the permissible values of Iraqi standards.

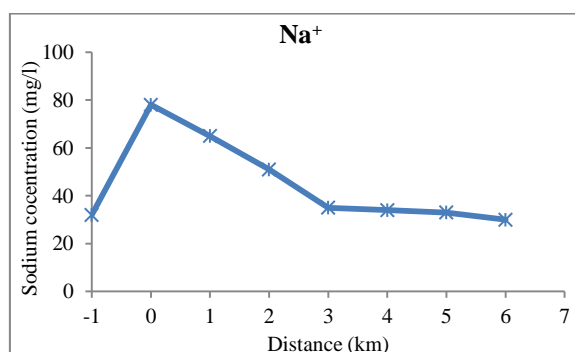
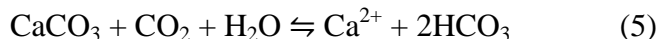


Figure (9) Variation of Na⁺ concentration with distance

- 8- Total hardness mainly depends upon the dissolved salts present in the water. The water is classified as very hard if the values exceed 180 mg/l, therefore water of the river can be considered as hard. Hard water also forms deposits that clog

plumbing. These deposits, called "scale", are composed mainly of calcium carbonate (CaCO_3), magnesium hydroxide $\text{Mg}(\text{OH})_2$, and calcium sulphates (CaSO_4). The following equilibrium reaction describes the dissolving/formation of calcium carbonate scales [11]:



As water moves through the soil and the rock, it dissolves very small amounts of minerals and holds them in solution. Calcium and magnesium dissolved in water are the two most common minerals that make water "hard." Calcium and magnesium ions can be removed by water softeners. In the present study, it has been found that the total hardness ranges from 400-877 mg/l at the stations 6km and 0km respectively (Fig. 10). This is due to discharge of domestic sewage, washing clothes, and animals in the river.

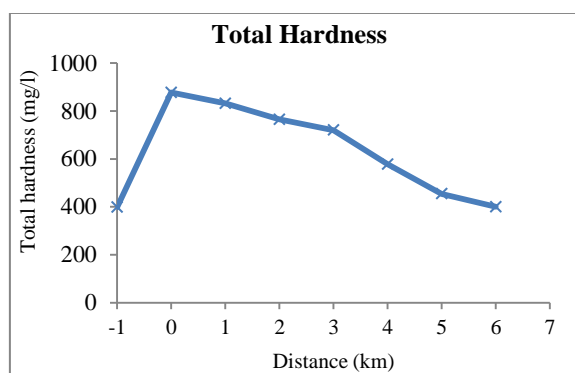


Figure (10) Variation of total hardness concentration with distance

4- DISCUSSION

The major sources of water pollution can be classified as municipal, industrial, and agricultural. Municipal water pollution consists of wastewater from homes and commercial establishments. For many years, the main goal of treating municipal wastewater was simply to reduce its content of suspended solids, oxygen-demanding materials, dissolved inorganic compounds, and harmful bacteria. In recent years, however, more stress has been placed on improving means of disposal of the solid residues from the municipal treatment processes. The basic methods of treating municipal wastewater fall into three stages: primary treatment, including grit removal, screening, grinding, and sedimentation; secondary treatment, which entails oxidation of dissolved organic matter by means of using biologically active sludge, which is

then filtered off; and tertiary treatment, in which advanced biological methods of nitrogen removal and chemical and physical methods such as granular filtration and activated carbon absorption are employed.

The impact of domestic discharges depends not only on their collective characteristics, such as biochemical oxygen demand and the amount of suspended solids, but also on their content of specific inorganic and organic substances. Three options are available in controlling domestic wastewater. Control can take place at the point of generation in the Chinese residential camp; wastewater can be pretreated for discharge to municipal treatment sources; or wastewater can be treated completely at the WTPP project and either reused or discharged directly into receiving waters.

The chemical composition of sewage varies from day-to-day or even from hour. Sewage water contains inorganic waste, which creates a problem of disposal, but apart from inorganic waste, undesirable organic matters, which are offensive and dangerous, are also present. Inorganic compounds of sewage water support the growth of harmful bacteria and other microorganisms, which sometimes lead to the epidemics among the human beings. Health standards are dependent upon efficient waste disposal. It has been observed that numbers of the serious diseases are transmitted through sewages. Gastrointestinal, typhoid fever, paratyphoid fever, cholera, and dysentery certain nematode infection, etc.

Tigris is an important river of the central part of Iraq supplies water to a large command area of Wasit province. The present investigation was aimed at assessment of water quality and thereby an estimation of pollution loads on the river just close to its origin. The study reveals that the water quality is poor and pollutants of both organic and inorganic origin are entering into the river, thereby deteriorating its water quality. The high concentration of BOD and COD are due to high concentration of decomposable organic matter in the domestic wastewater flowing from the Chinese residential camp. The increased concentration of TDS depicts high concentration of dissolved inorganic solids. It is evident from the study that the Chinese residential camp (during the construction phase of WTPP project) near the Tigris river are polluting it by discharge of wastewater. The severely pollution of water of Tigris river has rendered its water unfit for human consumption especially there are many villages downstream about 1km away from the project. Treatment of wastewater before

discharge in the river is the only means by which the problem of water pollution could be mitigated. During the present investigation, the water quality of Tigris river in the upstream was observed quite well in comparison to downstream of the river, which was found to be highly polluted due to discharge of municipal sewage through surface drains.

However, the obtained results from this study for all the parameters were much higher than the previously reported values [13], in spite of the fact that the range of values published in these literature were observed for a station located before distillery and downstream of point where untreated sewage from Bağıvar settlement.

Ali (1978) concluded that Tigris River in Baghdad area is highly polluted comparing with Euphrates and Abu- Graib stream. Al-Masri and Ali (1985) confirmed that discharging treated and untreated wastewater into river limited the use of water for different uses as it flows down stream. For evaluating water quality parameters Al-Masri and Ali (1985) were studied some water parameters such as: sulfate, Alkalinity, chloride, calcium, hardness, and magnesium in Tigris River through Baghdad city. The results of study have indicated that concentrations of hardness, sulfate, and calcium exceeded the allowable limits established by the Iraqi drinking water standards. Ghadban (1993), concluded that after the war on Iraq in 1991, most water intakes of treatment plants, were heavily polluted by sewage discharges causing ecological damage and public health hazards. Abd-Ali (1993), also concluded that war on Iraq in 1991, affected the bacteriological quality of the Tigris river in Baghdad especially down river at Dora site, as a result of discharging the material sewage to the river.

5- REFERENCES

- [1] WHO (2003). "The World Health Report: Shaping the Future: World Health Organization 1211 Geneva 27, Switzerland.
- [2] Vivan EL, Bashiru D, Adamu CI (2012). An Appraisal of Water Supply and Sanitation Situation in Some Selected Areas of Kaduna Metropolis. Published in GURARA J. Vocational Technol. Sch. Agric. Technol. NuhuBamalli Polytechnic, Zaria.

- [3] Dahr ,J.,(2004), " Pollution Chokes The Tigris; A Main Source of Baghdad's Drinking Water.
- [4] William, O. Maddous, (2001), "Water Resources Planning ", First Edition, p.98.
- [5] World Bank (1988). Pollution study on clean up river Kaduna. Part Creport. KEPA/ABUCONS.
- [6] APHA, AWWA, WPCF (1995). "Standard Methods for the Examination of Water and Wastewater."American Public Health Association, Washington, DC.
- [7] Young, J.C., G.N. ,Mcdermott &.Jenkins,(1981), Alterations in BOD Procedure for The 15th Edition of Standard Methods for The Examination of Water and Wastewater," J. Water Pollution Control.
- [8] Kadlec, R. H. and Knight, R.L. (1996). Treatment Wetlands. Lewis Publishers, CRC Press, Inc. Boca Raton, Fla.
- [9] Clesceri, L.S.,(1998), " Flow Injection Analysis for The Orthophosphate", Standard Methods for The Examination of Water and Wastewater, 20th Edition.
- [10] Rand and Greenburg, (1978), "Standard Methods for The Examination of Water and Wastewater", 4th Edition., Raven Press , New York . 619
- [11] Onwughara, I. N., Ajiwe, V. I. , Alaekwe, I. O. 2011, Impact Assessment Of Total Hardness On Borehole Waters In Umuahia North MUAHIA NORTH Local Government Area Of Abia State, Nigeria. VSRD-TNTJ, Vol. 2 (8), 2011, 358-369
- [12] Clesceri, L.S., A.E., Greenberg and A.E. Eaton, 1998, Turbidity Nephelo metric Methods' Standard methods for the Examination of Water and Wastewater, 20th Edition.
- [13] Varola, M., Gökotb, B., & Bekleyenb, A. (2010), Assesment of Water Pollution in the Tigris River in Diyarbakır, Turkey. Water Practice & Technology Vol. 5 No 1.
- [14] Abd-Ali. A.H. ,1993, "A Statistical Study on Some Effects of the Aggressive War upon the Quality of Water in the City Baghdad", M.Sc. Thesis, Build. And Const. Dept. University of Technology.

- [15] Ali, A.I. ,1978,"Study the Bacterial Quality of Water in Iraq", M.Sc. Thesis, Agr. College, University of Baghdad.
- [16] Al-Masri N.A. and Ali A.A. ,1985, "Effect of Domestic and Industrial Wastewater Discharge on Pollutant Variation in River Tigris", Proceeding of Iraq Conference on Engineering,IDE,pp.467-474.
- [17] Ghadban, F.D. 1993, "Evaluation of Some Environmental Effects in Iraq (Water and Wastewater Treatment Plants)", M.Sc. Thesis, College of Eng., University of Baghdad.

Dynamic Finite Elements Analysis of Coaxial Dual Rotor System Using MatLab

Dr. AMEEN AHMED NASSAR

Assistant Professor, Department of Mechanical Engineering, College of Engineering,

University of Basrah.

ameen.nassar@uobasrah.edu.iq

Abstract

Dynamic analysis of coaxial dual rotor system was demonstrated in this paper through the use of finite element script files developed using matlab. A coaxial rotor system, generally employed in the aircraft engines to save space and keep the weight to minimum, and for the importance of this application it was considered for this analysis. The system was modeled using eight finite elements only with different shafts and bearings properties. The results obtained in this investigation were closed to other previous studies found in the literature. The developed matlab script files proved to be very essential for designers and analyst of coaxial rotors.

Keywords: Rotor dynamics, Coaxial Rotors, Finite Elements, Matlab.

تحليل ديناميكي باستخدام طريقة العناصر المحددة لمنظومة محور ثنائي متداخل باستخدام الماتلاب

الملخص

تحليل ديناميكي لمنظومة محور ثنائي متداخل وضحت في هذا البحث من خلال استخدام ملفات برامج عناصر محددة طورت لهذا الغرض باستخدام الماتلاب. منظومة المحاور المتداخلة عادة تستخدم في محركات الطائرات لتوفير المكان والابقاء على الوزن اقل ما يمكن، ولاهمية التطبيق تم اعتبارها لهذا التحليل. تم نمذجة المنظومة باستخدام ثمانية عناصر محددة فقط مع خواص محاور واسناد مختلفة. النتائج المستحصلة في هذه الدراسة قريبه جدا الى نتائج موجودة

بالمصادر باستخدام طرق تحليل اخرى. برامج الماتلاب المطورة في هذا البحث اثبتت انها مهمة لمصممي ومحلي الاهتزازات في المحاور المتداخلة.

كلمات مرشدة : ديناميكية المحاور، محاور متداخلة، عناصر محددة، ماتلاب.

1-Introduction

Most of the modern day machinery, used for power generation or for industrial applications, employ rotating components called rotors, which are the main elements for the power transmission. To meet the weight and the cost requirements, the present day rotors are made extremely flexible. This makes rotor dynamics as an essential part of the design. It involves the prediction of the critical speeds and the safe operating speed limits for the rotors, based on the evaluation of natural frequencies and plotting them on the Campbell diagram. An alternative option is to decide upon the variables in the design such as bearing specifications in terms of stiffness, bearing span, and coupling specifications, to keep the critical speeds away from the operating region.

However accurately these rotors are balanced, there will be some unbalance still left in the system. The response to make sure that the rotor does not rub against the casing, is an important aspect of the rotor dynamic analysis [1]. A common practice in the rotor dynamics analysis is to use beam models for both torsional and lateral analysis. Such an analysis required special attention to meet the capabilities for the modern day design of high-speed machinery. The beam type models require good modeling technique such as finite elements to approximate the three-dimensional rotor models. The accuracy of the beam modeling analysis is limited to how best the mass and stiffness in the system are captured. For a complex geometry such as the rotor, it is difficult to accurately capture these terms in rotor dynamics model. Finite element rotor dynamics modeling provide an accurate solution for such problems[2]. With the vision of applying different speeds to different elemental components, it is possible to simulate the rotor dynamic analysis of dual coaxial rotors, considering the effect of bearings, unbalance, and external torques. This provides an efficient real-life rotor dynamic simulation of the present day rotors which is more accurate than the conventional modeling approach.

2- Model and Analysis

To demonstrate the capabilities of the finite element model rotor dynamics, a study was carried out considering a coaxial dual rotor system given in Reference [3]. A coaxial dual rotor system is generally employed in the aircraft engines to save space and keep the weight to a minimum by having a hollow outer spool which mounts the high pressure compressor and the turbine running at a relatively higher speed through which an inner spool rotor mounts the low pressure compressor and the turbine rotors. A case study was taken [4], to validate the accuracy of the proposed approach, as shown in Fig.(1). The case study was simulated in MatLab using a developed script files depending on the rotor dynamics toolbox associated with Reference [5] (All the relevant equations for this analysis can be reviewed in this reference). First the rotor was modeled using eight beam elements and nine nodes. The bearing stiffness properties are simulated using two types of bearings. The developed model was shown in Figures (2) and (3) respectively.

3- Results and Discussions

For the above model, a vibration analysis was carried out including the bearing effects, the external torques, and the unbalance at different disk. The Campbell diagram was generated and shown in Fig.(4). It is clearly shows that due to the effect of bearings, both the forward whirl and the backward whirl frequencies decrease with speed. The effect of decrease in frequency with the increase in speed is more for backward whirls than for forward whirls. Similar results and conclusion were demonstrated for the same model, using Ansys solid modeling, in reference [4]. The root locus diagram is shown in Fig.(5). This figure shows clearly the stability of the analysis where the real eigen values and imaginary eigen value are coincide on the same vertical line for all range of the spin speeds. The model first four natural frequencies and mode shapes are shown in Fig.(6). This figure shows the behavior of the two rotors at different natural frequencies. The orbit plots of disk 1 relative other disks for the first six mode shapes are generated and shown in Figures (7-9) respectively. It is clear from these figures that the whirling orbits of the disks relative to each other are different depending on the mode natural frequencies and positions. An investigation on the effect of the unbalance in each disk on the response of the other disks with different spin speeds are carried out. The results were shown in Figures (10-13) respectively. These figures clearly show different response behaviors due to the different unbalance location on the disks.

4-Conclusions

From the above analysis, the following conclusions can be drawn:

- 1- The finite element analysis and matlab are good tools for dynamic analysis of rotors and easiest in implementation than using packages such as Ansys or Nastran.
- 2- The developed matlab script files can produced all the graphics needed for the illustration of the analysis.
- 3- The developed matlab script files proved to be very essential for designers of coaxial dual rotor systems.

5- References

- [1] Santos I.F., "Vibrations in Rotating Machinery", Lecture Notes, Department of Mechanical Engg., Technical University of Denmark, Denmark.
- [2] Rajan, M., Nelson H.D., and Chen W.J., "Parameters Sensitivity in the Dynamics of Rotor-Bearing Systems", J. Vib. Acouust. Strss and Rel. Des., Trans. ASME, Vol. 108, 1986.
- [3] Rao, J.S., Sreenivas, R., and Veeresh C.V., "Solid Model Rotor Dynamics", Paper presented at the Fourteenth U.S. National Congress of Theoretical and Applied Mechanics, BlacksBurg, VA, 23-28 June 2002.
- [4] Rao, J.S., Sreenivas, R., "Dynamics of Asymmetric Rotors using Solid Models", Proceedings of the International Gas Turbine Congress 2003, Tokyo, November 2-7, 2003.
- [5] Friswell M.I., Penny J.E., Garvey S.D., Lees A.W., "Dynamics of Rotating Machines", Cambridge University Press, 2010.

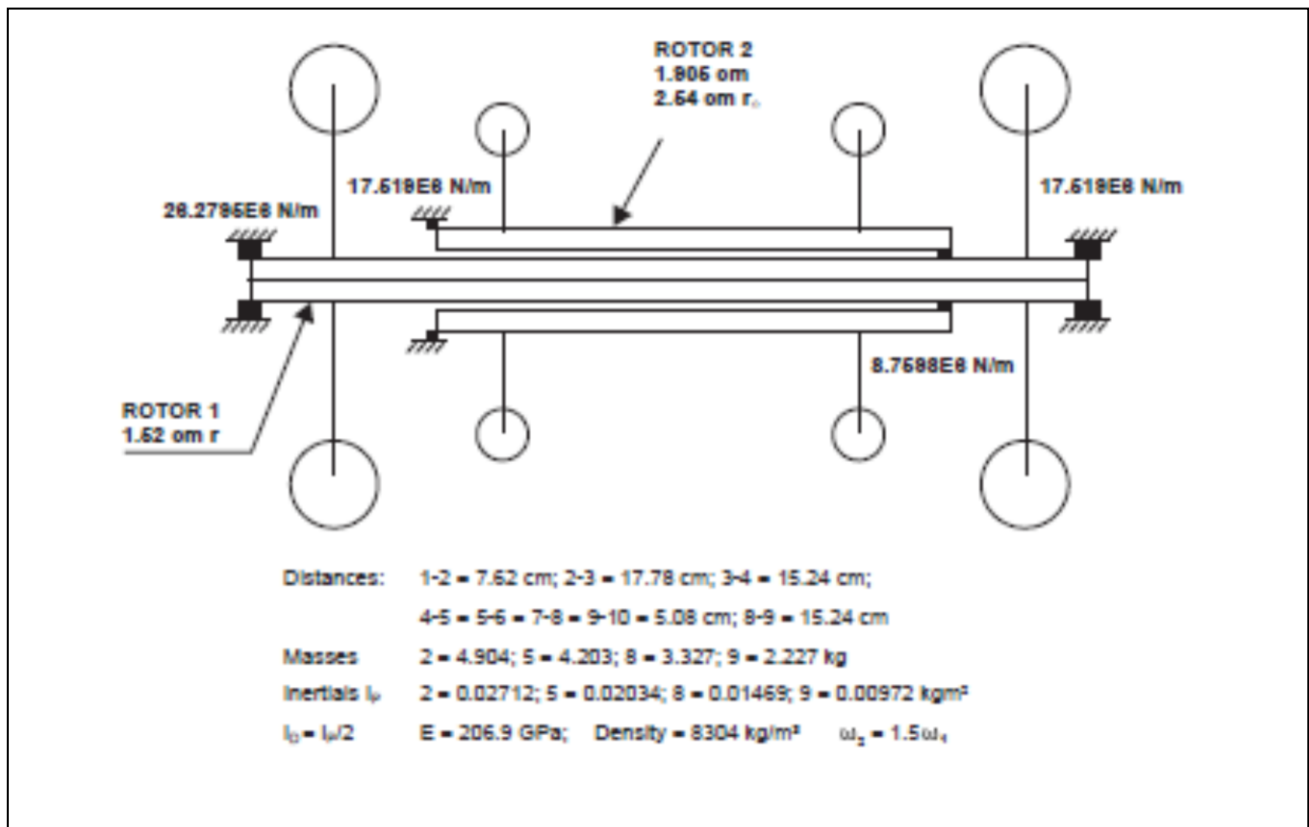


Fig.(1) Coaxial dual rotor system.

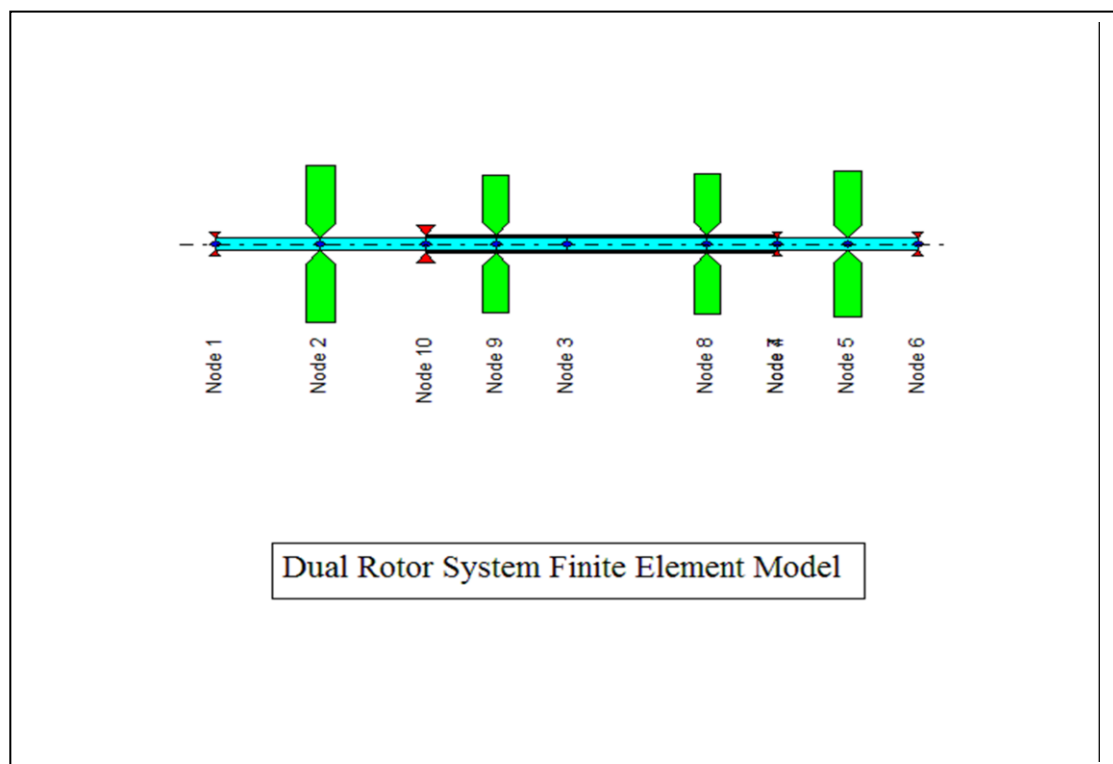


Fig.(2) Dual rotor system finite element model.

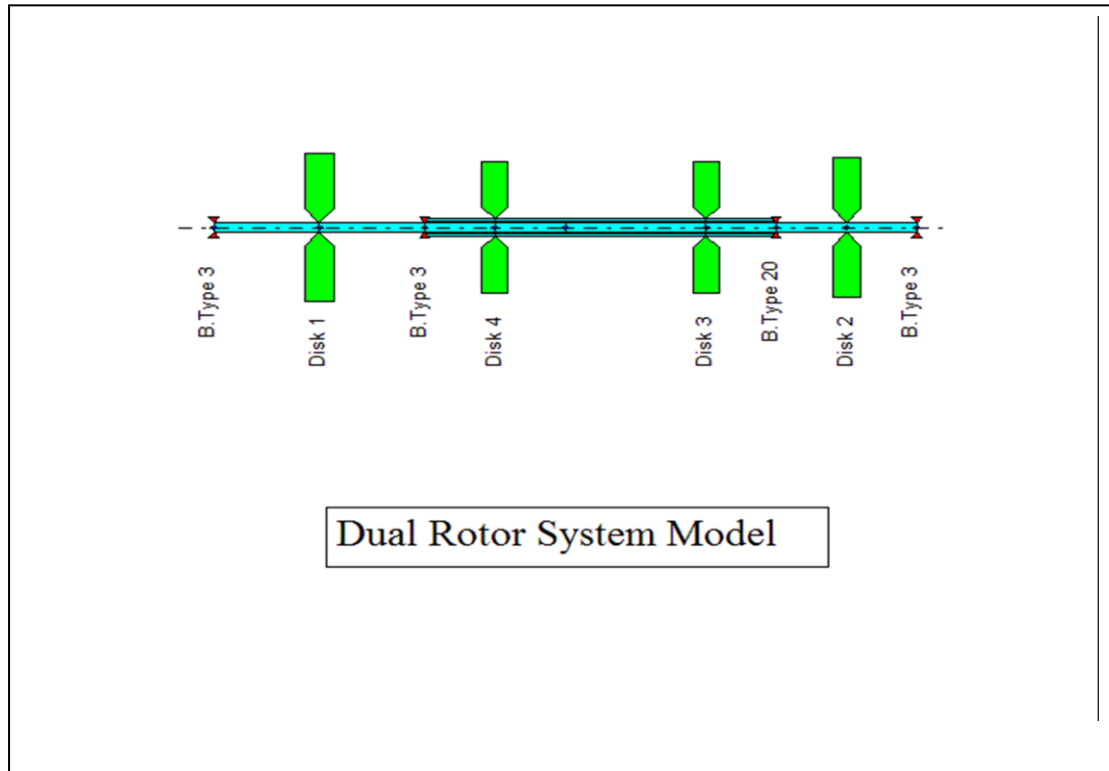


Fig.(3) Dual rotor system disks and bearings locations.

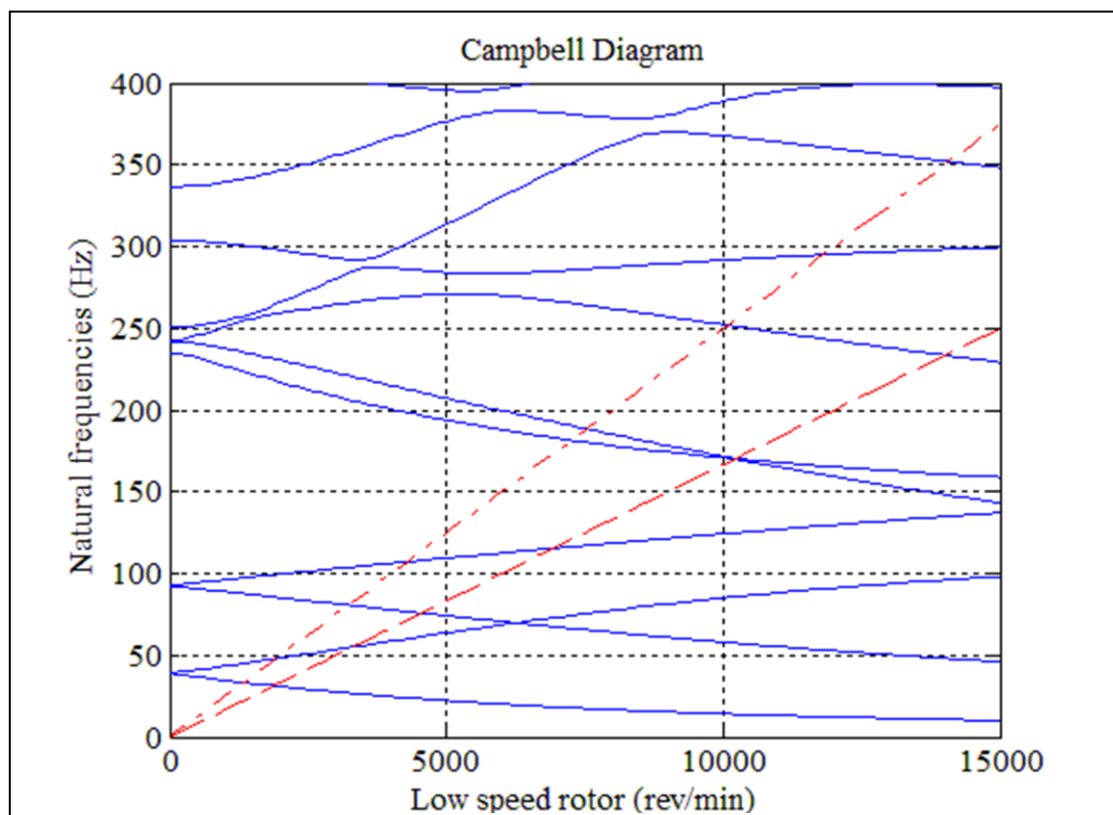


Fig.(4) Campbell Diagram for the model with bearing effects.

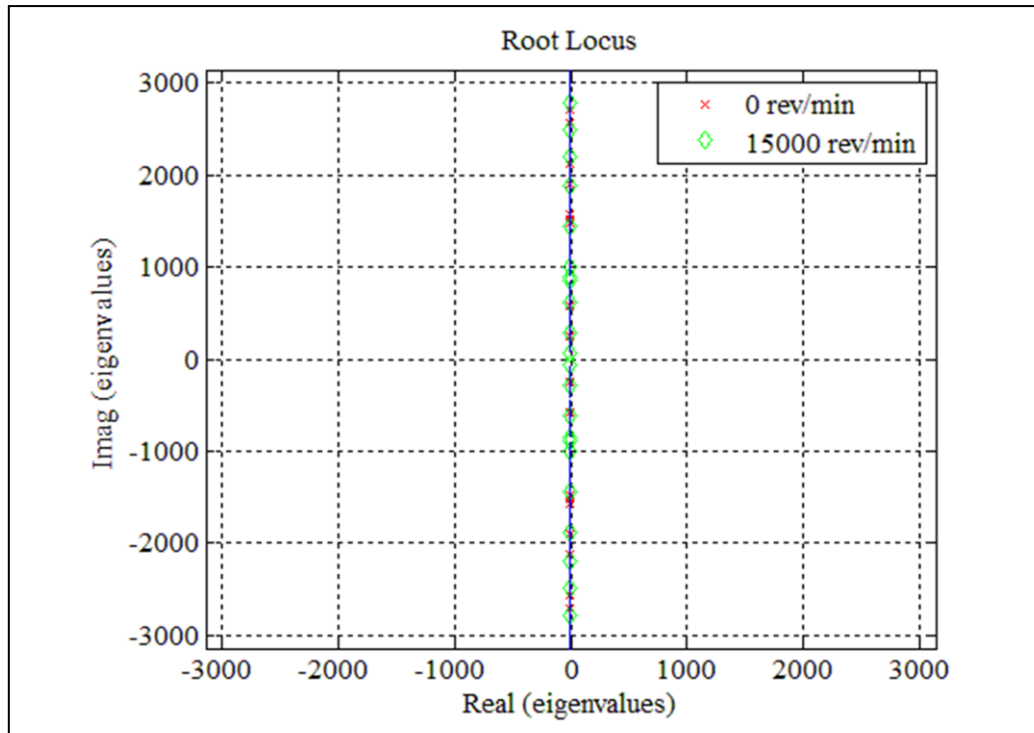


Fig.(5) Root locus diagram of the model.

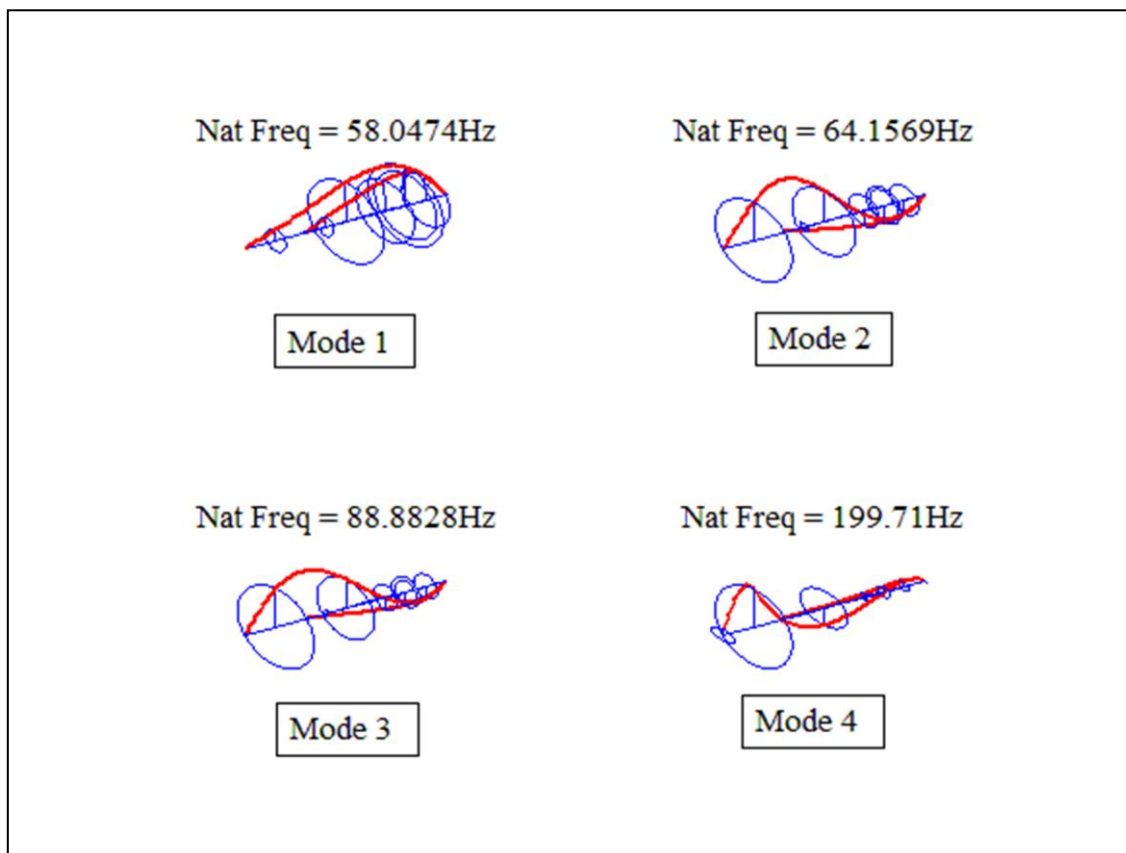


Fig.(6) The first four natural frequencies and mode shapes for the model.

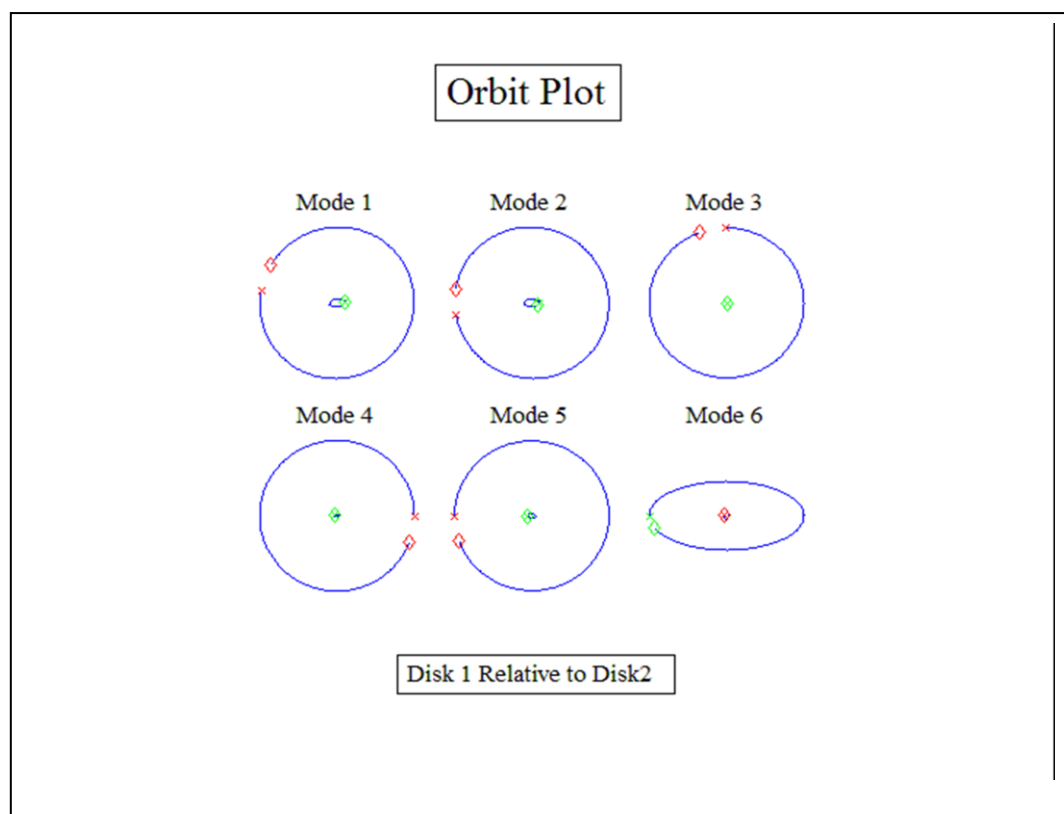


Fig.(7) Orbit plot of disk 1 relative to disk 2.

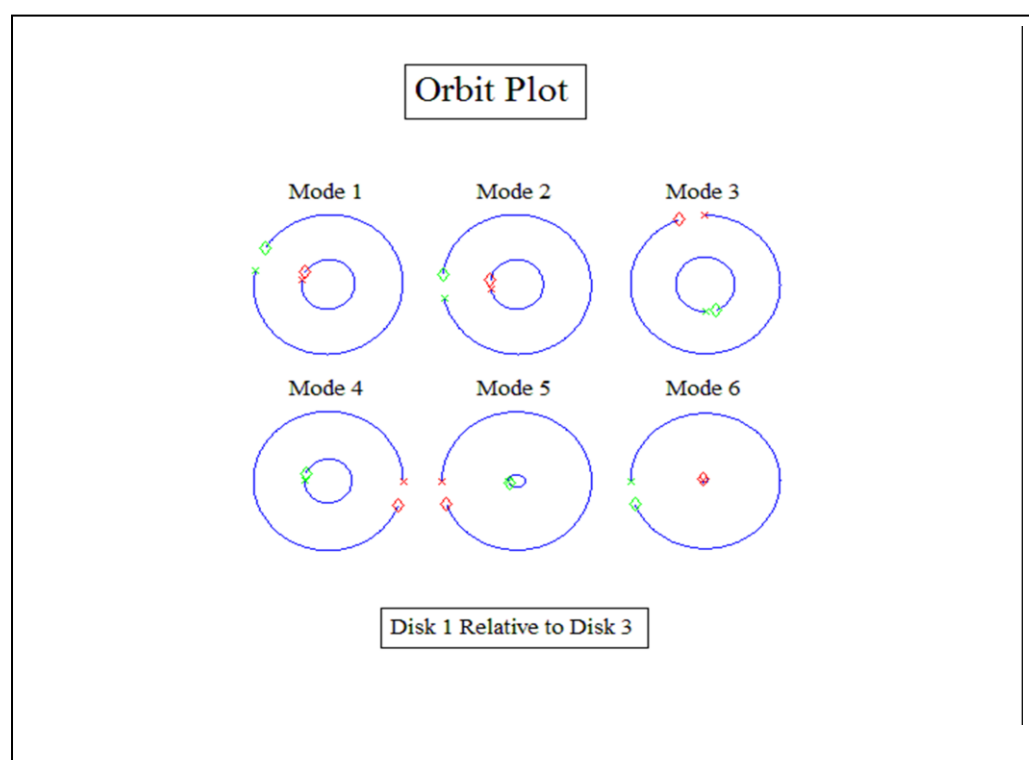


Fig.(8) Orbit plot of disk 1 relative to disk 3.

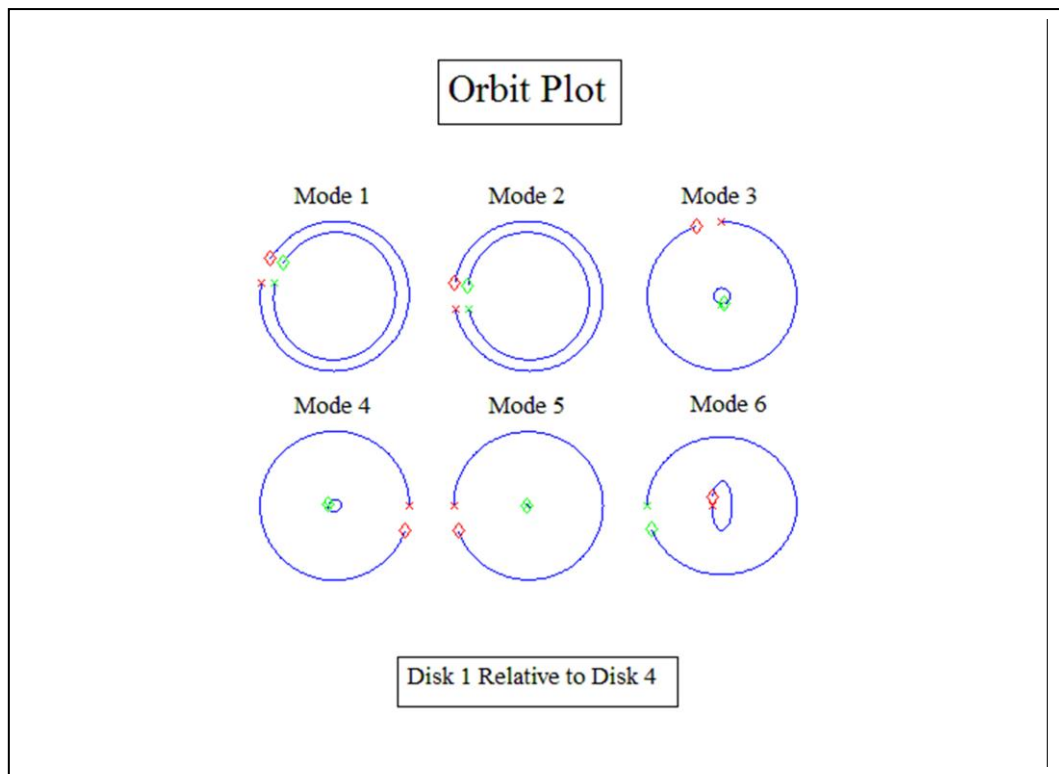


Fig.(9) Orbit plot of disk 1 relative to disk 4.

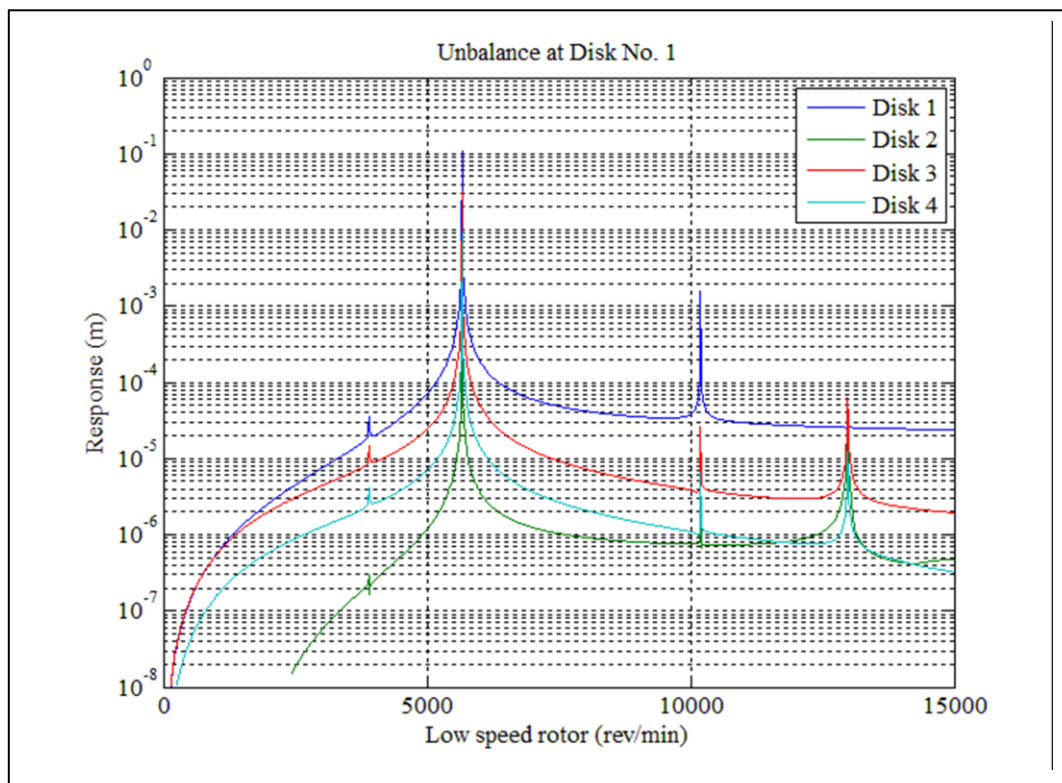


Fig.(10) Response of the model disks due to an unbalance at disk 1.

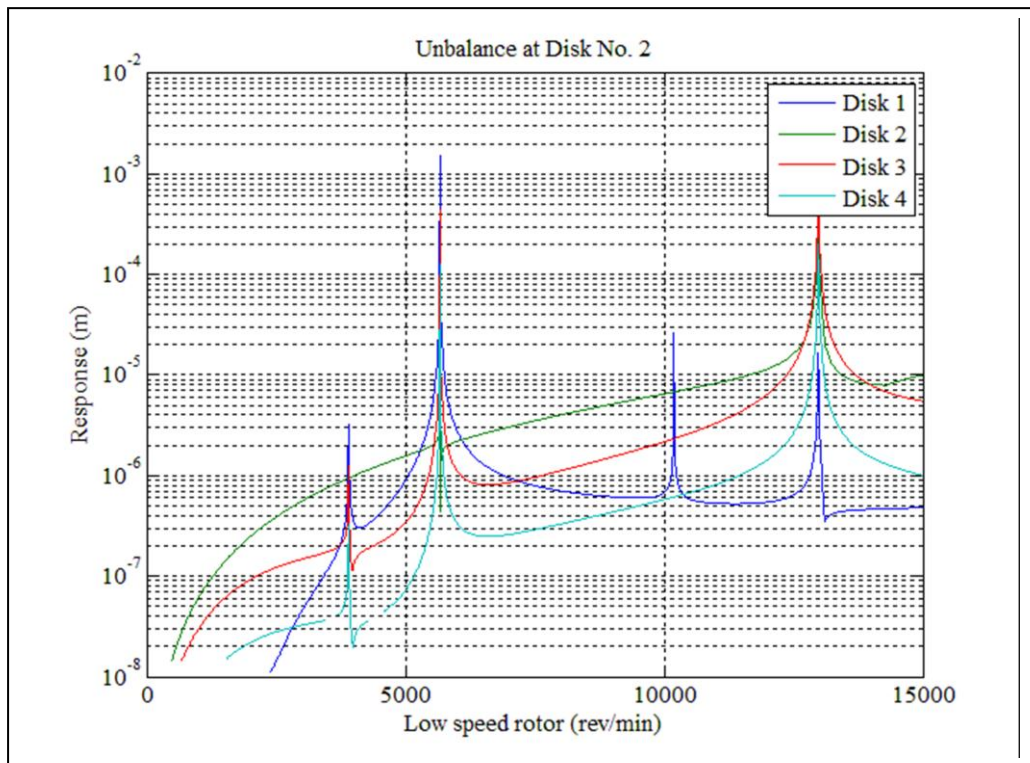


Fig.(11) Response of the model disks due to an unbalance at disk 2.

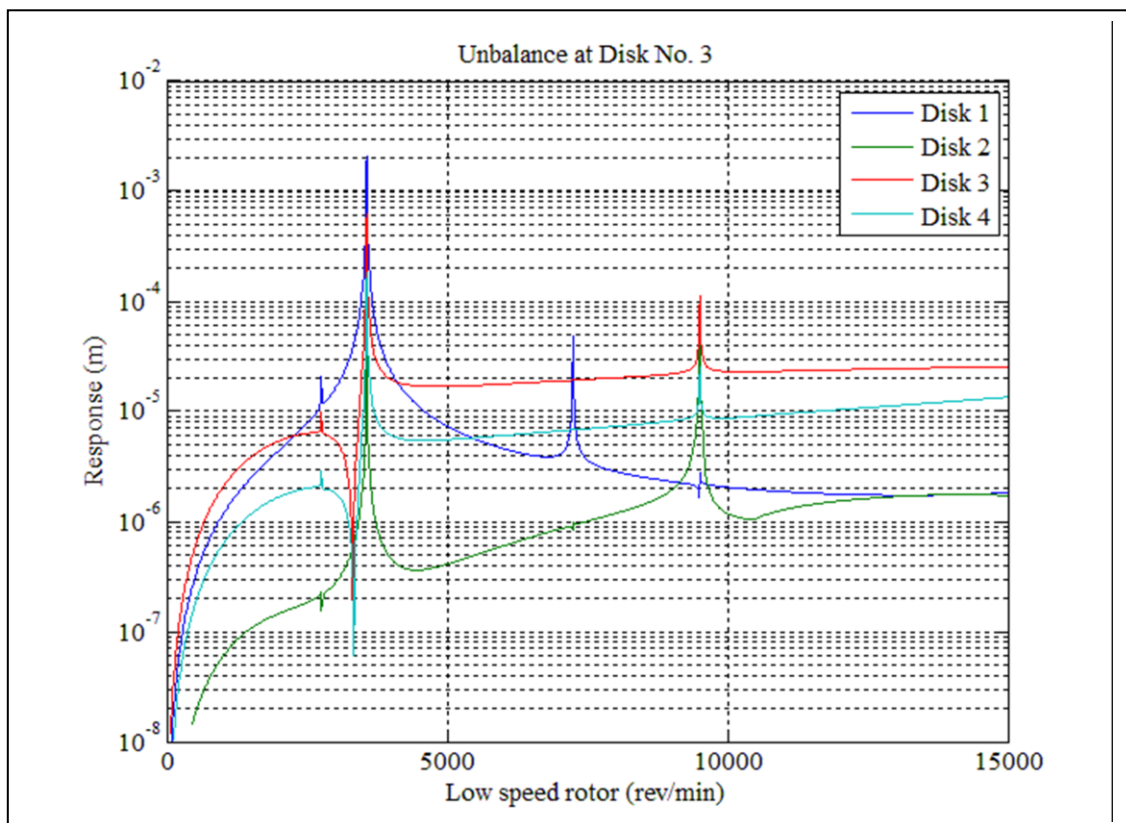


Fig.(12) Response of the model disks due to an unbalance at disk 3.

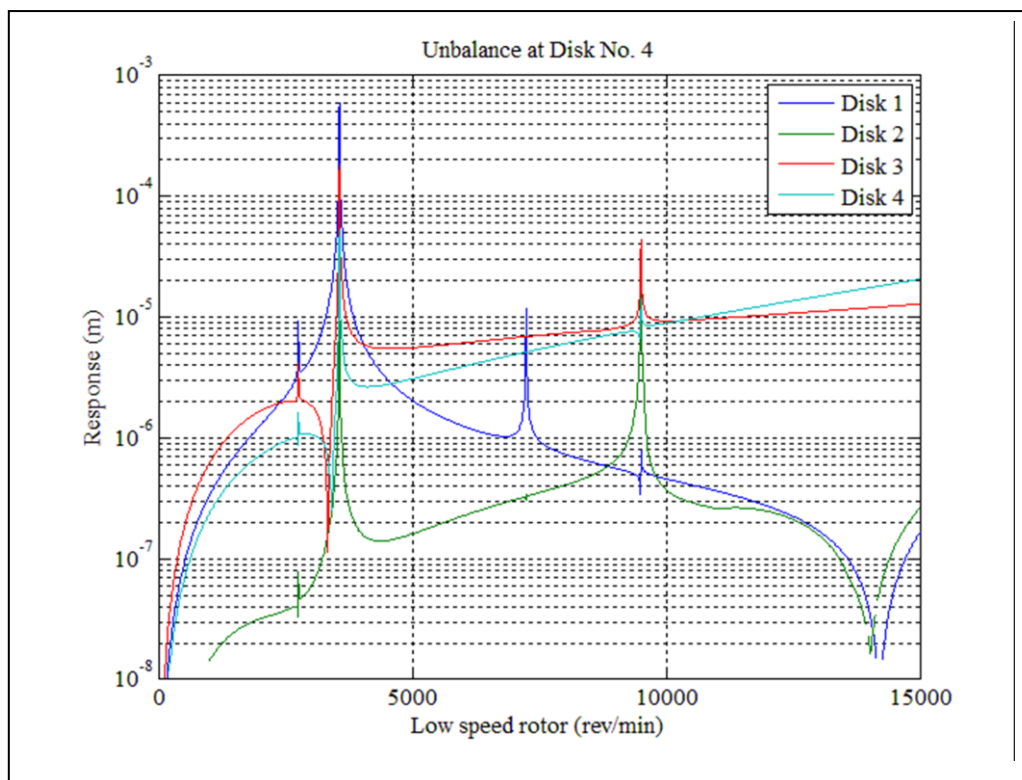


Fig.(13) Response of the model disks due to an unbalance at disk 4.

Experimental Study on Composite Beams with Circular Web Openings

Waleed Kh. Hadi

May J. Hamoodi

Civil Engineering Department

Building and Construction Department

Collage of Engineering

University of Technology

Dhi-Qar University, Nassiriya, Iraq

Baghdad, Iraq

waleedalzirgany@yahoo.com

ABSTRACT

The behavior of composite beams with circular web openings is described. Four composite beams comprising one control beam were tested. The perforated beams have six circular openings with various locations. Opening size was fixed (66.7% of the steel section web depth) while number of openings in each composite beam was varied. Deflections at midspan and at openings were observed. Cracking of concrete slab and behavior of each opening were explained in detail. Tests indicated that circular web opening reduced the strength of composite beams. The behavior of composite beams relatively unaffected by the presence of circular web openings up to first yield. Less effect for the inclusion of circular web openings located out of midspan. The concrete slab has limited contribution to the strength of composite beams with circular web openings.

KEYWORDS: Composite beams, Web openings, Circular, Moment to shear ratio, Slab behavior.

الملخص

تم شرح تصرف العتبات المركبة الحاوية على فتحات دائرية في الساق. تم فحص أربعة عتبات مركبة بضمنها عتبة مركبة واحدة مرجعية. العتبات احتوت على ستة فتحات دائرية ذات مواقع مختلفة. تم تثبيت حجم الفتحة (66.7% من عمق وتره المقطع الحديدي) بينما تم تغيير عدد الفتحات في كل نموذج عتبة مركبة. تم قياس الهطول في منتصف كل عتبة وعند الفتحات. تم العرض لشرح تفصيلي عن تشققات السقوف وتصرف كل فتحة. أظهرت الفحوصات أن الفتحة الدائرية تقلل من مقاومة العتبة المركبة. تصرف العتبات المركبة لا يتأثر تقريباً بوجود فتحات حتى حصول الخضوع الأولي للمقطع الحديدي. تأثير اقل لوجود الفتحات الدائرية خارج

موقع منتصف طول فضاء العتبة. السقف الخرساني له مشاركة محدودة في مقاومة العتبات المركبة ذات الفتحات الدائرية في ساق الوتر.

1. Introduction

Modern multistory buildings always have a stringent requirements on headroom. In order to accommodate building services within the constructional depth of a floor, it is common practice to provide web openings in structural floor beams for passing services such as air-conditioning pipeline, cables and ducts. Most openings may be rectangular or circular, and may be in the form of discrete openings, or a series of openings along the beam. Careful sizing and positioning of the openings in the beam web can minimize their adverse effects on shear and bending resistances of composite beams.

When a perforated steel beam is subjected to shear, the tee-sections above and below the web openings must carry the applied shear as well as the primary and secondary moments. The primary moment is the convectional bending moment and the secondary moment (Vierendeel moment), results from the action of shear force in the tee-sections over the horizontal length of the web opening. Therefore, the horizontal length of the web opening directly affects the secondary moment. In the absence of local or overall instability, perforated beams with standard web openings have two basic modes of collapse, which depend upon the geometry and the position of the web opening. They are as follows:

1. Plastic tension and compression stress blocks in the top and bottom tee-sections in regions of high overall buckling.
2. Parallelogram or Vierendeel action due to the formation of plastic hinges at the four corners or at specific angles around the web opening, in regions of high shear stress [1].

For composite beams, the composite action developed between the top-tee section and the concrete slab increases the resistance to Vierendeel action.

Circular web openings are structurally efficient, and also convenient for distribution of circular service ducts and water pipes [2]. The provision of multiple circular openings in the beams became a popular architectural feature of steel framed

structures [3]. For a composite beam with a circular web opening, the effective length and effective depth may be taken less than the web diameter. Therefore, the Vierendeel bending effects are less critical [2].

Considerable amount of experimental research work on composite beams with rectangular web openings were done. Clawson and Darwin [4] conducted tests on six composite beams with one or two rectangular web openings with different moment-shear ratios. Redwood and Wong [5] described the effect of large rectangular web openings on five composite beams with ribbed slab. Only one of the beams contain two web openings. Redwood and Poubouras [6] described tests of two composite beams with large rectangular web openings. Lawson et al [7] summarized the results of three load tests on composite beams of 10 m span, comprising one control composite beam, i.e. without opening and five rectangular openings of various sizes and locations. Cho and Redwood [8] describe nine tests in which composite beams containing one or two large rectangular web holes. Hamoodi and Hadi [9] conducted tests on six composite beams with rectangular and square openings. Various numbers and locations for openings were considered.

This study presents the results of an experimental investigation designed to provide information about composite beams with circular web openings. The key parameters in the current study were the number of openings and the moment to shear ratio (M/V) at the opening. The beams behavior was explained and the major observations were summarized.

2. Composite Beams Details

The study considered four composite beams of steel I-section and concrete slab which connected together by headed shear studs. One of the beams fabricated without web opening, while each of the others perforated with different number and locations of web openings; one central opening, two openings at third points, and three openings at quarter points. All openings have 100 mm diameter (66.7% of the steel section web depth) and centered at the mid-depth of the steel section. Information about beams and openings are listed in Table (1).

The steel section was IPEAA-160. Three tensile test specimens were cut out from top flange, bottom flange, and from web. The specimens were tested to get yield

strength and modulus of elasticity of 337 N/mm^2 and $196 \times 10^3 \text{ N/mm}^2$, respectively. The concrete slab thickness was 60 mm and the width was 500 mm reinforced with $\text{Ø}5@100 \text{ mm}$ steel deformed bars in both longitudinal and transverse directions at slab mid-depth. Tensile tests indicated that yield strength and modulus of elasticity of steel bars were 650 N/mm^2 and $198 \times 10^3 \text{ N/mm}^2$, respectively. Based on characteristics of partial shear connection, shear connectors with 8 mm diameter were distributed in two rows at 150 mm center to center in the longitudinal direction. Also, three specimens of the shear connectors were tested to obtain the yielding strength and modulus of elasticity which was 256 N/mm^2 and $197 \times 10^3 \text{ N/mm}^2$, respectively. The typical cross section of the composite beams is show in Figure (1).

3. Beam Fabrication and Casting

Firstly, the centers of openings in the web of steel section were determined for all beams. Then, the openings were cutout using an oxy-acetylene torch. The shear connector studs with 45 mm length were well hand welded at the top flange of steel section with uniform spacing.

Before casting, the steel framework of the concrete slab was lubricated and set level with top flange of steel section. The steel reinforcing mesh was kept at the mid-depth of slab. Concrete mix used through the whole investigation was the same. The mix proportions by weight were (1 : 1.5 : 3) of portland cement, fine aggregate, and crushed coarse aggregate, respectively. The water to cement ratio was 0.5. During casting of each beam, three (300 mm x 150 mm) diameter cylinders and three cubes of (150 mm x 150 mm) were made. All casted elements were well compacted using poker vibrator. The curing was done with same conditions. Results of cylinders and cubes at age of 28 days are listed in Table (2).

4. Instrumentation and Loading

Prior to testing, the beams were painted with white color in order to provide a better surface for crack marking. Each tested beam was simply supports and loaded with a single concentrated load at midspan using hydraulic loading system with maximum capacity of 2000 kN. Dial gauges of sensitivity 0.01 mm, were used to measure vertical deflection at midspan of the tested beam, and at the centerline of each opening, Figure (2).

At the start of each test, one cycle of 5 kN was applied to bed the beam on the supports. Load control with increments of 5 kN was used until a beam began to soften and deformed plastically. At this point deflection control was used. The dial gauges readings were recorded and cracks were marked after each load step. The test was stopped when excessive deflection happened with small load increments.

Cracks in the concrete slabs were marked and identified by load. After the beam had failed, the load system was removed, additional cracks were marked and additional photographs were taken.

5. Results

5.1 Load-deflection curves

The load-deflection curves for the composite beams during the tests are shown in Figure (3). The curves indicate approximately linear behavior up to (64 -79)% of the ultimate load followed by ductile failure. All beams have similar behavior before first yielding. When yielding began, two different behaviors can be noted. One for beams CB0 and CB2 and the other for beams CB1 and CB3. All beams had deflection about 30 mm at failure, except beam CB2 had about 20 mm.

The load-deflection relations show that the presence of circular web opening at midspan, the largest moment to shear ratio, controls the behavior of the composite beams. Beam CB2 which contains two openings each with 0.6 m M/V behaves as the imperforated beam CB0. Where beam CB3 which contains three openings one of them at midspan, behaves as beam CB1 which contains one opening at midspan. Since first yielding of steel section occurred at about 70% of ultimate load, it can be considered as a measure for the ultimate strength and the concrete slab contributes little to the ultimate strength. However, the compressive strength of concrete slab for beam CB2 was a little higher than those for other beams which results in a little more stiffness especially after first yield of steel section.

5.2 Slab behavior

In all beam specimens, transverse crack first formed at the bottom of concrete slab at midspan in the range of (73-84)% of the ultimate load. This crack was initially located adjacent to the steel flange edges and spread toward the edges of the slab. As

load was increased the crack propagated toward the top of the slab with increasing in width. About 90% of the ultimate load, another transverse cracks started at the top of slab near the low moment ends of openings CH2 and CH6 (Figure (4)). Longitudinal cracks were occurred at applied load of the range (88-96)% of the ultimate load started at the center of the top surface of the slab. These cracks were at midspan and propagated toward the side edges up to failure load.

Longitudinal cracks occurred due to splitting of concrete at the region of shear connectors which were stressed at early stages of loading. . For beams CB0 and CB1 the longitudinal crack reached about the quarter of the span from each side

5.3 Ultimate load

Ultimate loads were governed by failure of the concrete at midspan. Tests indicated that there was a decrease in ultimate strength due to the inclusion of web openings. The failure load for beam CB0 was 125 kN. The other perforated beams; CB1, CB2 and CB3 failed at 102 kN, 116 kN and 100 kN, with reduction of 18.4, 7.2 and 20%, respectively. In spite of perforating beam CB2 with two holes each one with 0.6m M/V, its failure load was higher than that for beam CB1 which perforated with one hole at midspan. The results show that beam CB3 had little reduction in ultimate failure load by introducing two openings at M/V equal 0.4 m when compared with beam CB1.

5.4 Behavior at openings

The bottom tees of openings located at midspan were first position yielded in beams CB1 and CB3. Holes CH1 and CH5 yielded at 75% and 69% of the ultimate load, respectively. Yielding extended along the width of openings that indicates a flexure failure. Near failure, the top tees yielded also and the concrete slab over openings crushed. It can be noticed that there was a local buckling at the top tee of opening CH1.

Little increase in the deflection of opening CH2 with respect to CH3 (Beam CB2) and in CH6 with respect to CH4 (beam CB3) was observed near failure load, see Figure (5). This is due to the presence of concrete transverse cracks over openings CH2 and CH6. All openings shape at failure are shown in Figure (6).

5.5 Failure mode

Failure of the composite beams was quite ductile. The reaching of ultimate loads were preceded by major cracking in the concrete, yielding of the steel section and large deflections. Yielding of steel sections at midspan (in the presence of an opening or not) was observed at load level more than 64% of the ultimate load. Yielding occurred at the tension zone or the bottom tee of steel section at opening. As the load increased, longitudinal and transverse cracking occurred within the slabs. At collapse, the concrete around shear studs at midspan failed, and the slab may be lifted (bridged) from the steel beam. Typical failure mode for composite beams (beam CB3) is shown in Figure (7).

Ultimate loads and the levels of applied load at first cracks and at initial yielding of steel section corresponding its locations are summarized in Table (3).

6. Conclusions

Based on the experimental investigations conducted in this study, the following conclusions can be drawn:

1. Circular openings within the web of steel I-section reduce the strength of composite beams, especially when the opening is at the section of highest moment.
2. The behavior of composite beams is relatively unaffected by the presence of circular web openings up to first yield. For the stages after, no significant effect for the inclusion of opening located out of midspan.
3. Composite beams with circular web openings at midspan failed by flexure. Plastic hinges formed at the top and bottom tees of the opening. The bottom plastic hinge extended up to collapse.
4. The failure mode of composite beams with circular web openings is quite ductile. Failure is beginning by yielding of steel section, followed by major cracking of concrete, and then large deflection at midspan.
5. The first yield of steel section in the presence of opening gives a measure for the ultimate strength of the composite beam.

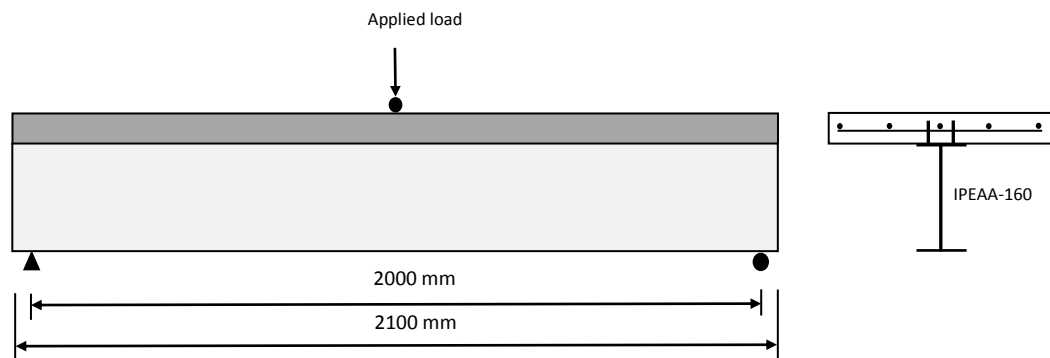
6. The concrete slab has limited contribution to the strength of composite beams with circular web openings.

References

1. Chung, K. F., Liu, T. C., and Ko, A. C., 2001, " Investigation on Vierendeel mechanism in steel beams with circular web openings", Journal of Constructional Steel Research, Vol. 57, pp. 467-490.
2. Chung, K. F., and Lawson, R. M., 2001, " Simplified design of composite beams with web openings to Eurocode 4 ", Journal of Constructional Steel Research, Vol. 57, pp. 135-163.
3. Psarras, L. D., Lagaros, N. D., Panadrakakis, M., 2005, "Sizing and shape optimization of 3D steel structures with web openings", 5th GRACM International Congress on Computational Mechanics, Limasol,.
4. Clawson, R. M., and Darwin, D., 1982 " Tests of composite beams with web opening ", Journal of the Structural Division, ASCE, Vol. 108, No. 1, pp 145-162,.
5. Redwood, R. G., and Wong, P. K., 1982 " Web holes in composite beams with steel deck ", Proceedings of the 8th Canadian Structural Engineering Conference, Canadian Steel Construction Council, Willow dale, Ontario, Canada,.
6. Redwood, R. G., and Poubouras, G., 1983, " Tests of composite beams with web holes ", Canadian Journal of Civil Engineering., Vol. 10, No. 4, pp 713-721, December.
7. Lawson, R. M., Chung, K. F., and Price, A. M., 1992, " Tests on composite beams with large web openings to justify existing design method ", Journal of The Structural Engineer, V 70, No.1, January.
8. Cho, S. H., and Redwood, R. G., 1992, " Slab behavior in composite beams at openings II: Tests and verification ", Journal of Structural Engineering, ASCE, Vol. 118, No. 9, pp. 2304-2322, September.
9. Hamoodi, M. J., and Hadi, W. Kh., 2011, " Tests of composite beams with web openings", Engineering and Technology Journal, Vol. 29, No. 10.

Table (1): Geometric Properties of Openings

Composite Beam	Opening	M / V at opening (m)	No. of Studs through Opening
CB0	-	-	-
CB1	CH1	1.0	2
CB2	CH2	0.6	2
	CH3	0.6	2
CB3	CH4	0.4	2
	CH5	1.0	2
	CH6	0.4	2

**Figure (1): Composite beams details****Table (2): Concrete Properties**

Beam	Average Compressive strength at 28 day (N/mm ²)		Unit weight (kN/m ³)
	Cylinder	Cube	
CB0	27.3	29.2	23.04
CB1	22.6	27.5	22.82
CB2	27.9	33.4	23.21
CB3	22.7	26.6	22.73

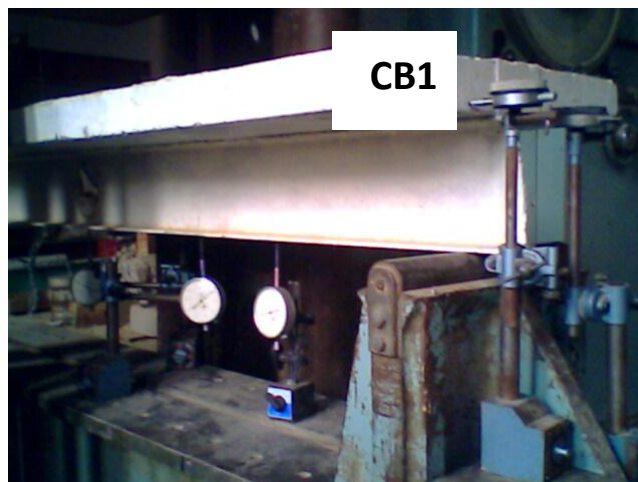


Figure (2): Beam setting

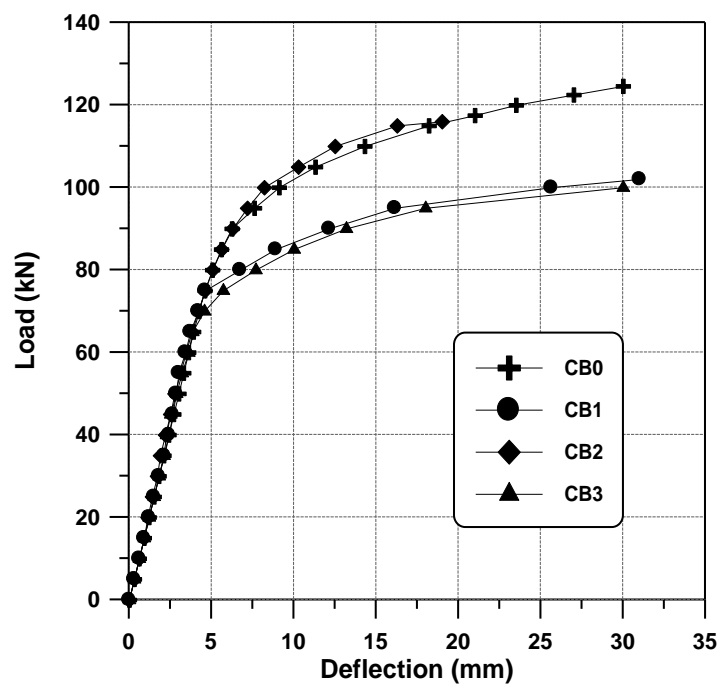


Figure (3): Load-deflection curves

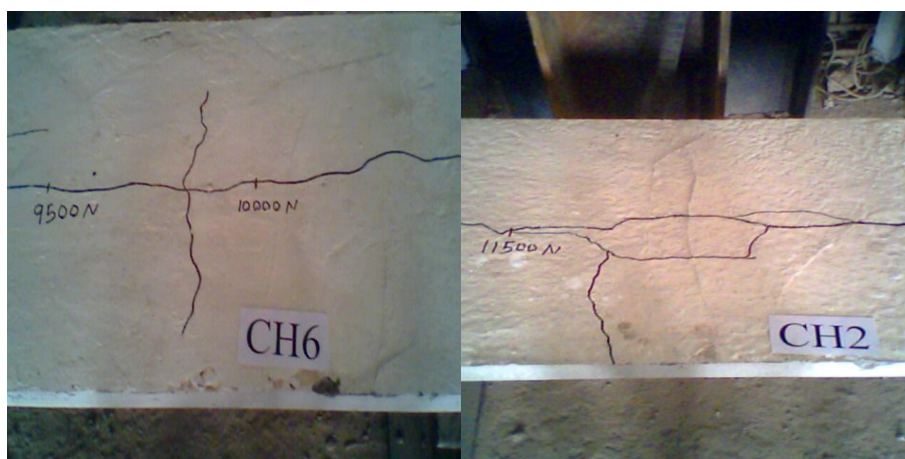


Figure (4): Concrete Cracking over openings



Figure (5): Openings at failure

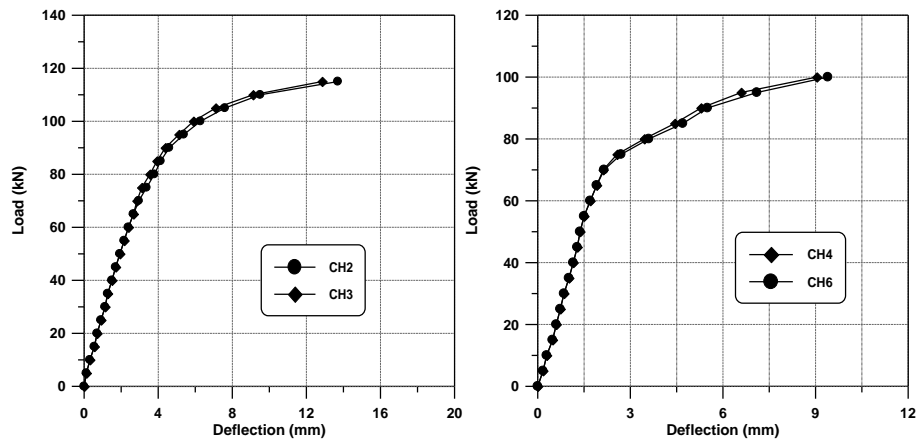


Figure (6): Deflection at Openings



Figure (7): Typical failure mode (Beam CB3)

Table (3): Test results

Composite Beam	Ultimate Load (kN)	Appearance of First Crack (% of ultimate load)		Initial Yielding of Steel Section (% of ultimate load)	
		Transverse	Longitudinal	Load (kN)	Location
CB0	125	84	96	64	bottom flange
CB1	102	78	88	75	bottom tee
CB2	116	73	95	79	bottom flange
CB3	100	80	91	69	bottom tee

The Influence of Injection pressure on Combustion and Emission Characteristics of a common-rail HSDI Diesel Engine

Hayder A.Dhahad¹ , Mohammed A. Abdulhadi ¹, Ekhlās

M.Alfayydh¹, T. Megaritis²

¹ University of technology – Baghdad –Iraq

² Brunel University, UK

Abstract

The present work investigates the influence of fuel injection pressure on the combustion and emission characteristics of ultra-low diesel fuel for high speed direct injection (HSDI) diesel engine at different fuel injection timings (-12,-9,-6,-3,0)ATDC has been made . The fuel injection pressure were (800,1000,1200) bar and at high load (80Nm= 5BMAP) , low load (40Nm=2.5BMAP) , With constant engine speed (1500rpm) . In-cylinder pressure was measured and analyzed using LABVIEW program .A calculation program specially written in MATLAB software was used to extract the apparent heat release rate, the ignition delay, combustion duration and specifies the amount of heat released during the premixed and diffusion combustion phases (premixed burn fraction PMBF) and (diffusion burn fraction DBF). The influence of injection pressure on the exhaust emissions such as carbon monoxide (CO), total hydrocarbons (THCs), nitric oxides (NO_x), smoke number (SN) and fuel consumption were also investigated.

A result referring to that when the injection pressure was increased, the ignition delay reduced. A shorter ignition delay at high injection pressure also advanced the combustion, and increased the in-cylinder pressure, heat release rate and their peaks respectively .The premixed burn fraction increased with fuel injection pressure increasing, and this caused a decrease in each of the exhaust SN, THC and CO emissions but the NO_x emissions increased.

Key words: combustion, diesel engine, injection pressure, gases emissions.

المخلص

هذا البحث درس تأثير ضغط الحقن على خصائص الاحتراق والانبعاثات لوقود الديزل منخفض الكبريت باستخدام محرك ديزل عالي السرعة وذو حقن مباشر ومع تغيير توقيت الحقن عند (-12,-9,-6,-3,0) , (ATDC) (ضغط الحقن للوقود كان (0881,8881,088 (ضغط جوي واجريت التجارب عند الحمل العالي (80Nm= 5BMAPوالحمل المنخفض , (40Nm=2.5BMAP) تم تثبيت سرعة المحرك عند 088

. rpm تم قياس الضغط داخل غرفة الاحتراق ومن ثم تحليل الضغط باستخدام برنامج LABVIEW وبرنامج حسابي باستخدام برنامج MATLAB لحساب معدل الحرارة المنطلقة و تاخر الاشتعال و مدة الاحتراق وكمية الحرارة المنطلقة في طور الاحتراق المسبق الخلط وكذلك في طور الاحتراق الانتشاري. تأثير ضغط الحقن على انبعاثات غازات العادم مثل اول اوكسيد الكربون (CO) الهيدروكربون غير المحترق الكلي (THC) واكاسيد النيتروجين (NOx) ورقم الدخان (SN) ومعدل استهلاك . النتائج اشارة الى ان زيادة ضغط الحقن نتج عنه نقصان في تاخر الاشتعال وبالتالي تقدم في بداية الاحتراق وزيادة ضغط الاسطوانة ومعدل الحرارة المنطلقة، ان زيادة جزء الاحتراق المسبق الخلط عند زيادة ضغط الحقن سبب نقصان في انبعاثات العادم لكل من SN و THC و CO ولكن انبعاث NOx يزداد.

2

NOMENCLATURE

AHRR Apparent heat release rate
 ATDC After top dead centre
 BMAP Brake mean effective pressure
 CI Compression ignition
 CO Carbon monoxide
 CO₂ Carbon dioxide
 C_p Specific heat at constant pressure
 C_v Specific heat at constant volume
 DBF Diffusion burn fraction
 EGR Exhaust Gas Recirculation
 EOC End of combustion
 EOPMB End of premixed burn
 HCCI Homogenous Charge Compression Ignition
 HSDI High speed direct injection
 ID Ignition delay
 LTC Low Temperature Combustion
 NO Nitrogen monoxide
 NO₂ Nitrogen dioxide
 NO_x Nitric oxides
 PCCI Premixed Charge Compression
 PM Particulate matter
 PMBF Premixed burn fraction
 SOC Start of combustion
 SOI Start of injection

Sox Sulfur oxides

SN Smoke number

THCs Total hydrocarbons

ULSD Ultra-low sulfur diesel fuel

1. Introduction

Although the advantages of high thermal efficiency and high performance of the compression ignition (CI) engine, the unburned or partially burned (total) hydrocarbon (THC) emissions, smoke (soot) or particulate matter (PM), nitrogen oxides (NO_x), sulfur oxides (SO_x) emitted from compression ignition (CI) engines and particularly carbon dioxide (CO₂) create severe environmental problems (Shah et al 2009, Abdel-Rahman 1998, Lebedevas and Vaicekauskas 2006). The past two decades have witnessed drastic reductions in regulated limits for pollutant emissions from diesel engines. For example, heavy-duty engine emissions limits in the United States (EPA 2003), the European Union (EEC1998, EEC1999, EPC 2009), and Japan (DieselNet 2009) for particulate matter (PM), nitrogen oxides (NO_x) and unburned hydrocarbons (THC) in the early 2010s are only 2%, 3*10⁻¹²%, and 6*10⁻¹²%, respectively, of their 1990 levels. Comparable reductions were also required in the light duty sector (DieselNet 2009, EPA2010). Likewise, in China and India, the evolution of emissions regulations for both

3

heavy- and light-duty diesel engines from 2000 through 2010 required reductions of similar magnitudes, mirroring the Euro I through Euro IV regulatory limits, though at an accelerated pace (DieselNet 2009).

Soot formation has been extensively investigated with regard to combustion characteristics (Suzuk et al 1997 Part 1, Suzuk et al 1997 Part 2, Senda et al 1999, Kawano et al 2001, Adomeit et al 2006) and application of alternative fuels (Miyamoto et al 1998, Kitamura et al 2001, Xu and Lee 2006). The model of soot formation in diesel spray has been proposed by Dec (Dec 1997) and it is illustrated in Figure (1)

Figure (1) Conceptual model of the soot formation process in diesel spray, proposed by (Dec 1997)

This model predicts that primary soot particles initially form at the leading edge of the liquid fuel jet where rich premixed combustion takes place due to initial fuel mixing process. However, as the vapor jet progresses across the cylinder, secondary soot particles, accountable for the majority of soot emissions produced by diesel engines,

form downstream of the jet particularly around the jet periphery whereby mixing controlled diffusion combustion occurs. Other major pollutants formed during diesel combustion are nitrogen oxides, commonly referred to as NO_x. The oxides of nitrogen present in the diesel exhaust gas consist of approximately 70-90% Nitrogen Monoxide (NO) and 10-30% Nitrogen Dioxide (NO₂) (Majewski and Khair 2006) . nearly all NO_x emission is formed between the start of combustion and the first 20° of crank angle. Therefore most NO_x reducing techniques are focused on this critical period (Challen and Baranescu 1999) . one of the major difficulties in conventional diesel engines is the NO_x-soot trade off. Premixed combustion, during which in-cylinder pressure and temperature are very high, plays an important role in NO formation (Peirce et al 2013). Techniques to control NO_x formation are mainly linked to a reduction in combustion temperature during this phase of combustion. Unfortunately, a reduction in combustion temperature also leads to an increase in PM emissions. new and renewable fuels are being used for a possible

4

effective replacement of the conventional diesel fuel either partially or completely (Labecki and Ganippa2012) .Furthermore ,diverse combustion and injection strategies (Low Temperature Combustion LTC, Homogenous Charge Compression Ignition HCCI, Premixed Charge Compression PCCI) have been studied among many research groups to reduce the exhaust emission and simultaneously increase the thermal efficiency of engine (Rakesh et al2013, Kokjohn and Reitz2010, Li et al 2010, Zhen Huang et al2013).The introduction of the common rail fuel injection system in the 1990s allowed greater control over the fuel injection rate and timing over the entire operating range of diesel engines. The fuel injection pressure is independent of the engine speed; thus, capable of promoting improved fuel evaporation and mixture formation at low speeds and loads. Such control over fuel injection system resulted in the development of alternative injection strategies through the application of split or multiple injections aimed at reduction of exhaust emissions while maintaining good level of fuel economy and combustion efficiency. Recent studies on NO_x and soot formation involved detailed analysis of the effect of alternative fuels (Kwanhee et al 2013, Sara Pinzi et al 2013, Karavalakis et al2010, Kawano et al2010, Kim et al2013, Ushakov et al 2013, Bermudez et al 2011, Kegl 2011), fuel injection timing (Seung et al 2011, Mani and Nagarajan 2009), injection strategy (Díez et al2012, Herfatmanesh and Hua Zhao2013) , and Exhaust Gas

Recirculation (EGR) (Desantes et al 2013, Bermúdez et al2011, Sarangi et al2010) , fuel injection pressure (Rakopoulos2012, Manasra and Brueggemann2011, Sayin and Gumus 2011, Puhan et al 2009). Modifications of engine operating parameters through the application of the aforementioned techniques resulted in significant reduction in soot emission. The present work investigates the effect of fuel injection pressure to understand the combustion and emission characteristics of ultra-low sulfur diesel fuel (ULSD) in a high speed direct injection diesel engine HSDI and that use of the modern fuel injection system type common rail injection system.

2- METHODOLOGY

2-1- Experimental setup and test conditions

Experiments were carried out in a 2 liter, 4 cylinders, 16 valves, compression ratio18.2, direct Injection Ford diesel engine, coupled to a Schenck eddy current dynamometer. The schematic of the experimental setup is shown in figure (2).

5

Figure 2. The schematic of experimental setup

In this investigation the engine was operated under naturally aspirated mode. The engine is fully instrumented, which enables the measurement of in-cylinder pressure and exhaust gas emissions under steady-state engine operating conditions. The in-cylinder pressures were measured using a Kistler pressure transducer fitted into the first cylinder of the engine. The signal from pressure transducer was amplified by the charge amplifier and then recorded by the LabView software in conjunction with the shaft encoder. In-cylinder pressure data were collected over 100 engine cycles per measurement, and the measurement was repeated 5 times for each point in the experimental matrix .The in-cylinder pressure data was averaged from100 cycles Output from the LabVIEW program are showed in figure (3) .

A common rail fuel injection system with six holes injector of 0.154 mm in diameter each, and a spray-hole angle of 154 degree was used in this investigation. In this study, the influence of injection timing has been tested. The Gredi software allowed the control and change of these parameters by programming the ECU in real time. Injection timing could be directly controlled through the software. The gaseous exhaust emissions were acquired using a Horiba-Mexa 7170DEGR gas analyser. A non-dispersive infrared method has been used for measuring the CO and CO₂ emissions. The NO_x emissions have been measured using chemiluminescence technique whereas the total unburnt hydrocarbons (THC) were measured using the

flame ionization detection technique, figure (4) shows a sample of these measurements.

6

Figure (3) LabVIEW program screen

Figure (4) Horiba measurement screen

Emissions data were recorded over 180 seconds intervals, twice for each point in the experimental matrix. Again, this process was repeated for confirmatory purposes.

The engine exhaust smoke emissions were measured using the AVL – 415 smoke meter while the diesel fuel consumption was measured using an AVL fuel consumption meter, which is based on gravimetric measurement principle .

7

Measurements were carried out using the standard ultra-low sulfur diesel fuel. [Table \(1\)](#) provides an overview of all tested engine operating conditions .The load and speed conditions have been chosen to represent the commonly used operating condition for the stationary driving cycle for automotive diesel engines.

After start-up, the engine was allowed to warm up until hydrocarbon emissions (the slowest pollutant to stabilize) had settled to an apparent steady state; this typically took around 90 min under an 80 Nm load. At each operational condition data collection was postponed until all emissions had reached apparent consistency when viewed over a 180 seconds duration.

2-2 Data Analysis

Raw data collected using LabView was loaded into MATLAB and batch processed to retrieve the pertinent information. In-cylinder pressure was processed to extract relevant data-peak pressure, angle of peak pressure, angle between start of combustion (SOC) and peak pressure- and to calculate apparent heat release rate (AHRR) data using the traditional first law heat release model (Heywood 1988) without any modeling of heat transfer or crevice effects, and using an assumed constant specific heat ratio of 1.35. This is a very basic approach, but it is held to be sufficient for the purposes of comparison.

Approximations of c_p/c_v were made from the logarithm of pressure versus logarithm of volume charts in order to ensure that a constant value would represent fuel equally well. The calculated ratios of specific heats were found to be essentially consistent for

ULSD under varying conditions, and so an assumed value of 1.35 was found to be adequate.

The definitions on which calculations of AHRR related parameters were based are illustrated in Figure (5) and explained in the accompanying text. Each 100 cycle pressure data set was used to generate a single average pressure trace, in order to reduce noise while maintaining the essential characteristics of combustion. It should also be noted that

8

although pressure data was only logged by the data acquisition system once per crank angle degree, all values were interpolated to one decimal place by the MATLAB code. All heat release parameters were calculated from the AHRR curve without filtering or averaging, except for the end of combustion, which was defined on the basis of the moving average of AHRR in order to improve consistency, and the end of premixed burn, which was calculated from the second derivative of AHRR. The following is a definition of the combustion characteristics in the figure (5).

1. Start of injection (SOI) was defined from the commanded SOI set within the engine management software. Any potential difference between commanded and actual SOI, due to solenoid delay for instance, should be consistent between measurements, since engine speed was held constant.
2. Ignition delay (ID) was defined as the difference between commanded SOI and calculated SOC.
3. Start of combustion (SOC) was defined as the point at which the AHRR curve crossed the x axis; that is, the heat release rate became positive.
4. Premixed burn fraction (PMBF) was defined as the integral of the AHRR curve between SOC and EOPMB, divided by the integral of the AHRR curve between SOC and EOC.
5. End of premixed burn (EOPMB) was defined as the first point at which the second differential of heat release rate reached a local maximum following the global minimum. Under most conditions, this approximately corresponds to the position at which the AHRR reaches a first local minimum following the global maximum, but the second differential was used instead because under low loads there local minimum in the AHRR curve is not always clear, as can be seen in Figure 5.
6. End of combustion (EOC) was defined as the first point at which the moving average of heat release rate dropped below zero. A moving average was used to

minimize problems due to noise, while still being representative of the general tendencies of the data.

Other values calculated from the in-cylinder pressure data including total apparent heat release, peak AHRR, PMBF, 10–90% burn fraction intervals, duration of partial burn fraction intervals, and average burn rates through partial intervals. Emissions data were averaged over the 180 s durations recorded.

Fig.(5) Labeled plot of heat release and the derivatives used to calculate combustion criteria

9

3-Results and discussions

3-1 Combustion characteristics

Figure (6) shows the variations of the in-cylinder pressure with crank angle at high load (80 N.m= 5 bar BMEP) with variation of fuel injection pressure at injection timing (-9 ATDC) , it can be seen that as the fuel injection pressure increases from 800 bar to 1200 bar the combustion starts earlier. In addition to this, the in-cylinder pressure peak increases with higher fuel injection pressure. we also note the shift in the location of pressure peaks. The rise in the momentum of the fuel spray leads to better entrainment of air into the core of the fuel spray. In addition to this, high injection pressure provides more energy to break up higher viscous fuels into smaller droplets, leading to faster evaporation at the periphery of the fuel sprays and faster ignition of the fuel vapour.

Figure (6) In-cylinder pressure under 80Nm
(5 bar BMEP) at different injection pressure

The same events occurs at the low load (40 N.m= 2.5 bar BMEP) figure (7).

10

Figure (7) In-cylinder pressure under 40Nm
(2.5 bar BMEP) at different injection pressure

In Figure (8) it can be seen that for any injection timing, the higher injection pressure causes a rise of the in-cylinder pressure peak. We also note clearly the decreasing of pressure peaks values when injection timing approaching to TDC and the obvious difference of pressure peaks values at high and low loads. The late injection of fuel in the compression stroke or even at TDC leads to a lower pressure peak due to the occurrence of combustion in the expansion stroke.

Figure (8) In-cylinder pressure peak at
different injection pressure and timing

11

As a result of increasing the In-cylinder pressure peak with the injection pressure increases, the rate of heat released will increase as shown in figure (9) and figure (10) for high and low loads respectively . In addition, the heat released peak moving forward because earlier starts of combustion.

Figure (9) apparent heat release rate under high load
at different injection pressure

Figure (10) apparent heat release rate under low load
at different injection pressure

12

Figure (11) shows the difference between heat released rate peak at high and low load at different fuel injection pressure. It is observed that AHRR peak for high load is higher than that for low load in all injection timings .This may be because operation temperatures are higher at high load. Vaporization of fuel will occur more readily than at lower temperatures, reducing the physical component of ID time. Therefore, it is probable that the observed reduction in ID at higher load is related to the impact of temperature change upon the physiochemical properties of fuel (its higher viscosity, density, heat capacity, and surface tension, reduced vapor pressure, etc.), which make the fuel generally more resistant to vaporization as shown in figure (12).

Figure (11) Heat release rate peak under high and low loads at different injection pressure and timing

It can be seen that the ignition delay decreases with an increase in the injection pressure. On average, a reduction of about 1 CAD was observed between 800 bar and 1200 bar for both loads and all injection timings. Higher injection pressure causes better mixing which reduces ignition delay.

Figure (12) Ignition delay under high and low load
at different injection pressure and timing

13

Besides, it can be noted that the ignition delay at low load was taller than at high load for each injection pressure, because of the relationship between the ignition delay and temperature, as explained above. At late injection (0ATDC) ignition delay again increasing, which leads to an increase premixed burn fraction with a high temperature at high load, the heat released rate peak increase as shown in Figure (11).

Figure (13) effect of injection pressure and timing on

duration of combustion

Figure (14) effect of injection pressure and timing on duration of premixed and diffusion combustion

A figure (13, 14) shows the duration of combustion during the premixed and the diffusion combustion phases for different fuel injection pressures. The overall DOC is the sum of premixed and diffusion combustion durations. Within this sum, the change in the

14

premixed DOC remained almost short, therefore the overall DOC inherits the trend of diffusion combustion duration for all cases. It is noticeable that duration of combustion for high load longer than duration of combustion for low load. In order to understand this, Figure (13) provides information about the duration of combustion in the premixed phase as well as in the diffusion phase. The premixed and diffusion combustion duration are distinguished using the second differential of the heat release rate. There is a significant difference between diffusion combustion duration at high load and diffusion combustion duration at low load, while there are no noticeable differences between the premixed combustion duration at high load and premixed combustion duration at low load. Interestingly, there is no diffusion combustion at conditions of low load, injection timing (-12 ATDC) and injection pressures (1000, 1200) bar, This means that the use of high injection pressure at low load with an appropriate injection timing could eliminate the soot. The combustion mode has changed from the Conventional diesel combustion to Homogenous Charge Compression Ignition HCCI by the use of high pressure injection, It is clearly noticeable in fig.(15), Where the diffusion burn fraction was equal to zero

Fig (15) effect of injection pressure and timing on premixed and diffusion burn fraction

In Figure (15) it can be seen that the amount of heat released (burn fraction) during the premixed phase is higher, compared to that of diffusion phase for all injection timings.

Generally, the amount of heat released in the premixed combustion phase is strongly connected to the formation of NO_x through the correlation of increased in-cylinder combustion temperature. A shorter duration of combustion and lower magnitude of heat released in the premixed phase leads to lower NO_x formation. On the other hand, better atomization due to higher injection pressure produces better entrainment, more efficient fuel vaporization and mixture formation. This leads to faster combustion and a higher heat release rate in the premixed phase resulting in a favourable environment

of higher in-cylinder temperature and higher NO_x emissions. The diffusion phase of combustion is strongly correlated to the soot emission from the engine, thus longer duration of diffusion combustion eventually leads to higher soot formation.

The Brake Specific Fuel Consumption (BSFC) for different injection pressure and different injection timings are shown in figure (16) . The increase in BSFC at low load is a result of the incomplete combustion of fuel . Therefore, the engine running at low

15

load is considered uneconomic, Effect of injection timing on fuel consumption was limited.

Figure (16) Effect of injection pressure and timing on The Brake Specific Fuel Consumption (BSFC) under high and low load

Increasing the injection pressure has no obvious effect on B.S.F.C at high load , while increasing the injection pressure at low load lead to reduce B.S.F.C .

3-2 Emission characteristics

Figure (17) shows the effect of fuel injection pressure at high and low loads with different fuel injection timings, it can be seen that an increase in the fuel injection pressure leads to higher NO_x emission. Where the premixed burn fraction increase with injection pressure increasing , which leads to increased heat released and therefore increase the temperature of combustion chamber . The NO_x formation during combustion mainly depends on the Zeldowich mechanism where formation reactions are more intensive in a high temperature environment leading to higher NO_x emissions. The highest cylinder temperature occurs during the premixed combustion phase where the formation of NO_x is dominant. In addition, the retarded injection timing significantly reduces the NO_x emissions because of the low in-cylinder temperature resulting from the shift of the combustion into the expansion stroke. As the difference of No_x emissions between high and low-load due to the difference of temperature in combustion chamber.

16

Figure (17) Effect of injection pressure and timing on NO_x emissions under high and low load

Figure (18) Effect of injection pressure and timing on carbon monoxide emissions under high and low load

17

Figure (19) Effect of injection pressure and timing on (THC)

emissions under high and low load

Figures (18) and (19) show the variation of CO and THC emissions at different fuel injection pressures. In figure (18) it can be seen that when fuel injection pressure increases the CO emission decreases. Figure (19) Shows the variation of the THC emissions at different fuel injection pressures. The THC emissions decrease with higher fuel injection pressure. However, the general emission trends for both THC and CO are similar. Both CO and THC emissions are the products of incomplete combustion and they tend to decrease with higher injection pressures. The unburnt hydrocarbon emissions are generally formed as a result of flame quenching. The formation of higher CO and THC emissions are strongly related to the viscosity of fuel. Higher viscosity also leads to longer spray penetration. As a result, wetting of the cylinder walls eventually leads to the formation of higher CO and THC emissions by incomplete combustion.

Figure (20) shows the variations in soot emissions under high and low loads at different injection pressures. The smoke number at all conditions is lowered by increasing the fuel injection pressure. Higher injection pressure leads to the formation of smaller fuel droplets and faster fuel vaporisation due to better entrainment which eventually results in the reduction of smoke emissions. We can clearly note the huge difference in soot emissions between high load and low-load for all timings, This difference results from the large difference in the amount of diffusion combustion (diffusion burn fraction) between high and low-load, as shown in Figure (15). The heat release rate analyses are helpful in understanding NO_x and soot emissions variations for different conditions. On the other hand, longer duration of the diffusion combustion phase leads to higher soot emissions. Furthermore, retarding the injection timing produces more heat in the premixed phase as shown in figure (15) , thus it can be suggested that soot emissions could be lower at late fuel injection timing as shown in figure (20). Late injection led to dramatic change in the mode of combustion as compared with conventional diesel combustion, where late injection lead to semi low temperature combustion (LTC) at high

18

load and to completely low temperature combustion (LTC) at low load where both soot and NO_x emissions tend to reduced simultaneously.

Figure (20) Effect of injection pressure and timing on smoke number under high and low load

Of the most important observations is the lack of a clear emission of soot under low load at fuel injection pressure (1000,1200) bar , Due to the fact that the combustion modes at this conditions are (HCC) at (injection pressure 1200bar & injection timing -12ATDC) where the combustion was just premixed combustion as shown in figure (15) , and (PCCI) & (LTC) at anther conditions .

4- Conclusions

- 1- When the injection pressure was increased, the ignition delay reduced. A shorter ignition delay at high injection pressure also advanced the combustion, and increased the in-cylinder pressure, heat release rate and their peaks respectively.
- 2- The premixed burn fraction increased with fuel injection pressure increasing, this caused a decrease in each of the exhaust SN, THC and CO emissions but the NO_x emissions increased.
- 3- At low load with high injection pressure, the combustion mode was changed from conventional diesel combustion to Homogenous Charge Compression Ignition HCCI at advanced injection timing and to (Premixed Charge Compression PCCI) & (Low Temperature Combustion LTC) at late injection timings.
- 4- The diffusion burn fraction at high load is higher than that at low load, which, leads to significant increase of soot emissions compared to those at low load.
- 5- The retardation of the injection timing leads to increase the ignition delay and therefore the premixed burn fraction is larger at late injection conditions, and this explains the characteristics of combustion and emissions at late injection.

19

Acknowledgment

The experimental work of this research has been in Centre for Advanced Powertrain and Fuels Research (CAPF), School of Engineering and Design, Brunel University, London , UK

References

- 1- A.N. Shah, G. Yun-shan, T. Jian-wei, Carbonyls emission comparison of a turbocharged diesel engine fuelled with diesel, biodiesel, and biodiesel-diesel blend, Jordan Journal of Mechanical and Industrial Engineering 3 (2) (2009) 111-118.

- 2- A.A. Abdel-Rahman, On the emissions from internal-combustion engines: a review, *International Journal of Energy Research* 22 (1998) 483-513.
- 3- S. Lebedevas, A. Vaicekauskas, Research into the application of biodiesel in the transport sector of Lithuania, *Transport* 21 (2) (2006) 80-87.
- 4- United States Environmental Protection Agency. Fact sheet: diesel exhaust in the United States; 2003. EPA420-F-03-022.
- 5- Council of the European Communities. European Union council directive of 3 December 1987 on the approximation of the laws of the Member States relating to the measures to be taken against the emission of gaseous and particulate pollutants from diesel engines for use in vehicles; 1988. 88/77/EEC.
- 6- Council of the European Communities. Directive 1999/96/EC of the European parliament and of the council of 13 December 1999; 1999. 1999/96/EEC.
- 7- European Parliament and the Council of the European Union. Regulation (EC) No 595/2009 of 18 June 2009; 2009
- 8- DieselNet. <http://www.dieselnets.com/>; 2009.
- 9- US EPA. Summary of current and historical light-duty vehicle emissions standards, www.epa.gov/greenvehicles/detailedchart.pdf; 2010.
- 10- Suzuki, H., Koike, N., Ishii, H., Odaka, M., 1997. Exhaust Purification of Diesel Engines by Homogeneous Charge with Compression Ignition Part 1: Experimental Investigation of Combustion and Exhaust Emission Behavior Under Pre-Mixed Homogeneous Charge Compression Ignition Method. SAE Paper 970313.
- 11- Suzuki, H., Koike, N., Ishii, H., Odaka, M., 1997. Exhaust Purification of Diesel Engines by Homogeneous Charge with Compression Ignition Part 2: Analysis of Combustion Phenomena and NO_x Formation by Numerical Simulation with Experiment. SAE Paper 970315.
- 12- Senda, J., Ikeda, M., Yamamoto, M., Kawaguchi, B., Fujimoto, H., 1999. Low Emission Diesel Combustion System by Use of Reformulated Fuel with liquefied CO₂ and n-Tridecane. SAE Paper 1999-01-1136
- 20
- 13- Kawano, D., Senda, J., Kawakami, K., Shimada, A., Fujimoto, H., 2001. Fuel Design Concept for Low Emission in Engine Systems -2nd report Analysis of Combustion Characteristics for the mixed fuels. SAE Paper 2001-01-1071.

- 14- Adomeit, P., Pischinger, S., Becker, M., Rohs, H., Greis, A., Grünefeld, G., 2006. Potential Soot and CO Reduction for HSDI Diesel Combustion Systems. SAE Paper 2006-01-1417.
- 15- Miyamoto, N., Ogawa, H., Nurun, N.M., Obata, K., Arima, T., 1998. Smokeless, Low NO_x, High Thermal Efficiency, and Low Noise Diesel Combustion with Oxygenated Agents as Main Fuel. SAE Paper 98-05-06.
- 16- Kitamura, T., Ito, T., Senda, J., and Fujimoto, H., 2001. Detailed Chemical Kinetic Modeling of Diesel Spray Combustion with Oxygenated Fuels. SAE Paper 2001-01-1262.
- 17- Xu, Y., Lee, C.F., 2006. Study of Soot Formation of Oxygenated Diesel Fuels Using Forward Illumination Light Extinction (FILE) Technique. SAE Paper 2006-01-1415.
- 18- J.E.Dec. A Conceptual Model of DI Diesel Combustion Based on Laser-Sheet Imaging. SAE, 970873 (1997).
- 19- Majewski, W.A., Khair, M.K., 2006. Diesel Emissions and Their Control. SAE International
- 20- Challen, B. & Baranescu, R. eds., 1999. Diesel Engine Reference Book. Second Edition, Butterworth-Heinemann: Oxford, UK.
- 21- D. M. Peirce, N. S. I. Alozie, D. W. Hatherill, and L. C. Ganippa . Premixed Burn Fraction: Its Relation to the Variation in NO_x Emissions between Petro- and Biodiesel. Energy Fuels 2013, 27, 3838–3852
- 22- L. Labecki, L.C. Ganippa. Effects of injection parameters and EGR on combustion and emission characteristics of rapeseed oil and its blends in diesel engines. Fuel.2012.03.029
- 23- Rakesh KumarMaurya , DevDattPal , AvinashKumarAgarwal. Digital signal processing of cylinder pressure data for combustion diagnostics of HCCI engine. Mechanical Systems and Signal Processing 36 (2013) 95–109
- 24- S L Kokjohn and R D Reitz. Investigation of charge preparation strategies for controlled premixed charge compression ignition combustion using a variable pressure injection system. International Journal of Engine Research 2010 11: 257
- 25- T Li, M Suzuki and H Ogawa. Effect of Two-Stage Injection on Unburned Hydrocarbon and Carbon Monoxide Emissions in Smokeless Low-Temperature Diesel Combustion with Ultra-High Exhaust Gas Recirculation. International Journal of Engine Research 2010 11: 345

- 26- Zhen Huang, Libin Ji, Dong Han, Zheng Yang and Xingcai Lu. Experimental study on dual-fuel compound homogeneous charge compression ignition combustion. International Journal of Engine Research 2013 14: 23
- 21
- 27- Kwanhee Choi, JuwonKim, AhyunKo, Cha-LeeMyung, SimsooPark ,n,Jeongmin Lee . Size-resolved engine exhaust aerosol characteristics in a metal foam particulate filter for GDI light –duty vehicle. Journal of Aerosol Science 57 (2013) 1–13
- 28- Sara Pinzi , Paul Rounce , José M. Herreros, Athanasios Tsolakis M. Pilar Dorado. The effect of biodiesel fatty acid composition on combustion and diesel engine exhaust emissions. Fuel 104 (2013) 170–182
- 29- Karavalakis, G., Bakeas, E., Stournas, S., 2010. An Experimental Study on the Impact of Biodiesel Origin and Type on the Exhaust Emissions from a Euro 4 Pick-up Truck. SAE Paper 2010-01-2273
- 30- Kawano, D., Mizushima, N., Ishii, H., Goto, Y., Iwasa, K., 2010. Exhaust Emission Characteristics of Commercial Vehicles Fuelled with Biodiesel. SAE Paper 2010-01-2276
- 31- J. Kim , Kwanhee Choi , Cha-Lee Myung , Youngjae Lee , Simsoo Park . Comparative investigation of regulated emissions and nano-particle characteristics of light duty vehicles using various fuels for the FTP-75 and the NEDC mode. Fuel 106 (2013) 335–343
- 32- S. Ushakov , Harald Valland , Vilmar Æsøy . Combustion and emissions characteristics of fish oil fuel in a heavy-duty diesel engine. Energy Conversion and Management 65 (2013) 228–238
- 33- V. Bermudez , Jose´ M. Lujan, Benjami´n Pla, Waldemar G. Linares. Comparative study of regulated and unregulated gaseous emissions during NEDC in a light-duty diesel engine fuelled with Fischer Tropsch and biodiesel fuels. b i o mass and bioenergy 3 5 (2 0 1 1) 7 8 9-7 9 8
- 34- B. Kegl. Influence of biodiesel on engine combustion and emission characteristics. Applied Energy 88 (2011) 1803–1812
- 35- Seung Hyun Yoon, Chang Sik Lee. Effect of biofuels combustion on the nanoparticle and emission characteristics of a common-rail DI diesel engine. Fuel 90 (2011) 3071–3077.

- 36- M. Mani , G. Nagarajan. Influence of injection timing on performance, emission and combustion characteristics of a DI diesel engine running on waste plastic oil. *Energy* 34 (2009) 1617–1623
- 37- Á Díez, H Zhao, T Carrozzo, A E Catania and E Spessa. Development of a high-speed two-colour system and its application to in-cylinder diesel combustion temperature and soot measurements with split injections. *Proceedings of the Institution of Mechanical Engineers, Part D: Journal of Automobile Engineering* 2012 226: 684
- 38- M. R. Herfatmanesh and Hua Zhao. Experimental investigation of effects of dwell angle on fuel injection and diesel combustion in a high-speed optical CR diesel engine. *Proceedings of the Institution of Mechanical Engineers, Part D: Journal of Automobile Engineering* 2013 227: 246.
- 39- José M Desantes, José M Luján, Benjamín Pla and José A Soler. On the combination of high-pressure and low-pressure exhaust gas recirculation loops for improved fuel economy and reduced emissions in high-speed direct-injection engines. *International Journal of Engine Research* 2013 14: 3
- 40- V. Bermúdez , José M. Lujan, Benjamín Pla, Waldemar G. Linares. Effects of low pressure exhaust gas recirculation on regulated and unregulated gaseous emissions during NEDC in a light-duty diesel engine. *Energy* 36 (2011) 5655-5665.
- 41- Sarangi, A.K., McTaggart-Cowan, G.P., Garner, C.P., 2010. The Effects of Intake Pressure on High EGR Low Temperature Diesel Engine Combustion. *SAE Paper* 2010-01-2145.
- 42- D.C. Rakopoulos. Heat release analysis of combustion in heavy-duty turbocharged diesel engine operating on blends of diesel fuel with cottonseed or sunflower oils and their bio-diesel. *Fuel* 96 (201 2) 524–534
- 43- S. Manasra, D. Brueggemann. Effect of Injection Pressure and Timing on the In-Cylinder Soot Formation Characteristics of Low CR Neat GTL-Fueled DI Diesel Engine. *SAE Paper* 2011-01-2464
- 44- C. Sayin , M. Gumus. Impact of compression ratio and injection parameters on the performance and emissions of a DI diesel engine fueled with biodiesel-blended diesel fuel. *Applied Thermal Engineering* 31 (2011) 3182-3188.
- 45- S. Puhan, R. Jegan, K. Balasubbramanian, G. Nagarajan, Effect of injection pressure on performance, emissions, and combustion characteristics of high linolenic

linseed oil methyl ester in a DI diesel engine, Renewable Energy 34(2009) 1227-1233.

46- Heywood, J.B., 1988. Internal Combustion Engine Fundamentals McGraw-Hill Science Engineering.

Speed Sensorless Control Based Artificial Neural Network for Direct Current Motor

Dr. Adel M. Dakhil^{*}, Dr. Basil H. Jasim^{**}.

^{*}Department of Electrical Engineering, College Of Engineering.

Misan University

Dr.adelmana@yahoo.com

^{**}Department of Electrical Engineering, College Of Engineering.

University of Basra

Abstract

In this paper, A robust adaptive speed sensorless by a neural network approach of a separately excited (DC) motor without the use of speed sensors is presented. The simulation carried out by Matlab backage. The actual speed is estimated using a feed-forward neural network, the neural estimator have three inputs which are armature current, armature voltage, and the speed in the previous step of time; and one output which represents the estimated speed. The obtained results are presented to show the validity and efficiency of sensorless control scheme, which in turn obtains high performances.

الخلاصة

في هذا البحث متحسس تم دراسة سرعة لمحرك تيار مستمر منفصل الأثرية متأقلم قوي باستخدام منظومة عصبية. منظومة المحاكاة صممت باستخدام برنامج Matlab. السرعة الحقيقية خُمنَت باستخدام منظومة عصبية ذات الارتجاع المسبق. هذه الشبكة العصبية لها ثلاث مدخلات (تيار المنتج ، فولتية المنتج، والسرعة عند الخطوة الماضية من الزمن)؛ و أخرج واحد يمثل السرعة المخمنة ، النتائج المستخلصة أظهرت ببيان مصداقية وكفاءة مخطط سيطرة متحسس السرعة لاستخراج خصائص جيدة

I. Introduction

Because of their high reliabilities, flexibilities and low costs, DC motors are widely used in industrial applications such as electric vehicles, steel rolling mills, electric cranes, robotic manipulators, and home appliances where speed or/and position control of motor are required. Generally, a high performance motor drive system must have good dynamic speed command tracking and load regulating response[1].

Therefore, the control of the position or/and speed of a DC motor is an important issue and as been studied since the early decades in the last century [2-3]. DC motors are customarily modeled linearly to enable the application of linear control theory in controller design[4].

Artificial Neural Network (ANN_s), which is based on the operating principle of human being nerve neural. This method is applied to control the motor speed [2]

The key of Artificial Intelligence Control (AIC) is how to construct inverse model of controlled system accurately [5 - 9]. The purpose of this study is to estimate and control the speed of a separately excited DC motor with Artificial Neural Network (ANN) controller using MATLAB software application. Among different kinds of neural networks, the most widely used ones are multilayer neural networks and recurrent networks[10].

weerasoory S. and al-sharkawi M.A, 2009 [2] presents new concepts of Artificial Neural Networks (ANN) in estimating speed and controlling the separately excited DC motor. Vince T., 2009 [10] this research presents regulation possibilities of DC motor via Internet and deals with artificial neural network utilization in such a regulation. In [4] Fielat EA, Ma'aita EK, 2012 , a neural network approach for the identification and control of a separately excited direct (DC) motor (SEDCM) driving a centrifugal pump load is applied. In this application, two radial basis function neural networks (RBFNN) are used to control the machine.

Simulation results are presented to demonstrate the effectiveness and advantage of estimating the speed of DC motor with ANNs in comparison with the conventional estimating schemes.

The organization of this paper is as follows. In section II, the mathematical modeling for a separately excited DC motor. The basic concept of AIC is briefly reviewed in section III. Section IV presents some simulation results on a separately excited DC motor with the new proposed technique. The last section V contains the conclusion.

II. Mathematical Model of DC Motor

The DC machine are characterized by their versatility. By means of various combinations of shunt, series, separately excited field windings they can be designed to display a wide variety of volt-ampere or speed torque characteristics for both dynamics and steady state operation [9, 11].

The separated excitation DC motor model is chosen in this paper due to its good electrical and mechanical performances as compared with the other dc motor models.

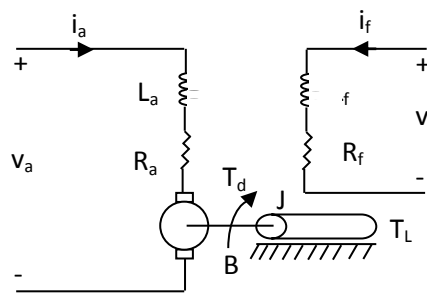


Fig.(1) The equivalent circuit of DC motor with separate excitation

The resistance of the field motor winding and its inductance used in this work are represented by R_f and L_f respectively. The resistance of the armature and its inductance are shown by R_a and L_a respectively.

Armature reactions effects are ignored in the description of the motor, The voltage V_f which applied to the field has constant value. A linear model of a simple DC motor consists of mechanical equation and electrical equation as determined in the following equation

$$J_m \frac{dw_m}{dt} = k_m \phi I_a - b w_m - T_{load} \quad (1)$$

$$k_b w = v_a - R_a I_a - L \frac{di}{dt} \quad (2)$$

Where R_a is armature resistance (Ω)

L_a is the armature inductance (Ω)

J_m moment of inertia

$k = k_b \phi$ =motor constant (Nm/Amp.)

$k = k_m \phi$ =motor constant (Nm/Amp.)

b is the damping ratio of mechanical system (Nms)

Thus from eq.(2), the rotor speed can be estimated.

In this work a feed forward back propagation neural network is presented which is trained to approximate eq.(2)

Table (1)

Motor Parameters Value

Parameters	Definition	Value
V_a	Terminal voltage (V)	240
I_a	Armature current (Amp.)	16.2
T_l	Load torque	15
J	Rotor inertia (J/Kg.M ²)	1
B	Viscous friction coefficient	0
R_a	Armature resistance (Ω)	0.6
L_a	Armature inductance (H.)	0.012
N	Rotor speed (R.p.m.)	1220

The dynamics model of the system is formed using these differential equation and the matlab simulink as shown in Fig.(2)

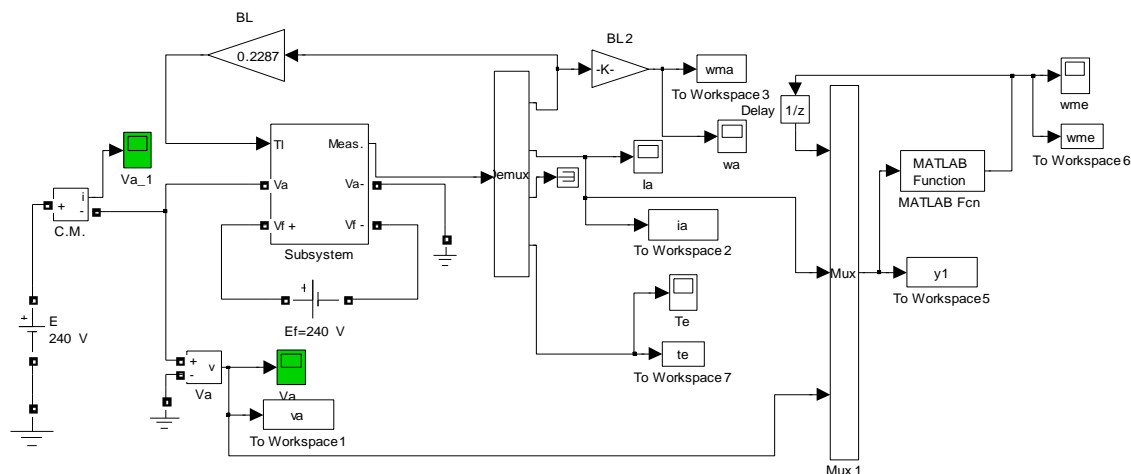


Fig.(2) Simulink model for DC Motor with neural network

III. Artificial Neural Network (ANN)

The approach of neural network basically works on the provided priorities information and makes a suitable decision for a given testing input based on the provided training information [1]. The signals activation of nodes either attenuate or amplify, when transmitted to next layer. ANNs are trained to emulate a function by a presenting it with representative set of input/ output functional technique adjusts the weights in all connecting links and thresholds in the nodes so that the difference between the actual output and target output is minimized for all given training patterns [2]. The number of inputs and outputs are the only fixed parameters for a designing and training an ANN to emulate a function, which are based on the input / output variables of the function. It is also widely accepted that maximum of the two hidden layers are sufficient to learn any arbitrary non linearity [12]. First and second layer is the hidden layers, Third layer is the output layer.

The most common feed forward neural network is shown in Fig.(3), the basic component of the network, called neurons. The network consists of three layers : input layer, the hidden layer, and the output layer, each of the input is connected to each neurons in the hidden layer, and in turn, each of the hidden layer neurons is connected to the output, each single neurons can be represented as shown in Fig.(4)

However the hidden neurons and the values of learning parameters, which are equally critical for a satisfactory learning, are not supported by such well established selection criteria. The choice is usually based on experience. The ultimate objective is

to find a combination of parameters which gives a total error of required tolerance a reasonable number of training sweeps [2,3]. The structure and the process of learning ANNs for estimation and control a speed for D.C. motor is shown in Fig.(3)

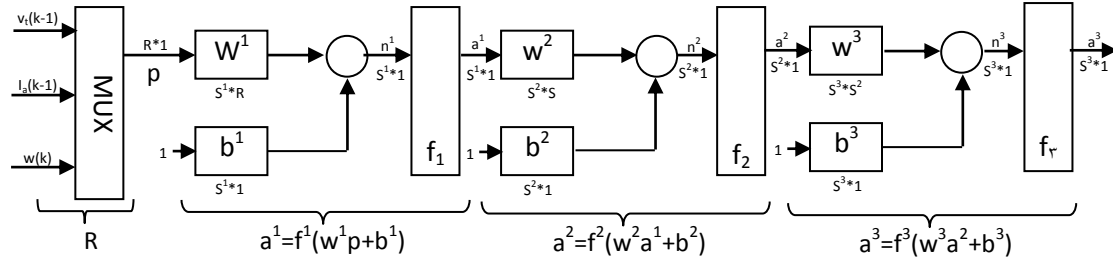


Fig.(3) Three layer network for the presented estimator

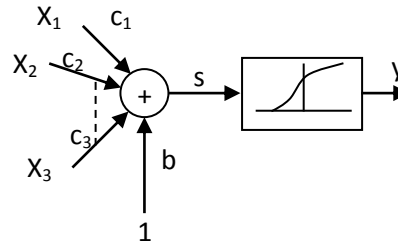


Fig.(4) Single neuron structure

Typically, a sigmoided squashing function is used, that is,

$$y = \frac{1}{1 + e^{-ks}} \quad (3)$$

Where k is constant and if $-\infty < s < \infty$ then $0 < y < 1$

Nonlinearity of the squashing function allows the neural network to model nonlinear phenomena, the argument, s, of the squashing function is given by

$$s = b + \sum_{i=1}^j c_i x_i \quad (4)$$

Where x_i , $i=1,2,\dots,j$, are neurons input signals, c_i are respective connection weights, and b is the bias weight.

To work properly, a neural network must be trained, that is, its weights must be set to values resulting in the required quality of operation. The training process consists of sequential application of various sets of inputs, evaluating the difference between the

outputs and their reference values, and adjusting the weights to minimize that difference. The training process is usually based on the efficient back propagation algorithm [13]. The training is automated and preformed prior to employing the network in the simulated circuit.

IV. Simulation Results

To study the performance of speed estimator by using the artificial neural network (ANN) for DC motor (DC motor parameters shown in Table 1), the simulation of the system was conducted using Simulink/ Matlab program with the toolbox of neural network is used. The DC motor has the parameter listed in Table(1).

The neural network was trained using four sets of input/ target pairs, each pair corresponding to excitation case, the training process of the ANN is shown in Fig.(5) the performance is (0.00010287) with (100) epochs

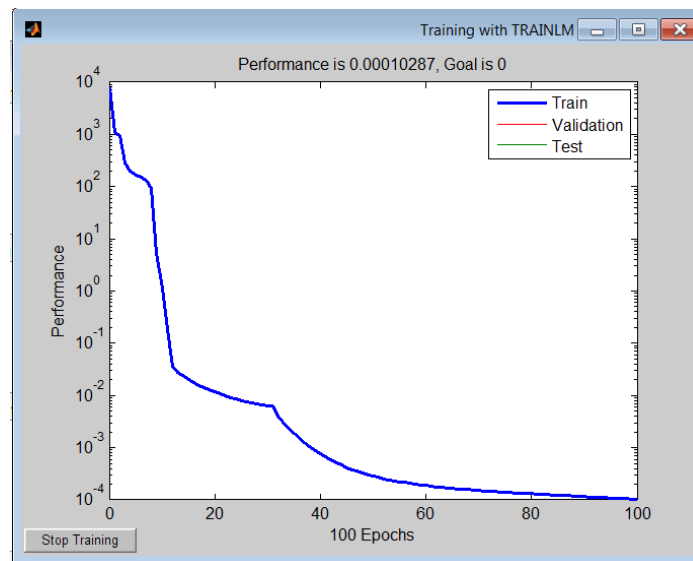
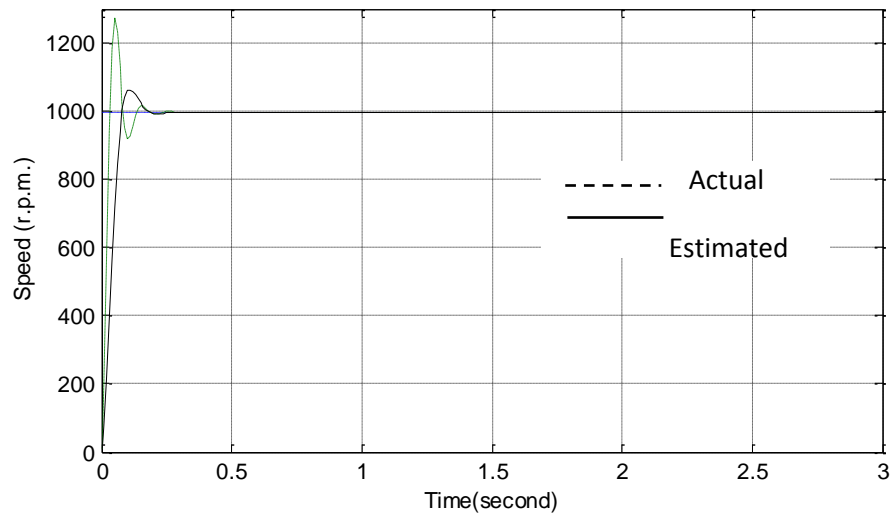
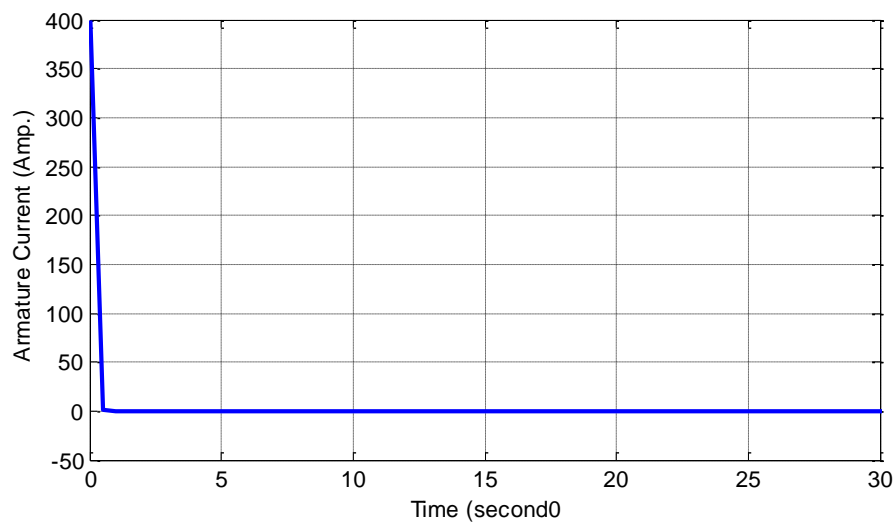


Fig.(5) Error of the Neural Network

Now the ANN is used to estimate the speed of the motor, the corresponding actual speed, estimated speed, armature voltage and current with the developed torque is shown in Fig.(6) –Fig.(8)

**Fig.(6) Actual and estimated speed****Fig.(7) Armature current waveform for the tested DC Motor**

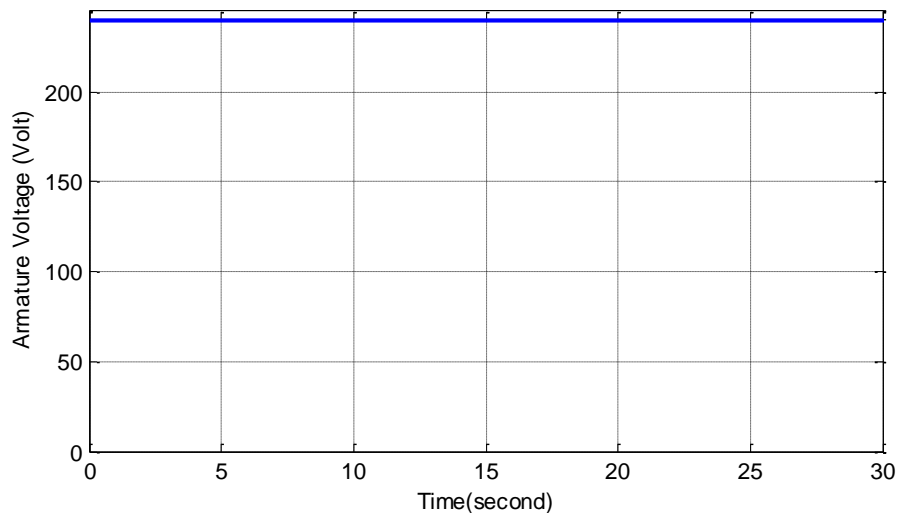


Fig.(8) Armature voltage waveform for the tested DC Motor

Other test for this estimator is done by using a step change of 15 N.m. loads at $t=5$ sec and observing the performance of this system.

From results shown in these two tests the estimation process by this Artificial Neural Network (ANN) is robustness the fluctuation of the estimated speed and to the variation of load torque. This network is able to estimate not only the speeds included in the training set, but it also is able to interpolate and extrapolate well.

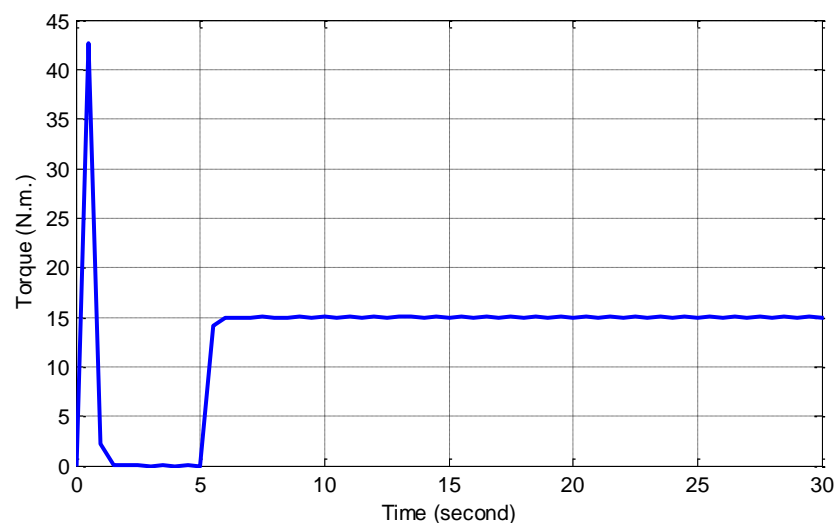


Fig.(9) Torque profile for DC motor with step change in torque equal 15 N.m. at $t=5$ second

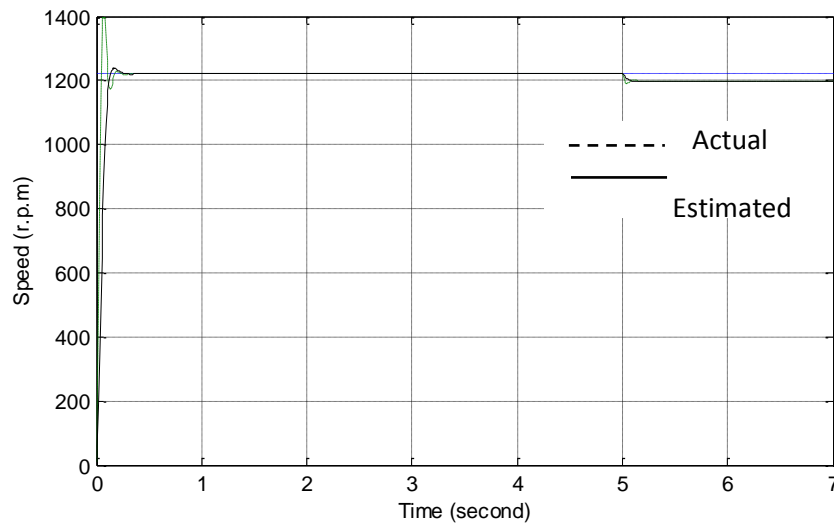


Fig.(10) Actual and estimated speed profile for DC motor with step change in torque equal 15 N.m. at t=5 second

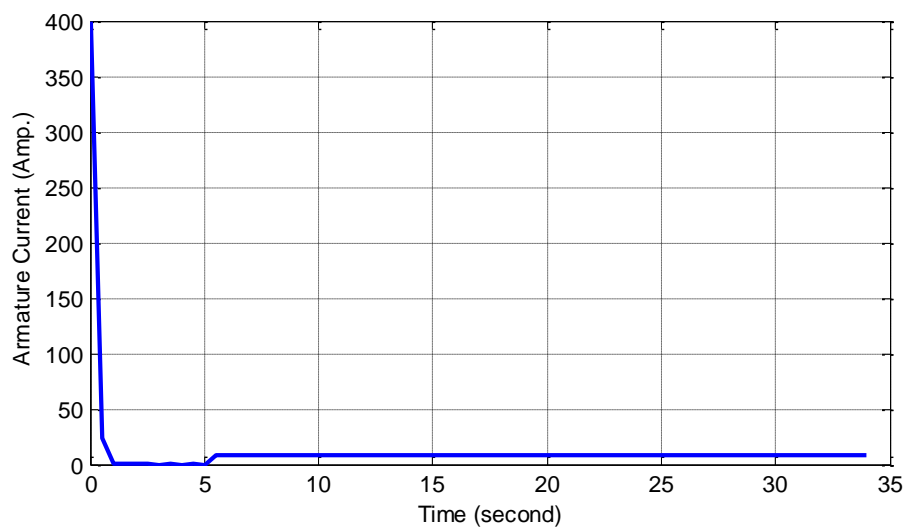


Fig.(10) Armature current waveform for DC motor with step change in torque equal 15 N.m. at t=5 second

V. Conclusion

In this work the speed of DC motor has successfully estimated and controlled using Artificial Intelligence, this work is trained to emulate function, by application such network there is no need to use speed sensors hence the speed estimated by measurement the armature current and voltage. The simulation results demonstrate that this estimator is able to estimate not only the speeds included in the training sets,

but it is able to interpolate and extrapolate very well, this estimator also able cover the variation of speed due to load change.

References

1. Arti A., Ilyas Md. May 2012," Speed Control of DC Motor using Neural Network Configuration" , International Journal of Advanced Research in Computer Science and Software Engineering, Vol.2, No.5,p.p209-212
2. weerasoory S. and al-sharkawi M.A, December 2009, " Identification and control of a DC Motor using back-propagation neural networks" , IEEE transactions on energy conversion, Vol.6, No.4, pp.663-669.
3. Psaltis D. , Sideris A. and Yamamura A. A., 1988, " A Multilayered Neural Network Controller", IEEE Control system Magazine, Vol.4, No.1, 17-20.
4. Fielat EA, Ma'aita EK, 2012," RBF Neural Network Approach for Identification and Control of DC Motors" , TJER, Vol.9.No.2, p.p.80-89.
5. Scott G.M.,1993" Knowledge – Based Artificial Neural Networks for Process Modeling and Control" , PhD. Thesis, University of wesconsin.
6. Gankin S. G., 2001," The Computing Modeling for Power Electronics Systems in Matlab" , IEEE transactions on energy conversion, Vol.4 , No.1, pp. 165-173.
7. Rasid G., September 2000," High performance Nonlinear MIMO Field Weakening Controller of a Separately Excited DC Motor", Electric power Systems Research, Vol.55 , issue 3, pp. 157-164.
8. Chang J.S.R., Sun C.T., and Mizuttani E. , " Neuro-Fuzzy and soft computing' Prentice Hall , Upper Saddle River, NJ, 1997.
9. Raghavan S. , " Digital Control for Speed and Position of a DC Motor", M.Sc. Thesis , Texas A&M University , Kingsville, August2005.
10. Vince T., October 2009," Artificial Neural Network in Remote DC Motor Speed Regulation via Internet", XI International PhD Workshop OWD2009, p.p.419-422.

11. H. N. Koivo and J. T. Tantt, "Tuning of PID Controllers: Survey of SISO and MIMO Techniques," in Proceedings of Intelligent Tuning and Adaptive Control, Singapore, 1991.
12. Levin E. , Gewirtzman R., and Inbur G.F. 1991," Neural Network Architecture for Adaptive System Modeling Control", IEEE Control system Magazine, Vol.2, No.4, pp. 185-191.
13. Nabil A. , March 2005 , " Modeling and Simulation of AC-DC Buck-Boost Converter Fed DC Motor with Uniform PWM technique, Electric Power Systems Research, Vol.73, issue3, pp.363-372.

Non linear vibration analysis of liquid storage tank

Dr. Abdulamir A. Karim

Civil Engineering Department, College of Engineering, University of Basrah

Thamer hussein amer

Civil Engineering Department, College of Engineering, University of Basrah

ABSTRACT

This study presents an idealization scheme for the analysis of rectangular storage tanks acted upon by earthquake excitations. Above and below ground tank, are considered. A linear three-dimensional finite element analysis is adopted to predict the natural frequencies. The analysis parameters are the ratio of height to length of the tank, the type of soil, level of water in the tank, and also the wall thickness. Tanks made from steel as well as from concrete are investigated. A general purpose finite element program (**ANSYS 12.0**) used to model the analysed system. The tank base and wall are modelled by plane strain shell elements. The contained liquid is represented by a special solid element. Finally, the soil is modelled by simple spring-damper elements. The soil medium is idealized by the elastic half space model, that is, linear springs are assumed to represent the structure-soil interface. Which is then modelled by two-node spring dashpot elements. Forced vibration analysis is conducted on above ground and buried concrete tank. This analysis is carried out by applying the records of the North-South component of the 1940 El Centro earthquake with peak acceleration of 0.32g. It is found that the bending stresses in above ground concrete tank is (74.167) % greater than the stresses in buried tank with the same dimensions.

Key words: Seismic analysis, viscous dampers, rectangular tanks, finite element models, fluid-structure-soil interaction, time history, free vibration, ANSYS.

الخلاصة

تتضمن الدراسة تحليل الخزانات المستطيلة المعرضة الى هزات أرضية بحالتين، الأولى تكون فيها الخزانات مدفونة بشكل كامل تحت الارض والحالة الثانية تكون الخزانات فيها فوق مستوى سطح الارض. استخدمت طريقة العناصر المحددة للتحليل الخطي ثلاثي الابعاد وذلك لغرض تحري علاقة كل من الاهتزاز الطبيعي ونسبة ارتفاع الجدران من حيث تغير نوع التربة وكمية الماء الموجودة بالخزان وكذلك علاقة أيضا باختلاف سمك الجدران. تم تحري نوعين من الخزانات احدهما حديد والاخر كونكريت بصورة عامة تم استخدام طريقة العناصر المحددة باستخدام برنامج (ANSYS 12.0) لغرض التحليل. كل من قاعدة وجدار الخزان مثلت باستخدام عنصر الطبقة القشرية. السائل داخل الخزان مثل باستخدام العنصر الخاص بالعناصر الصلبة. وأخيرا تم تمثيل التربة باستخدام العنصر البسيط (spring-damper). بحيث تم نمذجة الوسط الترابي اعتمادا على مبدأ نصف الفضاء المرن (Elastic Half Space) بفرض وجود نوابض خطية مرنة (Elastic Springs). تم حل معادلات الأتزان باستخدام طريقة التكامل المباشر وباعتماد طريقة (Newmark) لهذا الغرض. خصائص الاهتزاز الحر للخزان تم إثباتها مقارنة مع نتائج نظرية سابقة. تم اجراء دراسة موسعة تأخذ بنظر الاعتبار اهم العوامل المؤثر على التصرف الديناميكي للخزانات أثناء الاهتزاز الحر أو أثناء الزلزال. تحليل الاهتزاز القسري تتضمن حالات دراسة لخزان كونكريتي، فوق التربة ومدفونة كلياً. حيث تم ايجاد كل من الازاحة وقوى القص والعزم والأجهاد للخزان الكونكريتي. نوع الهزة الأرضية التي استخدمت هي (EL Centro) 1940 في كاليفورنيا. ان قيمه القصوى للتعجيل هو $0.32g$. النتائج اظهرت بأن أجهاد الانحناء اكبر لحالة الخزان فوق التربة مما لو كان مدفوناً بنسبة 74.167% لنفس ابعاد الخزان الكونكريتي.

Introduction

Liquid storage tanks are important components of lifeline and industrial facilities. Behavior of large tanks during seismic events has implications far beyond the mere economic value of the tanks and their contents. Similarly, failure of tanks storing combustible materials, can lead to extensive uncontrolled fires. A study on the effect of the geometry of the tank foundation on the modal properties of the tank-liquid-soil system in which both fluid-structure and soil-structure interactions studied by **Hosseini and Mohajer [1] in (2000)**. The free vibration analysis of circular cylindrical fully anchored ground supported steel liquid storage tanks studied by **Atalla [2] in (2008) and Saadi [3] in 2008**. **Malhotra ,Veletsos and Tang [4] in 1993** and **Malhotra and Veletsos [5] in 1994** investigated the principal effects of base uplifting on the seismic response of ground supported cylindrical steel tanks which were unanchored with their base. **JIN et al.[6] in 2004**, presented the

earthquake response analysis of LNG storage tank by Simple beam-stick model. Also showed that the sloshing height could be underestimated when it is considered only one sloshing mode. The methods which used : the finite element method (FE), lumped mass and spring model. **Sanchez, Salas and Dominguez [7] in 2004**, investigated the behavior, under seismic conditions, of already existing steel storage tanks of large capacity, located in high risk zones with a strong ground motions (MEXICO). Dynamic analysis of cylindrical storage tanks anchored to rigid base, empty, filled and partially filled with liquid are considered studied by **Haroun[8] in (1980)**, **Seyoum[9] in (2005)**, **Lateef A. [10] in (2010)** and **Khtar [11] in 2012**. **Malhotra and Eeri M.[12] in 2005**, Presented a simple method to estimate the additional loads on tank's roof, wall and foundation due to impacts from the sloshing waves which caused by long-period ground motions. **O R Jaiswal et al. [13] in 2007** and **P. Pal [14] in 2009**, investigated the sloshing of liquid in partially filled container subjected to external excitation.

1. BASIC ASSUMPTIONS

The assumptions introduced in the present analysis are as follows:

- The tank is symmetric about x-axis and z-axis in terms of geometry.
- The material of the tank is linearly elastic, isotropic and homogeneous.
- The contained liquid is inviscid, incompressible and in a non-rotational motion, within vessels having no net flow rate
- The base is connected rigidly to the tank wall.
- The soil medium is represented as a system of closely spaced independent linear springs, masses and dashpots.
- The seismic effect is parallel to the z-axis and perpendicular to the x-axis.

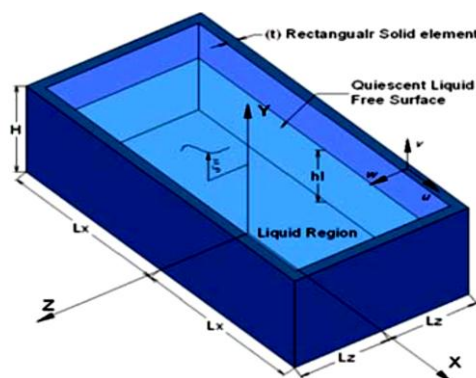


Plate (1) Rectangular storage tank and Coordinate system

2. Parametric Studies for Rectangular Concrete Tanks

To study the effect of tank geometry on natural frequencies, an examination of the above ground and buried tanks, is conducted. The properties of material used in all cases of the parametric study are as follows:

- Concrete is used for base and walls of the tank whose properties are: $E_c = 20 \times 10^6 \text{ kN/m}^2$, $\nu_c = 0.15$ and $\rho_c = 2400 \text{ kg/m}^3$.
- Water is used as a contained liquid of the tank having density of 1000 kg/m^3 , $E_w = 2.0684 \times 10^9 \text{ kN/m}^2$ and $\nu_w = 0.19$ [ANSYS 2012].
- Three different models of soil types are carried out. The three types of soil are listed in table (1). [SOIL PROPERTIES(LPILE&COM624P)]

Table (4.5) Soil properties of all concrete models considered in the analysis

Soil Type	Modulus of subgrade reaction (kN/m^3)		Winkler Spring Stiffness K_s (N/m)	
	Vertical	Horizontal	Vertical	Horizontal
Dense	33900	22600	6864750	4576500
Medium	27150	18100	5497875	3665250
Soft	8140	5426.7	1648350	1098900

3. SEISMIC GROUND EXCITATION

The structure is assumed to be acted upon by a seismic ground motion. A peak ground acceleration (PGA) of $0.318g$ have been used. A rectangular concrete tank has been analyzed due to north-south component El-Centro earthquake of Fig. (1).

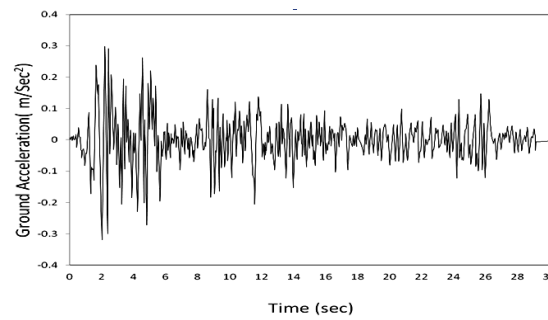


Figure (1): Accelerogram N-S El Centro earthquake, 18-May-1940

4. FINIT ELEMENT MODEL

The numerical analysis of the rectangular storage tank structure is performed on the basis of detailed FE model implemented with the help of the routines available in the ANSYS Finite Element program (ANSYS 2012). The rectangular storage tank is modeled for the two cases of tank considered in this work, i.e. the underground tank and the tank above ground. Four-noded shell elements (SHELL63) with six DOFs per node are used. The eight node solid fluid element (FLUID80), with three DOFs per node, has been chosen to model the incompressible fluid content. In order to satisfy the continuity conditions between the fluid

and solid media at the rectangular tank boundary, the coincident nodes of the fluid and shell elements are constrained to be coupled in the direction normal to the interface, while relative movements are allowed to occur in the tangential directions. Finally, concentrated mass elements (MASS21) and linear spring-damper elements (COMBIN14) are used to

model the discrete elements for the simulation of soil-structure interaction. The above FEM rectangular tank model is numerically analyzed by means of a full transient linear analysis. The governing equations of motion can be expressed in matrix form as (Chopra 1996):

$$[M]\{\ddot{u}\} + [C]\{\dot{u}\} + [K]\{u\} = \{F_{(t)}\}$$

with $[M]$, $[C]$ and $[K]$ being the mass, damping and stiffness matrices of the structure respectively, and $\{\ddot{u}\}$ the ground acceleration. Eq. (1) is integrated directly in time using the Newmark - β method.

5. NUMERICAL STUDY

Seismic response of the rectangular liquid storage tank above ground and underground is investigated by performing two types of analyses:

- (i) modal analysis, and
- (ii) time domain analysis.

6.1 Modal Analysis

The first step in the dynamic analysis of any structural system is to determine the free vibration characteristic natural frequencies and mode shapes, which are important in calculating the seismic response of the liquid storage tanks.

6.1.1 Effect of Tank Height to Length Ratio Variation

For this purpose, two cases of storage tanks are considered, the tank above ground and buried tank, for each empty and completely liquid filled tanks are examined. Tank length, $L=9.9\text{m}$, tank width $B=6.3\text{m}$ and the tank height, H_t , are varied from 1.8m to 12.6m at 1.8m increments to accommodate the aspect ratio (H_t/l_x) range of 0.2 to 1.4. $l_x = \text{Clear length} = 9\text{m}$. The results of natural frequencies are plots of Figures.(2) to (5) for empty and completely liquid fill tanks, for the three different types of soil. It is observed that the natural frequency for all modes decreases as the strength of supporting soil decrease. This can be justified due to the lowering of the stiffness of the system. And it has been noticed that the natural frequencies decreased when the ratio (H_t/l_x) increased because of the increasing of the tanks mass. In comparing the results between the two cases of the tanks (the tank above ground and buried tank), it has been found that the buried tank has natural frequencies less than the tank above ground, because the mass of the tank will increase and that will make the natural frequencies getting less. It is also noticed by examining these tables and plots, that the natural frequencies of the empty tank are much larger than those of the full tanks regardless of the type of soil.

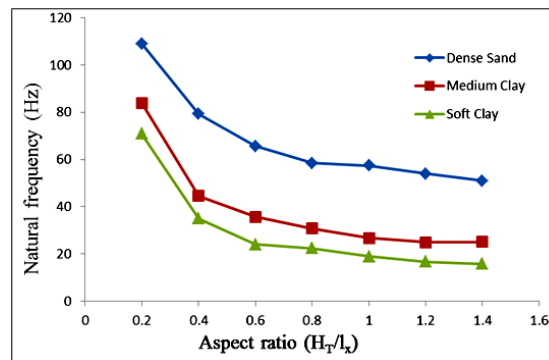


Figure (2): Fundamental natural frequencies versus aspect ratio (H_t/l_x) variation of empty tank above the ground

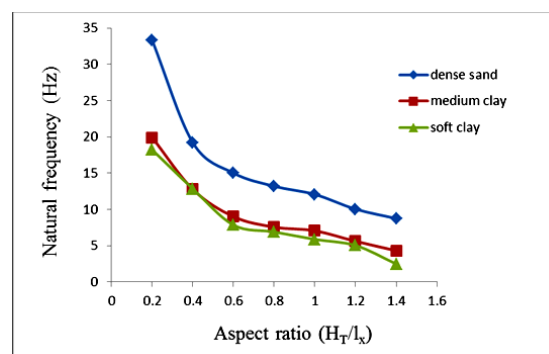


Figure (3): Fundamental natural frequencies versus aspect ratio (H_t/l_x) variation of full tank the above ground

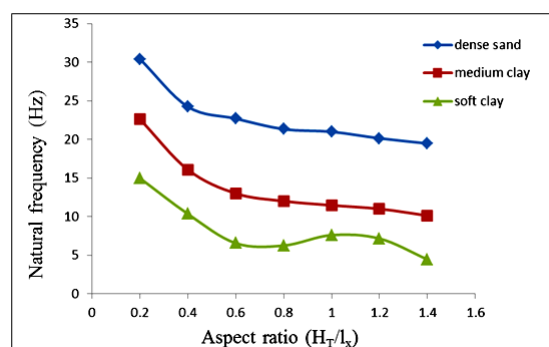


Figure (4): Fundamental natural frequencies versus aspect ratio (H_t/l_x) variation of empty buried tank

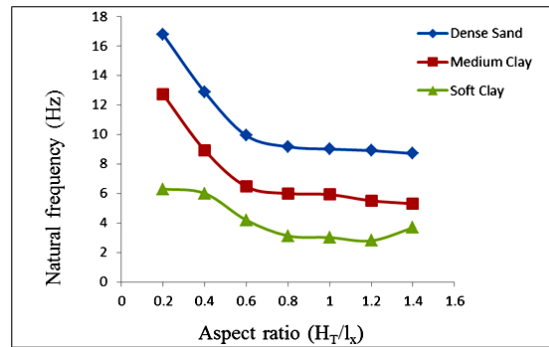


Figure (5):Fundamental natural frequencies versus aspect ratio (H_T/l_x) variation of full buried tank

6.1.2 Effect of Liquid Height to Tank Height Ratio Variation

To demonstrate the effect of liquid height variation (H_L/H_t), two cases of the tanks (the tank above ground and buried tank) were considered for this purpose. Tank length, $L=9.9\text{m}$, tank width $B=6.3\text{m}$ and the tank height, $H_t=5.4\text{m}$. Different values of liquid depths for the same three types of the soil were carried out to demonstrate the influence of liquid height on the dynamic characteristics. The resulting natural frequencies shown at Fig.(6) and (7) for above ground and buried tanks respectively. It can be observed from these plots that, as the level of fluid in the tank increases, the natural frequencies decrease for both cases of tanks and for all three types of the soil. This behavior is obvious since the mass of the structure system increases with the level of fluid.

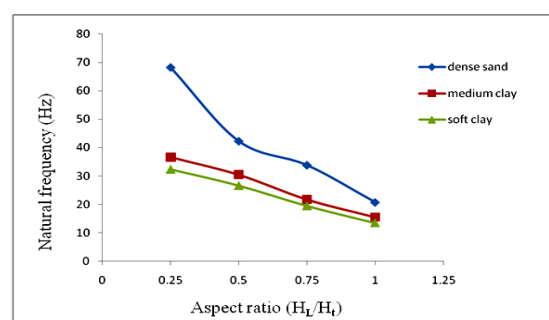


Figure (6):Fundamental natural frequencies versus filling ratio (H_L/H_t) of tank above ground

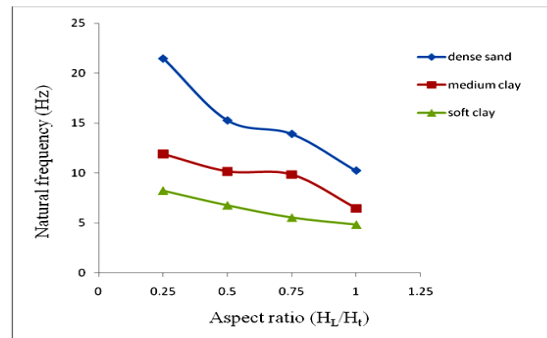


Figure (7): Fundamental natural frequencies versus filling ratio (H_L/H_t) of buried tank

6.1.3 Effect of Wall Thickness Variation.

To demonstrate the effect of wall thickness variation, empty tank and completely full tank, having dimensions 3.6m height, 9.9m length and 6.3m width is studied for the free vibration characteristics when its wall thickness varies from 450mm to 1350mm with one type of the surrounding soil (dense sand), and also for two cases (above ground and buried tank). The resulting natural frequencies are plots at Figs.(8) to (11). It can be seen clearly from these results that, the natural frequencies increases when the thickness of the wall increases without changing the height of the tank (the wall stiffness increases with increasing its thickness).

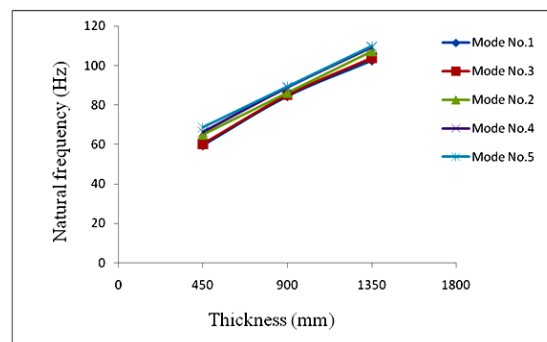


Figure (8): Effect of thickness variation on natural frequencies of empty tank above ground

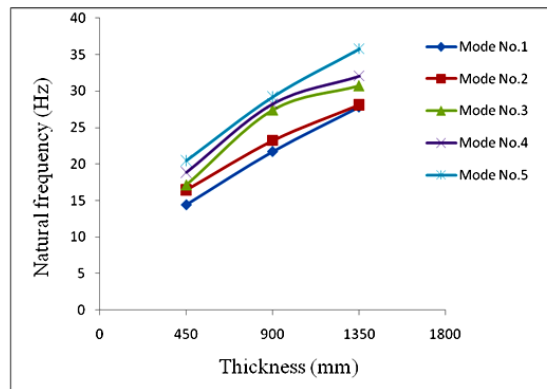


Figure (9): Effect of thickness variation on natural frequencies of full tank above ground

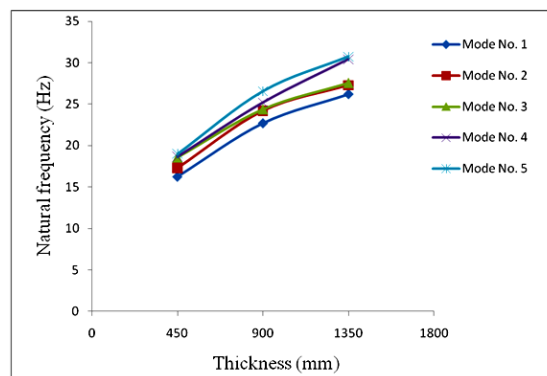


Fig. (10): Effect of thickness variation on natural frequencies of empty buried tank

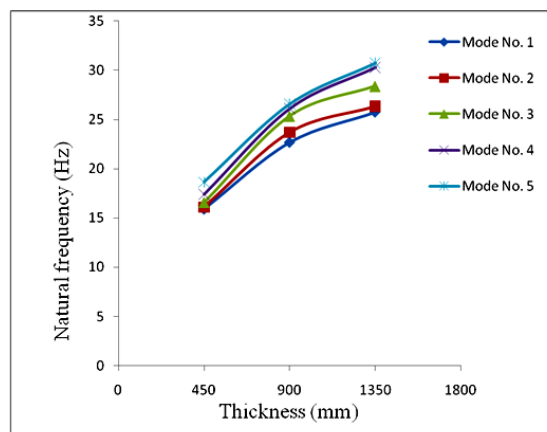


Figure (11): Effect of thickness variation on natural frequencies of full buried tank

6.2 Time Domain Analysis

A time domain analysis using the north-south component of the 1940 El Centro earthquake was used for the linear elastic model. Peak ground acceleration values were adjusted to 0.318g. Model time history analysis under linear elastic, small

deformation assumptions included evaluation of water surface profiles top displacements, axial force, and resulting base shear. These studies depend on two cases, the first case, is for an above ground tank and case two is for the tank underground (buried tank). The results are compared for each case for variant effects including (soil type and location of the tank). The damping ratio (ζ) is taken equal to 5% of the critical damping ratio and the acceleration duration is divided into several step with $\Delta t=0.02$ sec.

The tank dimensions for this model having length 9.9m, width 6.3m, height 12.6m, thickness of wall 45cm. The analysis shown the relationships between the displacement ,shear force ,bending moment , stresses and the time and also for the two cases (above ground and underground) are presented. In this case found the displacement (1.9 mm) for empty tank above ground as shown in the figure (12) ,greater than the displacement (0.032 mm) for tank underground as shown in figure(13) , the shear force is (2500 kN) for empty above ground tank as shown in the figure (14) greater than (2000 kN) for underground tank as shown in figure (15) , and the bending moment for empty tank above ground as shown in the figure (16) is (13000 kN.m) greater than (4500 kN.m) for underground tank as shown in figure (17).The maximum stresses for empty tank above ground as shown in figure (18) is (24 MPa)greater than (6.2 MPa) for underground tank as shown in figure (19).

The results for empty tank above ground appearance largest than underground due to the confined from soil also for the fixed support the displacement ,shear and bending moment less than simply support and the bending stresses according to maximum bending moment value.

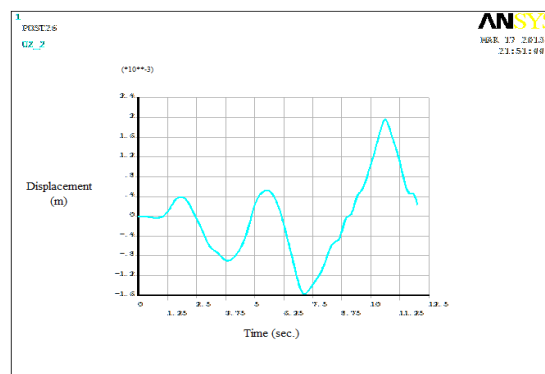


Fig. (12): The displacement for empty tank above ground

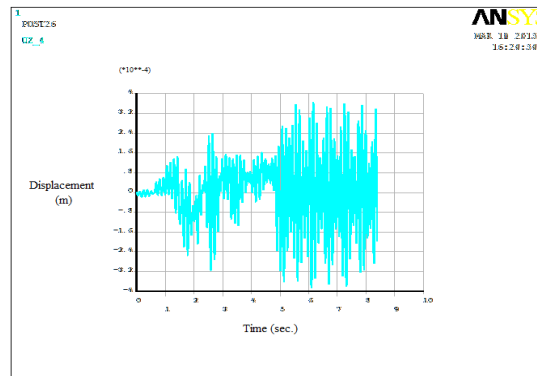


Fig. (13): The Displacement for empty tank under ground

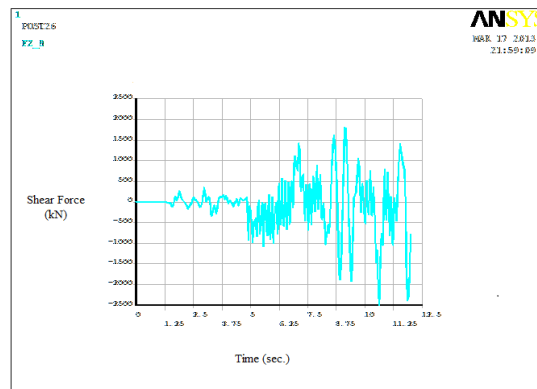


Fig. (14): Shear force for empty tank above ground

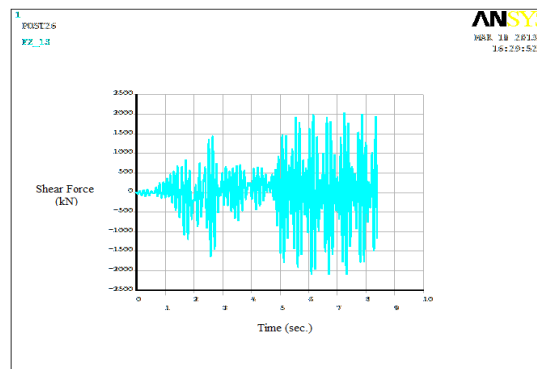


Fig.(15): Shear force for empty tank under ground

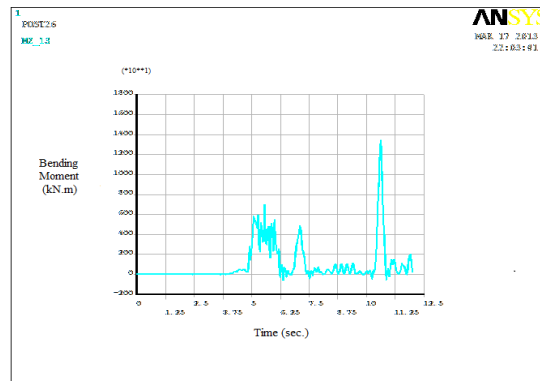


Fig. (16): Bending Moment for empty tank above ground

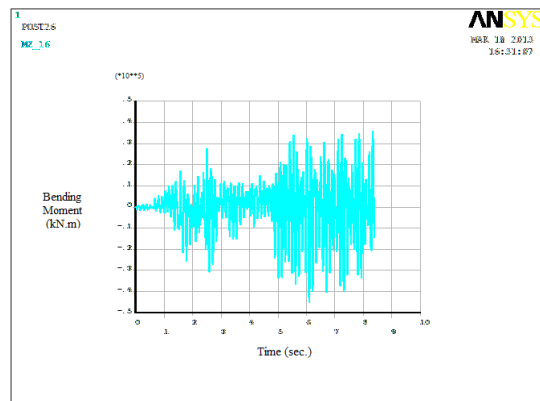


Fig. (17): Bending Moment for empty tank under ground

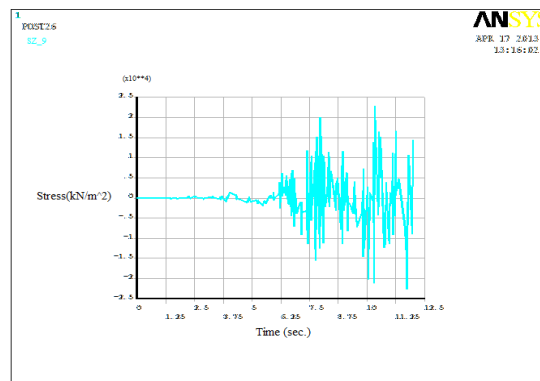


Fig. (18): Bending Stress for empty tank above ground

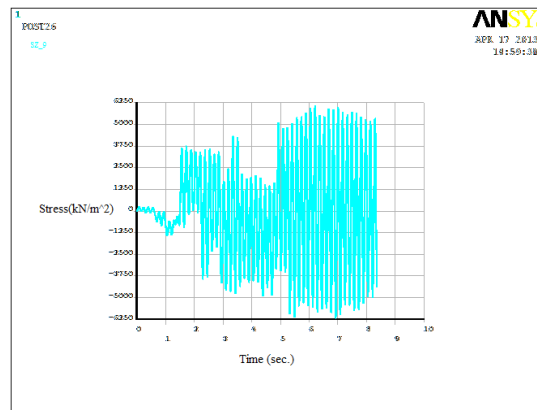


Fig. (19): Bending Stress for empty tank under ground

6. CONCLUSIONS

1. The wall and base of the tanks are modelled using four-node shell elements (**SHELL63** element). The fluid is modelled by using the eight-node brick elements (**FLUID80** element). The soil is modelled using two-node spring-dashpot element (**COMBIN14** element).
2. Buried tanks are found to have lower natural frequencies than comparable above ground tanks.
3. The natural frequency is found to decrease as the contained liquid level increases.
4. From seismic analysis it is found that the maximum displacement of above ground tanks is 1.9 mm while it is 0.032 mm for buried tank of similar dimension and subjected to the same earthquake loading.
5. Variations of the properties of surrounding soil medium are found to have an important influence on the free and forced vibrational response (seismic excitation) for the storage tanks.
6. The base shear for above ground tank have values (2500kN) greater than those in underground tank (2000kN).
7. The bending moment for above ground tank have values (13000kN.m) greater than those (4500kN.m) in underground tank.
8. The maximum bending stress for above ground tanks is found to be (24 MPa) and for underground tank is (6.2 MPa) when the two tanks are subjected to El Centro earthquake.

7. REFERENCES

1. Hosseini, M. and Mohajer, M. "Effects of foundation geometry on the natural periods of cylindrical tank-liquid-soil systems" JSEE, Vol. 2, No 4, 2000.
2. Atalla A. "Vibration analysis of circular cylindrical liquid storage tanks using finite element technique" PhD. Thesis, University of Basrah, 2008.
3. Saadi N. O. " Free vibration analysis of free-clamped circular cylindrical liquid storage tank" Msc. Thesis, University of Technology, 2008.
4. Malhotra P. K, Veletsos A. S. and Tang H. T. "Seismic response of unanchored liquid storage tank", Elsevier science publishers B.V, 1993.
5. Malhotra P. K and Veletsos A. S. " Uplifting analysis of base plates in cylindrical tanks " Journal of Structural Engineering, Vol. 120, No. 12 , Paper No. 6879 ,1994 .
6. Jin B. M. , Jeon S. J. , Kim S. W. , Kim Y. J. and Chung C. H. "Earthquake response analysis of LNG storage tank by axisymmetric finite element model and comparison to the results of the simple model "13th World Conference on Earthquake Engineering , Paper No. 394 ,2004 .
7. Sanchez H. S., Salas C. C. and Dominguez A. M." Structural behavior of liquid filled storage tanks of large capacity placed in seismic zones of high risk in Mexico "13th World Conference on Earthquake Engineering, Paper No. 2665, 2004.
8. Haroun M. A. "Dynamic analysis of liquid storage tanks" Report EERL 80-04, Pasadena, California, February 1980.
9. Seyoum S. "Dynamic analysis of liquid containing cylindrical tanks" Msc thesis, University of Addis Ababa, 2005.
10. Lateef H. A. "Dynamic analysis of fully anchored circular cylindrical steel water storage tanks using finite element method" Msc thesis, University of Basrah, 2010.
11. Khtar A. K. "The effect of geometrical and mechanical properties of cylindrical liquid storage tanks on their dynamic response". Msc thesis, University of Basrah, 2012.

12. Malhotra P. K. and Eeri M. " Sloshing Loads in Liquid-Storage Tanks with Insufficient Freeboard" Earthquake Engineering Research Institute, Vol. 21, No. 4, pages 1185–1192, 2005.
13. Jaiswal O. R., Kulkarni S. and Pathak P. "A study on sloshing frequencies of fluid-tank system " The 14th World Conference on Earthquake Engineering October 12-17, 2007, Beijing, China.
14. Pal, P. "Sloshing of liquid in partially filled container- an experimental study" International Journal of Recent Trends in Engineering, Vol. 1, No. 6, 2009.
15. Chopra A.K. "Dynamics of structures: Theory and Applications to Earthquake Engineering", Electronic Publishing Services Inc., Prentice Hall, 1995.

Large amplitude dynamics of beam subjected to a compressive axial force resting on non-linear elastic foundation

Talib H. Elaikh

Mech. Eng. Depart. College of Engineering, Thi-Qar University

taleb_ehres@yahoo.com

Abstract

In this paper, the large amplitude of free vibration and buckling of Euler–Bernoulli beam rests on a non-linear elastic foundation subjected to an axial force are studied. Hamilton's principle is followed to derive governing equation of the beam response. Using an analytical method based on the Galerkin technique, the nonlinear governing equations of motion was simplified to a time-dependent Duffing equation with cubic nonlinearities and then solved using Laplace Iteration Method. Comparison between results of the present work and those available in literature review shows reasonable agreement of this method. Effects of vibration amplitude, elastic coefficients of foundation and axial force on the non-linear natural frequencies and buckling load of beams are presented. Results reveal that decreasing linear and shear parameters and increasing nonlinear parameters of foundation lead to increasing frequency ratio and buckling load ratio. Furthermore, increasing axial force decreases absolute values of both linear and nonlinear frequencies as well as natural frequency ratio.

Keywords:

Nonlinear Vibration; Buckling; Euler-Bernoulli beam; Non-linear elastic foundation; Galerkin method ; Laplace Iteration Method;

السعة الديناميكية الكبيرة لعارضة معرضة لقوة ضغط محورية مسندة على أساس مرن غير

خطي

الخلاصة

في هذا البحث تم دراسة السعة العالية للاهتزاز الحر والانبعاج لعارضة اويلر-برنولي مستقرة على اساس مرن غير خطي معرض الى قوة محورية. تم استخدام مبدا هاملتون في اشتقاق المعادلة الحاكمة لاستجابة العارضة. استخدم الأسلوب التحليلي استنادا إلى تقنية Galerkin ، تم تبسيط المعادلات الغير خطية الحاكمة للحركة الى معادلة دفنج المعتمدة على الزمن من الدرجة الثالثة والغير خطية وبعد ذلك تم حلها باستخدام طريقة

لابلاس للتكرار. مقارنة النتائج التي تم الحصول عليها في هذه الدراسة و تلك المتاحة في الأدبيات اظهرت توافق معقول لهذه الطريقة . تأثيرات كل من سعة الاهتزاز ، معامل مرونة الاساس والقوة المحورية على الترددات الطبيعية اللاخطية وحمل الانبعاج للعارضة تمت دراستها. النتائج بينت بأن خفض المعاملات الخطية و معاملات القص وزيادة المعاملات اللاخطية للأسس ادت إلى زيادة نسبة التردد و نسبة الانبعاج. بالإضافة الى ذلك، زيادة القوة المحورية قللت القيم المطلقة لكل من الترددات الخطية وغير الخطية وكذلك نسبة التردد الطبيعي.

كلمات مرشدة

الاهتزازالغير الخطي؛ الانبعاج؛ عارضة؛ اويلر-برنولي ؛ اساس لا خطي المرونة ؛ طريقة كارلكن؛ طريقة لابلاس التكرارية.

1-Introduction

Beam is one of the important mechanical elements and has numerous applications in different fields of engineering and industries such as civil, marine and aerospace structures or vehicles.

In most applications, they are subjected to non-linear vibrations which lead to material fatigue and structural damage due to increment of the oscillation amplitude [1]. Therefore, it is necessary and very important to study dynamic nonlinear behavior and natural responses of these structures at large amplitudes. Many investigations have been reported on the linear, non-linear vibration and buckling of Euler-Bernoulli beams with and without an elastic foundation. Lai et al. [2] utilized Adomian Decomposition Method to obtain the natural frequencies and mode shapes for the Euler- Bernoulli beam under various supporting conditions. Non-linear vibration behavior Euler-Bernoulli beams subjected to axial load using homotopy analysis method (HAM) is investigated by Pirbodaghi et al. [3]. Barari et al. [4] studied non-linear vibration behavior of geometrically non-linear Euler-Bernoulli beams using variational iteration method and parameter perturbation method. Non-linear vibration Euler-Bernoulli beams subjected to axial load using He's variational approach (VA) and Laplace iteration methods (LIM) is studied by Bagheri et al. [5]. Analysis of the nonlinear free vibration of simply-supported and clamped-clamped Euler-Bernoulli beams fixed at one end subjected to the axial force using Hamiltonian approach is presented by Bayat et al. [6]. Nonlinear vibration analysis of isotropic beams with simple end conditions has been investigated by Kargarnovin and Jafari [7]. They have used the HAM to obtain closed-form solutions for natural frequencies and beam deflection. Liu and Gurram [8] investigated the free vibration of Euler-Bernoulli beam

under various supporting conditions using a variational iteration method. Nonlinear analysis for simply supported beam resting on a two-parameter elastic foundation is presented by Hui-Shen [9]. The large amplitude free vibration of uniform beams on Pasternak foundation using the conservation of total energy principle is presented by Venkateswara [10]. The LIM method which was introduced by Rafieipour et al. [11] is a very powerful method in solving non-linear differential equations and its effectiveness is proved in studying non-linear vibration of composite plate. It was shown that this is one of the best analytical methods due to the rate of convergence and its accuracy.

The objectives of the present paper are to use the Laplace Iteration Method to obtain approximate analytical solutions for large amplitude dynamic of Euler–Bernoulli beam subjected to a compressive axial force resting on non -linear elastic foundation and to study the influence of different parameters on the frequency and post-buckling loads of the beam.

2. Theoretical formulation

A simply supported beam with uniform cross section made of a homogenous isotropic material with negligible damping is considered. The beam is supported on an elastic foundation with cubic nonlinearity and shearing layer as shown in Fig.1. The beam is modeled according to Euler Bernoulli beam theory. Planes of the cross sections remain planes after deformation, straight lines normal to the midplane of the beam remain normal, and straight lines in the transverse direction of the cross section do not change length, [4]

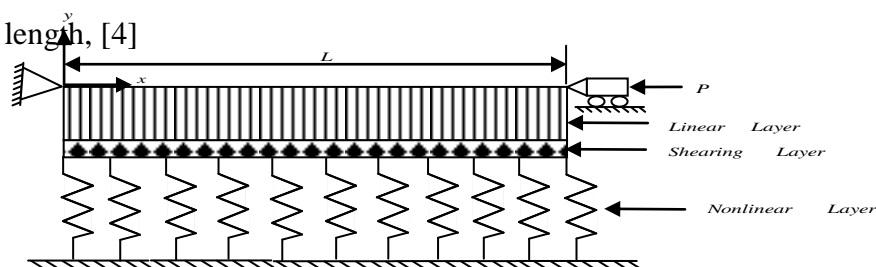


Fig. 1: A schematic of an Euler-Bernoulli beam subjected to an axial load resting on non -linear elastic foundation

Based on the Euler–Bernoulli beam theory, the nonlinear strain–displacement relations of the beam with the axially immovable ends are given by, [14]

$$\varepsilon_x = \frac{\partial u}{\partial x} + \frac{1}{2} \left(\frac{\partial w}{\partial x} \right)^2, \quad k_x = \frac{\partial^2 w}{\partial x^2} \quad \text{--- (1)}$$

where u is the longitudinal displacement, w is the lateral displacement and k_x is the curvature of the beam, respectively. In this study, the equations of motion are derived by using Hamilton's principle. This principle can be expressed as, [12]

$$\delta \int_0^t [K_e - (U_s - W_{ext})] dt = 0 \quad \text{--- (3)}$$

In equation (5), K_e is the kinetic energy, U_s is the elastic strain energy and W_{ext} is the work done by the external applied forces and these are given by, [10,12]

$$\begin{aligned} T_e &= \frac{1}{2} \int_0^L m \left\{ \frac{\partial w}{\partial t} \right\}^2 dx \\ U_s &= \frac{1}{2} \int_0^L \left(EA \left\{ \frac{\partial u}{\partial x} + \frac{1}{2} \left(\frac{\partial w}{\partial x} \right)^2 \right\} + EI \left\{ \frac{\partial^2 w}{\partial x^2} \right\}^2 \right) dx \\ W_{ext} &= \frac{1}{2} \int_0^L k_L w^2 dx + \frac{1}{2} \int_0^L k_{NL} w^4 dx - \frac{1}{2} \int_0^L k_s \left(\frac{\partial w}{\partial x} \right)^2 dx + \frac{1}{2} \int_0^L p \left(\frac{\partial w}{\partial x} \right)^2 dx \end{aligned} \quad \text{--- (4)}$$

Applying the Extended Hamilton's principle [12], the governing equation of transverse vibration of beam including axial stretching on a nonlinear elastic foundation can be obtained as:

$$\frac{\partial^2}{\partial x} \left\{ EI \frac{\partial^2 w}{\partial x^2} \right\} + p \frac{\partial^2 w}{\partial x^2} - \left\{ \frac{EA}{2L} \int_0^L \left(\frac{\partial w}{\partial x} \right)^2 dx \right\} \frac{\partial^2 w}{\partial x^2} + m \frac{\partial^2 w}{\partial t^2} + k_L w + k_{NL} w^3 - k_s \left(\frac{\partial^2 w}{\partial x^2} \right) = 0 \quad \text{--- (5)}$$

For convenience, the following non-dimensional variables are used:

$$X = x / L, \quad W = w / r, \quad t = \bar{t} (EI / mL^4)^{1/2}, \quad r = \sqrt{(I / A)}, \quad \text{--- (6)}$$

As a result equation (5) can be written as follows:

$$\frac{\partial^2 W}{\partial t^2} + \frac{\partial^4 W}{\partial X^4} + P \frac{\partial^2 W}{\partial X^2} - \frac{1}{2} \frac{\partial^2 W}{\partial X^2} \int_0^1 \left(\frac{\partial W}{\partial X} \right)^2 dX + K_L W + K_{NL} W^3 - K_s \left(\frac{\partial^2 W}{\partial X^2} \right) = 0 \quad \text{--- (7)}$$

In which:

$$P = pL^2 / EI, \quad K_L = kL^4 / EI, \quad K_{NL} = k_{NL} L^6 / EI, \quad K_s = k_s L^2 / EI \quad \text{--- (8)}$$

Assuming $w(X, t) = q(t)\phi(x)$ where $\phi(x)$ is the first normal mode of the beam [16] and using the Galerkin method, the governing equation of motion is obtained as follows:

$$\frac{d^2 q(t)}{dt^2} + (\alpha_1 + P\alpha_p + \alpha_{K_L} + \alpha_{K_s})q(t) + (\alpha_{K_{NL}} + \alpha_3)q^3(t) = 0 \quad \text{--- (10)}$$

where coefficients α_i are presented in Appendix A. The beam centroid is subjected to the following initial conditions, [3]

$$q(x,0) = W_{\max} \quad \frac{dq(x,0)}{dt} = 0 \quad \text{--- (11)}$$

From equation (10), the Post-buckling load–deflection relation of the beam can be obtained as:

$$P_{NL} = \frac{-(\alpha_1 + \alpha_{K_L} + \alpha_{K_S}) - (\alpha_{K_{NL}} + \alpha_3)q(t)^2}{\alpha_2} \quad \text{--- (12)}$$

It should be noted that neglecting the contribution of q in equation (16), the linear buckling load can be determined as, [17]

$$P_L = P_{cr} = \frac{-(\alpha_1 + \alpha_{K_L} + \alpha_{K_S})}{\alpha_2} \quad \text{--- (13)}$$

Equation (10) is strongly nonlinear and nobody can find an exact analytical closed form solution for $q(t)$ and ω_{NL} . Although numerical methods can be implemented to get over this problem but, they cannot offer any suitable way for parametric study. Therefore, it will be valuable if a powerful analytical approximate method exists that presents an accurate approximation of $q(t)$ and ω_{NL} while providing the ability to parametric study of the problem.

3- Description of the proposed method

Using the Laplace Transformation method, an analytical approximated technique is proposed to present an accurate solution for nonlinear differential equations. To clarify the basic ideas of proposed method consider the following second order differential equation [11],

$$\ddot{u}(t) + N\{u(t)\} = 0 \quad \text{--- (14)}$$

With artificial zero initial conditions and N is a nonlinear operator. Adding and subtracting the term $\omega^2 u(t)$, equation (14) can be written in the form

$$\ddot{u}(t) + \omega^2 u(t) = L\{u(t)\} = \omega^2 u(t) - N\{u(t)\} \quad \text{--- (15)}$$

where L is a linear operator. After taking Laplace transform of both sides of the equation (15) in the usual way and then implementing the Laplace inverse transform by using the Convolution theorem yields:

$$u(t) = \int_0^t (\omega^2 u(\tau) - N\{u(\tau)\}) \frac{1}{\omega} \sin(\omega(t-\tau)) d\tau \quad \text{--- (16)}$$

Now, the actual initial conditions must be imposed. Finally the following iteration formulation

can be used, [13]

$$u_{n+1} = u_0 + \frac{1}{\omega} \int_0^t (\omega^2 u_n(\tau) - N\{u_n(\tau)\}) \sin(\omega(t-\tau)) d\tau \quad \text{--- (17)}$$

Knowing the initial approximation u_0 , the next approximations, u_n , $n > 0$ can be determined

from previous iterations. Consequently, the exact solution may be obtained by using

$$u = \lim_{n \rightarrow \infty} u_n \quad \text{--- (18)}$$

The method proposed here can be applied in various non-linear problems. However, there is no

need for any linearization and any small parameter, also, the obtained approximate solutions converge quickly to the exact one.

4-Implementation of the proposed method

Rewriting equation (10) in the standard form of equation (15) results in the following equation:

$$\frac{d^2 \eta(t)}{dt^2} + \omega^2 \eta(t) = \omega^2 \eta(t) - N\{\eta(t)\} \quad \text{--- (19)}$$

where

$$N\{\eta(t)\} = \alpha \eta(t) + \beta \eta^3(t) \quad \text{and} \quad \alpha = \alpha_1 + P \alpha_p + \alpha_{K_L} + \alpha_{K_S}, \quad \beta = (\alpha_{K_{NL}} + \alpha_3) \quad \text{--- (20)}$$

Applying the proposed method, the following iterative formula is formed as:

$$\eta_{n+1} = \eta_0 + \frac{1}{\omega} \int_0^t (\omega^2 (\eta_n(\tau)) - N\{\eta_n(\tau)\}) \sin(\omega(t-\tau)) d\tau \quad \text{--- (21)}$$

Equation(19) will be homogeneous, if left side of this equation is considered to be zero. So, it's homogeneous Solution

$$\eta_0(t) = W_{\max} \cos(\omega t) \quad \text{--- (22)}$$

is considered as the zero approximation for using in iterative equation (21)

Expanding $f(\eta_0(\tau))$ we have:

$$f(\eta_o(\tau)) = \left(-\alpha W_{\max} + \omega^2 W_{\max} - \frac{3}{4} \beta W_{\max}^3 \right) \cos(\omega t) - \frac{1}{4} \beta W_{\max}^3 \cos(3\omega t) \quad \text{--- (23)}$$

Considering the relation:

$$\frac{1}{\omega} \int_0^t (\cos(m\omega\tau)) \sin(\omega(t-\tau)) d\tau = \begin{cases} \frac{\cos(\omega t) - \cos(m\omega t)}{\omega^2(m^2-1)} & m \neq 1 \\ \frac{t \sin(\omega t)}{2\omega} & m = 1 \end{cases} \quad (24)$$

The coefficient of the term $\cos(\omega t)$ in $f(\eta_o(\tau))$ should be vanished in order to avoid secular terms in subsequent iterations.

As a result, the nonlinear natural frequency of the motion can be expressed as:

$$\omega_{LIM} = \sqrt{\alpha + \frac{3}{4} \beta W_{\max}^2} \quad \text{--- (25)}$$

Then, the nonlinear to linear frequency ration can be determined as:

$$\frac{\omega_{NL}}{\omega_L} = \frac{\sqrt{\alpha + \frac{3}{4} \beta W_{ma}^2}}{\sqrt{\alpha}} \quad \text{--- (26)}$$

and, the zero-order approximate solution can be easily determined as:

$$\eta(t) = W_{\max} \cos\left(\sqrt{\alpha + \frac{3}{4} \beta W_{\max}^2} t\right) \quad \text{--- (27)}$$

5-Results and discussion

In order to demonstrate the accuracy and effectiveness of the LIM, The procedure explained in previous section is applied to simply supported and clamped beams. Table 1 shows the comparison of non-linear to linear frequency ratio (ω_{NL} / ω_L) with those reported in the literature. It can be observed that there is a reasonable agreement between the results obtained from the LIM and those reported by Ref's [14 and 15]. By increasing the amplitude of vibration the difference between the non-linear frequency and linear frequency increases. In general, large vibration amplitude will yield a higher frequency

Table 1 Comparison of nonlinear to linear frequency ratio (ω_{NL} / ω_L)

Boundary condition	W_{max}	Ref. [14]	Ref. [15]	Present Study
Simply supported	1	1.0897	1.0891	1.0897
	2	1.3229	1.3228	1.3228
	3	1.6394	1.6256	1.6293
Clamped-clamped	1	1.0552	1.0572	1.0551
	2	1.2056	1.2125	1.2056
	3	1.3904	1.4344	1.4214

The exact nonlinear frequency (ω_{ex}) of Duffing equation (10) can be determined as [18]:

$$\omega_{ex} = 2\pi \left(4 \int_0^{\pi/2} \frac{d\tau}{\sqrt{(\alpha_1 + P\alpha_2 + \alpha_{K_L} + \alpha_{K_S}) + \frac{1}{2}(\alpha_{K_{NL}} + \alpha_3)W_{max}^2(1 + \sin^2(\tau))}} \right)^{-1} \quad (28)$$

The another verification attempt, frequency ration obtained by equation (25) for versus dimensionless amplitude is compared with the results obtained from exact frequency ratio using equation (28), as shown in Table (2). A reasonably good agreement with exact solution for nonlinear analysis of beam can be observed.

Table 2: Comparison of nonlinear to linear frequency ratio (ω_{NL} / ω_L)

a	Present Study	Exact	Relative Error
0	1.0000	1.0000	0.000
1	1.0233	1.0213	0.002
2	1.0882	1.0863	0.019
3	1.1891	1.1871	0.002
4	1.3175	1.3167	0.008
5	1.4662	1.4658	0.004

The effect of the elastic foundation coefficients and axial force on the nonlinear natural frequency and post-buckling behavior of simply supported beams is studied. The figures (2-5) demonstrate effects of foundation parameters, linear (K_L), shear (K_S) and nonlinear (K_{NL}) for simply supported beam. In all figures, the dimensionless frequency ratio (ω_{NL} / ω_L) and dimensionless nonlinear to linear buckling load ratio (P_{NL} / P_L) versus dimensionless amplitude are presented. It is worth mentioning that (P_{NL}) is determined by maximizing equation (12) in one period

of vibration. It can be concluded from figures (2, 3) together with Table (3) that an increase in the value of linear elastic foundation stiffness and shearing layer stiffness results in decreasing hardening characteristic of the beam i.e. decrease in the rate of increase in the nonlinear frequency and post-buckling strength with amplitude. Whereas it is shown in figure (4) that an increase in the value of nonlinear elastic foundation stiffness has inverse results on the nonlinear frequency and post-buckling strength i.e. the rate of increase in these figures enhances with an increase in nonlinear foundation stiffness. The results might be explained by writing frequency ratio based on equation (26) as:

$$\frac{\omega_{NL}}{\omega_L} = \sqrt{1 + \frac{3}{4} \frac{\beta}{\alpha} W_{max}^2} \quad \text{--- (28)}$$

Considering the fact that α is a function on both linear and shear stiffness of the foundation while β remain constant. This yields to decreasing frequency ration by increasing κ_L and κ_s . On the other hand, however the effect of nonlinear stiffness coefficient of the foundation appears only in β which results in increasing the frequency ratio.

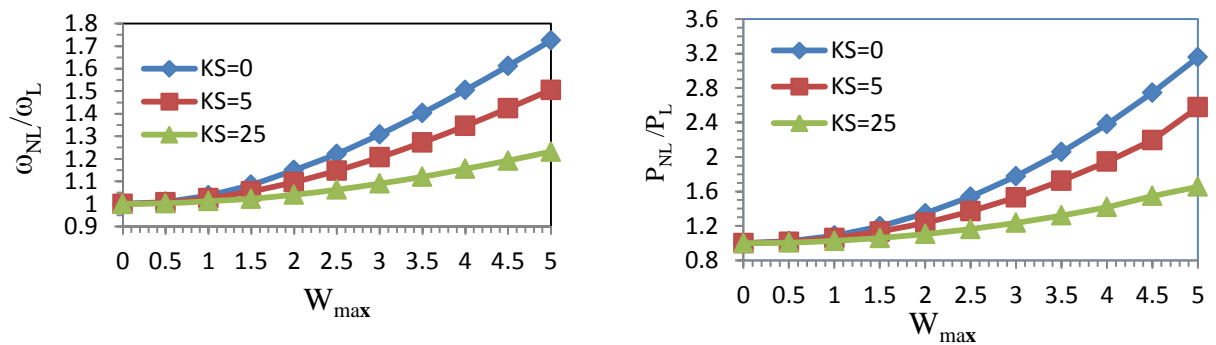


Fig.2: Effects of the shear foundation stiffness on the frequency and post-buckling load-deflection.

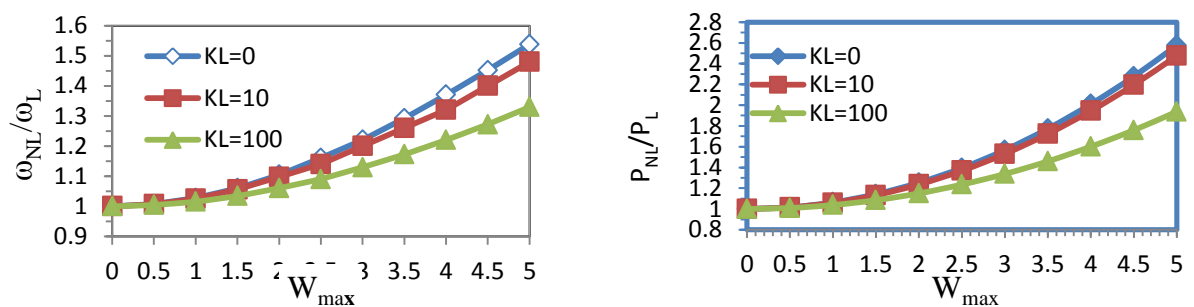


Fig.3: Effects of the linear foundation stiffness on the frequency and post-buckling load-deflection.

Table 3: Comparison of nonlinear frequency (ω_{NL}) and nonlinear to linear frequency ratio (ω_{NL} / ω_L) with change of different factors for beam, $a=2$.

Nonlinear natural frequency						Nonlinear to linear frequency			
P	K_L	K_{NL}				K_{NL}			
		0		100		0		100	
		K_S		K_S		K_S		K_S	
		0	25	0	25	0	25	0	25
0	0	10.227	18.749	17.564	23.564	1.0373	1.0106	1.779	1.2702
	50	12.447	20.038	18.935	24.602	1.0277	1.009	1.559	1.239
5	0	5.609	17.383	16.099	22.493	1.0742	1.0124	2.322	1.31
	50	10.269	18.767	17.583	23.577	1.0368	1.0106	1.776	1.269

The effect of initial and pre-buckled non-dimensional axial force on the nonlinear natural frequency is shown in figure (5). It can be concluded that the values of nonlinear frequency decrease with increase in the axial force, whereas nonlinear to linear frequency ratio enhances with an increase in the axial force value.

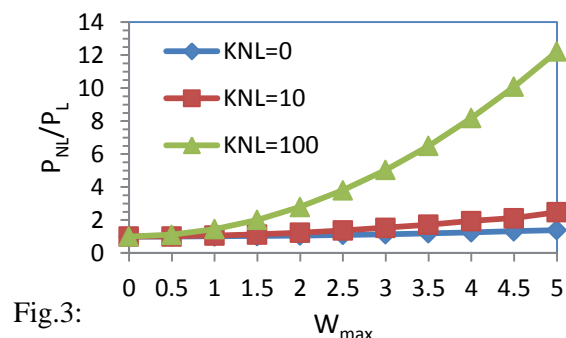
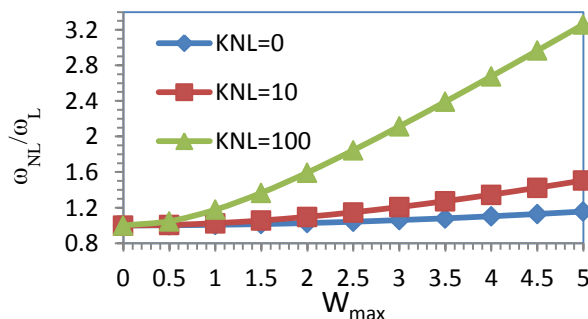


Fig.3:

Effects of the non- linear foundation stiffness on the frequency and post-buckling load-deflection.

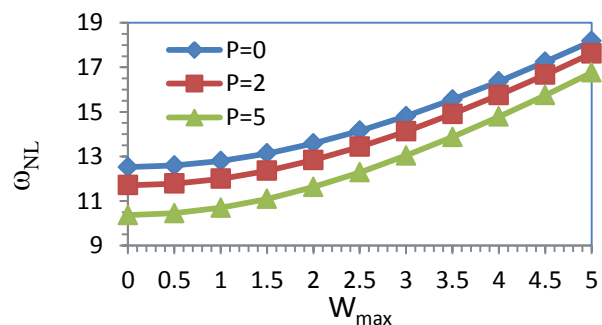
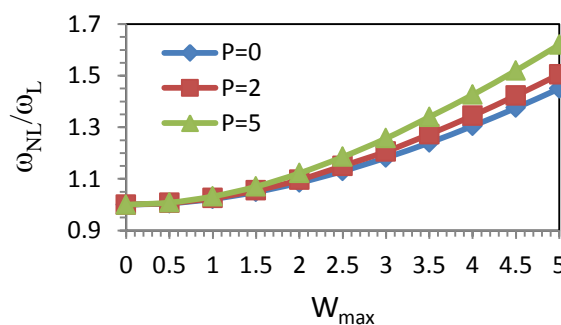


Fig.5: Effects of the axial load on the frequency ratio of the beam

6- Conclusions

Laplace Iteration Method is used to obtain the analytical expressions for the nonlinear free vibration of an Euler-Bernoulli beam on a nonlinear elastic foundation subjected to axial compressive force. The influence of foundation stiffness parameters and initial pre-buckled axial load on the nonlinear natural frequency and post-buckling load-deflection has been investigated. Based on a detailed study, the following observations are made:

- 1- The influence of linear and shear layer stiffness parameters is to decrease the nonlinear behavior of the beam, whereas the nonlinear layer stiffness of the foundation increases the strength of the nonlinearity.
- 2- The rate of increase in nonlinear to linear natural frequency and post-buckling to critical load ratios is very low at small amplitudes. However, as the amplitude increases, the effect of nonlinearity on these parameters becomes significant.
- 4-The nonlinear to linear frequency ratio enhances with an increase in the value of the axial force, whereas the values of nonlinear frequency decrease.
- 5-Laplace Iteration Method provides the ability for parametric study of the considered problem. Results revealed that the presented method offers accurate solution with low computational effort.
- 6- Comparison between the results of the present study and other methods available in the literature shows the accuracy of the method.

Appendix A:

$$\alpha_1 = \frac{\int_0^l \phi'''' \phi dx}{\int_0^l \phi^2 dx}, \quad \alpha_2 = \frac{\int_0^l \phi'' \phi dx}{\int_0^l \phi^2 dx}, \quad \alpha_{K_s} = -K_s \frac{\int_0^l \phi'' \phi dx}{\int_0^l \phi^2 dx}$$

$$\alpha_{K_{NL}} = K_{NL} \frac{\int_0^l \phi^4 \phi dx}{\int_0^l \phi^2 dx}, \quad \alpha_3 = -0.5 \frac{\int_0^l \phi'' \phi dx \int_0^l \phi'^2 dx}{\int_0^l \phi^2 dx}, \quad \alpha_{K_L} = K_L$$

References

- [1] M.T. Ahmadian, M. Mojahedi, H. Moeenfar, (2009). “ Free Vibration Analysis of a Nonlinear Beam Using Homotopy and Modified Lindstedt-Poincare Methods” J. of Solid Mechanics Vol. 1, pp.29-36.
- [2] Lai, H.Y., Hsu, J.C., Chen, C.K., (2008). “An innovative eigenvalue problem solver for free vibration of Euler- Bernoulli beam by using the Adomian Decomposition Method”, Computers and Mathematics with Applications, 56, 3204-3220.
- [3] T. Pirbodaghi, M. T. Ahmadian, M. Fesanghary , (2009) “ On the homotopy analysis method for non-linear vibration of beams” Mechanics Research Communication, 36, 143-148.
- [4] A. Barari, H.D.Kaliji, M.Ghadimi and G. Domairry , (2011) “ Non-linear vibration of Euler-Bernoulli beams” Latin American Journal of Solid and Structure” 8, 139-148.
- [5] S. Bagheri, A. Nikkar , H. Ghaffarzadeh , (2014) “Study of nonlinear vibration of Euler-Bernoulli beams by using analytical approximate techniques” Latin American Journal of Solids and Structures 11,157 – 168.
- [6] M. Bayat, I. Pakar and M. Bayat, (2013) “ On the large amplitude free vibration of axially loaded Euler-Bernoulli beams” Steel and Composite Structure, 14(1) , 73-83.
- [7] Kargarnovin, M.H., Jafari-Talookolaei, R.A. (2010) “Application of the homotopy method for the analytic approach of the nonlinear free vibration analysis of the simple end beams using four engineering theories” Acta Mechanics. **212**, 199–213.
- [8] Liu, Y., Gurram, C. S., (2009)” The use of He’s variational iteration method for obtaining the free vibration of an Euler-Beam beam” Math. and Computer Modelling 50:1545-1552.
- [9] Hui-Shen Shen, (2011)” A novel technique nonlinear analysis of beams on two-parameter elastic foundation” Int. J. of Structural Stability and Dynamics, 11(6), 999-1014.
- [10] G. Venkateswara Rao, (2003) ” The large amplitude free vibration of uniform beams on Pasternak foundation” Journal of Sound and Vibration, 263, 954-960.
- [11] Rafieipour, H. , Lotfavar, A. , Masroori, A., Mahmoodi, E.,(2013) “Application of Laplace iteration method to study of nonlinear vibration of laminated

- composite plates Latin American Journal of Solids and Structures , 10(4), 781-795.
- [12] S. S. Rao., (2007) “ Vibration of Continuous Systems” John Wiley & Sons, Inc., Hoboken, New Jersey.
- [13] E. Hesameddini and H. Latifizadeh, (2009) “Reconstruction of variational iteration algorithms using the Laplace transform “Int. J. Nonlinear Sci. Numerical. Simulation, 10(10), 1365-1370.
- [14] R.K. Gupta, Gunda Jagadish Babu ,G. Ranga Janardhan ,G. Venkateswara Rao,(2009) “Relatively simple finite element formulation for the large amplitude free vibrations of uniform beams” Finite Elements in Analysis and Design, Vol. 45, Issue 10, pp. 624–631.
- [15] Emam SA., Nayfeh AH. (2009), “Postbuckling and free vibration of composite beams” J. of Computer and Structure Vol. 88, pp. 634-642.
- [16] Azimi M. and Kariman S. (2013), “Periodic Solution for Vibration of Euler-Bernoulli Beams Subjected to Axial Load Using DTM and HA” J Appl Mech Eng 2:2 <http://dx.doi.org/10.4172/2168-9873.1000125>
- [17] I. Pakar and M. Bayat (2013), “An Analytic Study of Nonlinear Vibrations of Buckled Euler-Bernoulli Beams” J. of Acta Physica Polonica A, Vol. 123 , pp. 48-52.
- [18] Younesian, D., Askari, H., Saadatnia, Z., KalamiYazdi, M., (2010) “Frequency analysis of strongly nonlinear generalized Duffing oscillators using He's frequency-amplitude formulation and He's energy balance method” Computers and Mathematics with Applications, 59(9), pp. 3222-3228.

Nomenclature

A	Cross section of beam (m^2)	<u>Greek symbols</u>
E	Young's modulus (N/m^2)	ω_L Linear fundamental frequency (rad/s)
I	Second moment of area (m^4)	ω_{NL} Non-linear frequency (rad/s)
\bar{k}_L	Linear foundation stiffness (N/m)	$\phi(x)$ Trial function

\bar{k}_{NL}	Nonlinear foundation stiffness (N/m ³)
\bar{k}_s	Shearing layer stiffness (Nm)
k_x	The curvature of the beam
ε_x	The nonlinear axial strain
L	Length of beam (m)
m	Mass per unit length (kg/m)
p	Axial load (N)
r	Radius of gyration of the cross section (m)
\bar{t}	Time (s)
u	Longitudinal displacement (m)
w	Transverse displacement (m)
w(t)	Time-dependent deflection parameter
W_{max}	Dimensionless maximum amplitude of oscillation (m)